Contrib. Astron. Obs. Skalnaté Pleso **48**, 396 – 404, (2018)

AXRO introduction and historical background

R. Hudec[1,2]

[1] *Czech Technical University in Prague, Faculty of Electrical Engineering*
Technicka 2, Prague 166 27, Czech Republic
(E-mail: hudecren@fel.cvut.cz)
[2] *Engelhardt Astronomical Observatory, Kazan Federal University,*
Kremlyovskaya street 18, 420008 Kazan, Russian Federation

Received: December 21, 2017; Accepted: January 25, 2018

Abstract. With the AXRO conference held in December 2017 in Prague, we celebrated the 10th anniversary of these international workshops on astronomical X–ray optics. In this contribution a short overview on the AXRO history and its background is given, including a short history of grazing incidence X–ray optics in the Czech republic.

Key words: X–ray optics – X-ray telescopes – X–ray astrophysics

1. Introduction

With the first X–ray lens produced around 1969/1970, astronomical X–ray optics has a long tradition in the Czech Republic. With this years AXRO (International Workshop on Astronomical X–ray Optics) conference in Prague (December 2017), we celebrated the 10th anniversary of these workshops. The goal of this contribution is to present and to briefly discuss the history of development of astronomical X–ray optics in the Czech Republic, and in addition to that, to present background and history of the international astronomical X-ray optics conferences AXRO. The Czech efforts in the field of astronomical X–ray optics in the past focused mainly on development and tests of numerous technologies, including novel techniques, novel materials, and novel designs.

2. History of Grazing Incidence X-Ray Optics in the Czech Republic

The AXRO history is related to the history of X–ray astronomy in general and to the history of X-ray optics developments in the Czech Republic (and formerly in Czechoslovakia) in particular.

The first Czech X-ray mirror was built already in the years 1969/1970, for a solar telescope within the Eastern Europe/Soviet INTERKOSMOS program (Hudec & Valníček, 1984). The early stages of the X-ray optics developments in the Czech Republic are closely related to the INTERKOSMOS Space Program (the Soviet and Eastern European equivalent to ESA, operated until 1989), see Fig.1. All of the X-ray imaging telescopes on board of soviet spacecrafts until 1990 were equipped with the Czech X-ray optics (exception: X-ray normal incidence mirrors in the special channel of the TEREK telescope). Later on, laboratory applications have been started in addition. A very short summary is given below.

- The total number of X-ray mirrors produced is more than 80.
- The total number of mirrors flown in space is 9.
- The total number of spacecrafts equipped with Czech X-ray optics is 5.
- The number of space experiments with Czech X-ray optics onboard is 9.

Figure 1. The early stages of the Czech X–ray optics developments. Left: Electroformed mandrel for musical records. Right: Replicated galvanoplastic Wolter 1 mirror with an aperture of 115 mm developed for the AUOS–S satellite. The mirror material was quite heavy, made from nickel with a wall thickness of around 1 cm

The first Czech X-ray mirror in space was the Wolter 1 mirror (50 mm aperture) on the Vertikal 8 rocket (Hudec et al., 1984), as illustrated by Fig. 2. In this historical experiment, soft X-ray images of the sun were obtained in an experimental trial of the f/45 RTF imaging telescope (using a 6 micron-thick Al filter for 0.8 -2.2 nm wavelengths and a 20 micron thick Be filter for 0.6 - 2.0 nm) during the Vertikal-8 high-altitude rocket flight of September 26, 1979, with the data being analyzed using digital processing techniques. The two images are found to be underexposed, so that only one active region, corresponding in position to McMath 16298, could be defined. The method of filter ratios was used to calculate the temperature and emission measure of the region as $(1.3 \pm 0.5) \cdot 10^6$ K and $4 \cdot 10^{29}$ cm^{-3}, respectively. This experiment was repeated in 1980 with Vertikal 11 rocket flight. There were always two X–ray telescopes on board (both with our 50 mm aperture X–ray Wolter mirror), one in collaboration with CBK Wroclaw, Poland, and the second one in collaboration with FIAN Lebedew Institute in the Soviet Union.

The most recent Czech X–ray mirror in space is then the 1D LE module on the VZLUSAT–1 cube satellite (Pína et al., 2016; Urban et al., 2017a). Further experiments are planned in the near future, for example the sounding Water Recovery X-ray Rocket (Dániel et al., 2017; Stehlikova et al., 2017a) with iridium coated X-ray mirrors (Stehlikova et al., 2017b).

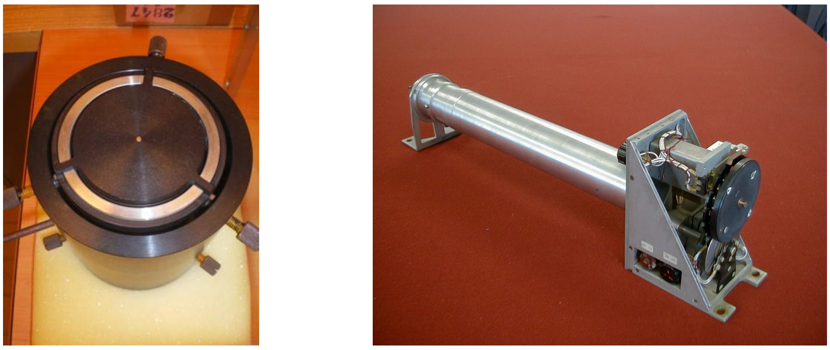

Figure 2. First space experiment with Czech grazing incidence X–ray optics was the X–ray telescope with photographic recording developed in collaboration with Poland and Soviet Union for the Vertikal 8 rocket flight in 1979. Left: The X–ray mirror. Right: The telescope.

And a very concise history of Czech astronomical X–ray mirrors follows here.

- 1969 first considerations started
- 1970 first solar X-ray mirror produced (Wolter 1, aperture 50 mm)
- 1971 Wolter 1 (aperture 80 mm)
- 1976 Wolter 1 (aperture 115 mm)
- 1979 first mirrors flown in space (two Wolter 50 mm in 2 experiments, Vertikal 9 rocket)
- 1980 Vertikal 11 rocket (two Wolter 50 mm in 2 experiments)
- 1981 first large Wolter mirror (aperture 240 mm)
- 1981 Salyut 7 orbital station (RT–4M X–ray telescope, Wolter 240 mm nested)
- 1985 applications for plasma physics, EH 17 mm, PP 20 mm
- 1987 first high quality X-ray foils for foil mirror X-ray telescope (SODART)

- 1988 Fobos 1 Mars probe, TEREK X-Ray Telescope, 80 mm Wolter 1
- 1989 KORONAS I X-ray mirror, Wolter 80 mm
- 1990 first micromirror (aperture less than 1 mm)
- 1993 collaboration with SAO, USA on a WF X-ray optics started
- 1996 first Lobster Eye (LE) test module, produced in Schmidt geometry
- 1997 double-sided X-ray reflecting flats
- 1997 Lobster Eye Angel geometry project started
- 1999 first Lobster Eye test module produced (Angel geometry)
- 2001 thin segmented X-ray mirrors
- 2004 thermal glass forming of samples of laboratory X-ray optics started
- 2005 replication of multilayers for X-ray optics
- 2006 X-ray optics based on Si wafers, Si wafers shaping started
- 2009 K-B (Kirkpatrick–Baez) Optics started
- 2014 1D LE optics
- 2015–2017 various LE and KB modules, AHEAD KB module, VZLUSAT–1 1D LE, REX LE.

The from gramophone industry adopted replication technology (Hudec et al., 1981) (Fig. 1), used for most of the Wolter mirrors developed between 1970 and 1990, was modified and upgraded several times with emphasis of internal stress reduction so that at later stages several copies from one polished mandrel were possible to be produced without mandrel degradation (Hudec & Valníček, 1984; Hudec et al., 1988), as documented by Fig. 3 and Fig. 4.

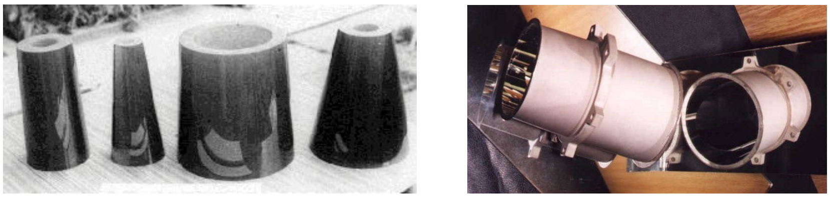

Figure 3. Galvanoplastic X–ray astronomical mirrors. Left: The four glass ceramics mandrels used for the Salyut 7 orbital station RT–4M X–ray telecope (with double nested Wolter 1 mirror with aperture of 240 mm, outer shell with Ni surface, inner shell with Au reflecting layer deposited by electroforming). Right: The two identical Wolter mirrors with 80 mm aperture for he KORONAS satellite.

Figure 4. The X–ray optics laboratory at the Ondrejov Observatory of the Astronomical Institute of the Czech Academy of Sciences, demonstrating the various technology tests.

It should be noted that the development before 1987 was done completely independent, without any contact to other groups abroad and without access to relevant literature and/or meetings and workshops. The development of galvanoplastic replication was also completely independent on efforts abroad.

The work was focused mainly on various technology developments and tests with verification on small mirrors, see Fig. 5.

The Czech X–ray optics consortium included many Czech Institutes and subjects over these past years, e.g. ASU AV CR, VUGT Lodenice, SVUM Prague, CTU in Prague, Institute of Chemical Technology in Prague, Optical workshop in Turnov, Reflex s.r.o., Rigaku RITE Prague, ON Semiconductor, and others.

There were also essential efforts devoted to the development of novel technologies for satellite projects which were either cancelled or interrupted. The two wasted years of development on the technology of high quality Ni foils for the Danish SODART telescope (Schnopper, 1990), 1986-1988, can serve as an example. The SOviet-DAnish Roentgen Telescope (SODART) was planned for on board the Spectrum Roentgen Gamma (SRG) satellite equipped with three different instruments devoted to X–ray spectroscopy. Each of the two thin foil telescopes had an 8 m focal length, a 60 cm diameter, a 1 deg field-of-view (FOV), a half-power width better than 2 arcmin and ca. 1 700 and 1 200 cm^2 collecting area at 2 and 8 keV, respectively.

Figure 5. Visit of the US Astronaut with Czech family origin John Blaha in the X–ray optics laboratory at the Ondrejov Observatory in 1998. From the left to the right: Rene Hudec, Astronaut John Blaha and his wife.

For this project, we have developed and tested galvanoplastic replication of glass flat mandrels, sizes up to 300 × 400 mm, and were able to demonstrate that the thickness homogeneity of replicated flat nickel foils during the project improved from 8 % to 2 %.

The galvanoplastic replication (or electroforming technology according to the term used by other teams) technology was originally adopted from gramophone industry namely under collaboration with large gramophone company located in Lodenice near Prague.

3. X–ray optics on VZLUSAT–1

The VZLUSAT–1 cubesatellite is the most recent satellite with Czech X–ray optics onboard. It represents an example of 2U cubesatellites with advanced astrophysical payload onboard (Dániel et al., 2016; Urban et al., 2017a). One of the payloads is represented by an one dimensional (Pína et al., 2016) miniature X–ray telescope (Pina et al., 2015) with a Timepix detector (Llopart et al., 2007; Urban et al., 2017b) in its focal plane (Baca et al., 2016). The main mission goal is the technological verification of the system, but scientific outcome is also expected for some bright celestial X–ray sources (Blazek et al., 2017; Daniel et al., 2016). This satellite represents the 5th satellite with Czech X–ray optics onboard.

4. History of AXRO workshops

The history of AXRO workshops is dated back to May 2007, when the Czech-US Seminar on Astronomical X-Ray Optics was organized in Prague, with participation of six leading US specialists in the field of astronomical X-ray optics. This seminar was attended by many Czech scientists and it was very productive,

Figure 6. The participants of the first US–Czech seminar on astronomical X–ray optics, Prague, May 2007, with a remarkable train trip to ON Semiconductor company in Roznov pod Radhostem, where the participants were able to see the production of high–quality silicon wafers recently used in various X–ray optics applications.

Figure 7. Participants of the 1st AXRO workshop held in Prague, December 2008.

as documented by Fig. 6. At the workshop, we have decided to repeat it with opening it to the international astronomical X–ray optics community. The first AXRO workshop was then indeed organized in Prague, at the historical Vila Lanna, in December 2009, see figure 7, and since then the astronomical X–ray optics scientists meet there every year in the second week in December.

5. Conclusion

The development of astronomical X–ray optics has a long tradition in the Czech republic with emphasis on development and tests of innovative approaches and technologies. Since 2007 we also organize a very successful and productive series of international workshops with ample time for discussions among participants.

The Czech X–ray optics consortium included many Czech Institutes and subjects over these past years, e.g. ASU AV CR, VUGT Lodenice, SVUM Prague, CTU in Prague, Institute of Chemical Technology in Prague, Optical workshop in Turnov, Reflex sro, Rigaku RITE Prague, ON Semiconductor, and others.

Acknowledgements. We acknowledge GA CR grant 13-33324S and AHEAD EU Horizon 2020 project (Integrated Activities in the High Energy Astrophysics Domain), grant agreement n. 654215.

References

Baca, T., Platkevic, M., Jakubek, J., et al., Miniaturized X-ray telescope for VZLUSAT-1 nanosatellite with Timepix detector. 2016, *Journal of Instrumentation*, **11**, C10007, DOI: 10.1088/1748-0221/11/10/C10007

Blazek, M., Pata, P., Inneman, A., & Skala, P., Astronomical Tasks for Tests of X-Ray Optics in VZLUSAT-1 Nanosatellite. 2017, *Advances in Astronomy*, **2017**, 316289, DOI: 10.1155/2017/3162892

Dániel, V., Inneman, A., Pína, L., et al., X-ray Lobster Eye all-sky monitor for rocket experiment. 2017, in Society of Photo-Optical Instrumentation Engineers (SPIE) Conference Series, Vol. **10235**, *Society of Photo-Optical Instrumentation Engineers (SPIE) Conference Series*, 1023503

Dániel, V., Pína, L., Inneman, A., et al., Terrestrial gamma-ray flashes monitor demonstrator on CubeSat. 2016, in Proceedings of the SPIE, Vol. **9978**, *CubeSats and NanoSats for Remote Sensing*, 99780D

Daniel, V., Urban, M., Nentvich, O., & Stehlikova, V., VZLUSAT-1: verification of new materials and technologies for space. 2016, in Proc. SPIE, Vol. **9978**, *CubeSats and NanoSats for Remote Sensing*, 99780N

Hudec, R., Valnicek, B., Aschenbach, B., Brauninger, H., & Burkert, W., Grazing Incidence Replica Optics For Astronomical And Laboratory Applications. 1988, in Proc. SPIE, Vol. **830**, *Grazing incidence optics for astronomical and laboratory applications*, 193–197

Hudec, R., Valnicek, B., Hudcova, V., Sylwester, J., & Kordylewski, Z., X-ray pictures of the sun taken from Vertical 8. 1984, *Bulletin of the Astronomical Institutes of Czechoslovakia*, **35**, 153

Hudec, R., Valnicek, B., Prazak, V., & Solc, I., Properties of galvanoplastic grazing incidence mirrors for astronomical applications. 1981, *Bulletin of the Astronomical Institutes of Czechoslovakia*, **32**, 188

Hudec, R. & Valníček, B., Development of x-ray mirrors for high-energy astrophysics in czechoslovakia. 1984, *Advances in Space Research*, **3**, 545, DOI: 10.1016/0273-1177(84)90143-1

Llopart, X., Ballabriga, R., Campbell, M., Tlustos, L., & Wong, W., Timepix, a 65k programmable pixel readout chip for arrival time, energy and/or photon counting measurements. 2007, *Nuclear Instruments and Methods in Physics Research A*, **581**, 485, DOI: 10.1016/j.nima.2007.08.079

Pina, L., Hudec, R., Inneman, A., et al., X-ray monitoring for astrophysical applications on Cubesat. 2015, in Proceedings of the SPIE, Vol. **9510**, *EUV and X-ray Optics: Synergy between Laboratory and Space IV*, 951005

Pína, L., Hudec, R., Inneman, A. J., et al., Development and tests of x-ray multifoil optical system for 1D imaging (Conference Presentation). 2016, in Proceedings of the SPIE, Vol. **9964**, *Advances in Laboratory-based X-Ray Sources, Optics, and Applications V*, 99640B

Schnopper, H. W., SODART Telescope on Spectrum-Roentgen-Gamma and its instrumentation. 1990, in Astrophysics and Space Science Library, Vol. **166**, *IAU Colloq. 123: Observatories in Earth Orbit and Beyond*, ed. Y. Kondo, 119–128

Stehlikova, V., Urban, M., Nentvich, O., et al., Hard X-ray Vela supernova observation on rocket experiment WRX-R. 2017a, *Contributions of the Astronomical Observatory Skalnate Pleso*, **47**, 165

Stehlikova, V., Urban, M., Nentvich, O., et al., Study of lobster eye optics with iridium coated x-ray mirrors for a rocket experiment. 2017b, in Society of Photo-Optical Instrumentation Engineers (SPIE) Conference Series, Vol. **10235**, *Society of Photo-Optical Instrumentation Engineers (SPIE) Conference Series*, 1023505

Urban, M., Nentvich, O., Stehlikova, V., et al., VZLUSAT-1: Nanosatellite with miniature lobster eye X-ray telescope and qualification of the radiation shielding composite for space application. 2017a, *Acta Astronautica*, **140**, 96, DOI: 10.1016/j.actaastro.2017.08.004

Urban, M., Nentvich, O., Stehlikova, V., & Sieger, L., Uncooled spectrometer for x-ray astrophysics. 2017b, in Society of Photo-Optical Instrumentation Engineers (SPIE) Conference Series, Vol. **10235**, *Society of Photo-Optical Instrumentation Engineers (SPIE) Conference Series*, 102350O

Contrib. Astron. Obs. Skalnaté Pleso **48**, 405 – 415, (2018)

Effects of manufacturing inaccuracies on spatial resolution of lobster eye optics

V. Tichý[1], M. Barbera[2,3], G. I. Butcher[1], U. Lo Cicero[3,2], A. Collura[3], R. Hudec[4,5], A. Inneman[4], S. Varisco[3] and R. Willingale[1]

[1] *University of Leicester, Department of Physics and Astronomy,*
University road, LE1 7RH Leicester, United Kingdom

[2] *Università degli Studi di Palermo, Dipartimento di Fisica e Chimica,*
Via Archirafi 36, 90123 Palermo, Italy

[3] *Istituto Nazionale di Astrofisica, Osservatorio Astronomico di Palermo G.S. Vaiana,*
Piazza del Parlamento 1, 90134 Palermo, Italy

[4] *Czech Technical University in Prague, Faculty of Electrical Engineering,*
Technická 2, 16627 Praha 6, Czech Republic

[5] *Engelhardt Astronomical observatory, Kazan Federal University,*
Kremlyovskaya street 18, 420008 Kazan, Russian Federation

Received: December 23, 2017; Accepted: March 3, 2018

Abstract. The performance of Schmidt lobster eye systems are affected by manufacturing inaccuracies in the assembly of individual mirrors or in their non ideal flatness. Such inaccuracies may significantly affect the optics performance and in particular the angular resolution. For this reason we have investigated, via ray-tracing simulations, the effects of such manufacturing inaccuracies. We report the preliminary results of this analysis and compare them with X-ray measurements performed on a test Schmidt lobster eye specimen using the 35 m long X-ray beam-line of the XACT facility of INAF-OAPA in Palermo, Italy.

Key words: lobster eye – multi-foil optics – reflective optics – grazing incidence optics – x-ray optics – technology aspects

1. Introduction

Lobster eye (LE) optics (Schmidt, 1975; Angel, 1979) are a very promising technology for space X-ray sky monitors since the field of view can be orders of magnitude larger than other geometries of grazing incidence optics. LE optics are part of the payload of the VZLUSAT-1 mission (Baca et al., 2016; Pina et al., 2015) and they are considered as possible candidate in several other missions (Petre et al., 2015; Gorenstein, 2011; Fraser et al., 2002; Tichý et al., 2015). Apart from space astrophysics applications LE are also used in laboratory applications such as neutron imaging (Šaroun & Kulda, 2006).

This paper in particular deals with Schmidt lobster eye (SLE) (Schmidt, 1975). A one-dimensional SLE is composed of one stack of flat rectangular mirrors (Fig. 1). These mirrors form a uniform pattern around a virtual cylinder. Two such stacks can be arranged to form a two-dimensional SLE.

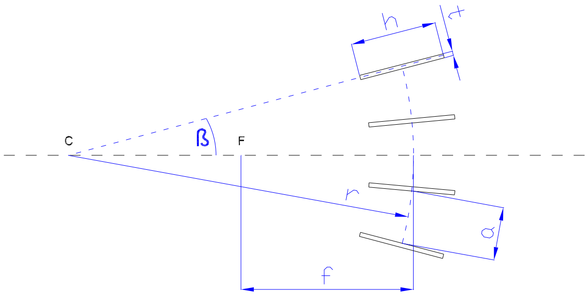

Figure 1. Lobster eye geometrical parameters.

A supporting structure is necessary to hold the mirrors in the SLE stack. Inaccuracies in the fabrication of the supporting structure and lack of flatness in actual mirrors introduce deviations from the ideal case (Tichý et al., 2011, 2009a,b). In this paper we investigate both aspects and how they affect the spatial resolution of SLE.

2. Experimental specimen LTW-51

To compare theory with experimental results, prototype lobster eye LTW-51 has been assembled, see Fig. 2. The prototype is one-dimensional, its focal length marked as f in Fig. 1 equals 51 cm. It is composed of 30 glass substrate mirrors of dimensions 37×37 cm, glass thickness t equals 0.28 mm. The pitch between centres of surfaces a is 0.995 mm. Mirrors are coated on both sides, so that the optic can operate in wide field mode. The coating consists of a bottom layer of gold and a 5 nm thin top layer of nickel. The coating has been made by TTS s.r.o., Prague, Czech Republic. The maximum grazing angle β is equal to 19.1 mrad = 1.09°.

The mirror plates are float-glass which has an observable ripple in one direction. This direction was aligned to lateral axis to minimize gradient errors at grazing incidence. At grazing incidence, mirror deformations in lateral axis are less significant because they cause only small shift of the reflection. Mirror deformations in optical axis cause change of reflection angle and therefore they have significant impact on image quality.

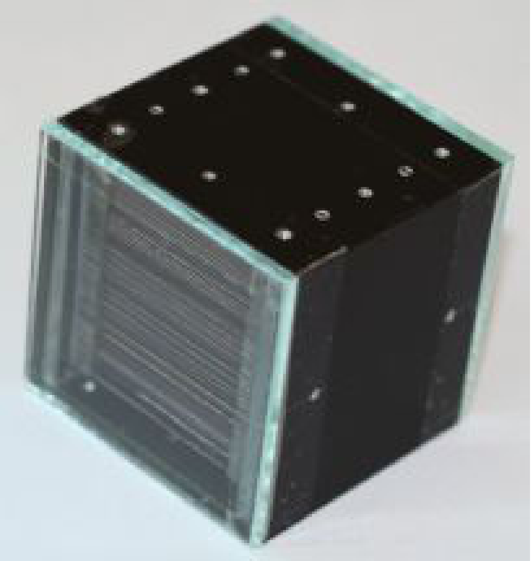

Figure 2. Schmidt lobster eye prototype LTW-51.

3. Glass profile measurements

Profiles of the mirror plates were measured by Fizeau interferometer, see Fig. 3. Mirrors were placed vertically and they were held by a special holder, see Fig. 4. Mirrors are held at corners marked by arrows and four mirrors can be accommodated in the holder.

The internal structure of the holder and a mirror itself is seen in Fig. 3. Because there is a small space around mirrors and there is a small space between mirrors and top part of the holder, the holder itself does not introduce a force on mirrors.

Typical profiles are shown in Fig. 6, Fig. 7. The profiles are of the same mirror but in Fig. 7, the mirror is physically rotated by 90° with respect to Fig. 6. Therefore, the difference between the profiles in figures Fig. 6, Fig. 7 are due to the effect of gravity.

4. Result of simulations for ideally assembled optics of ideally flat mirrors

First, the simulations of LTW-1 were performed with the assumptions that mirrors are idealy flat and ideally assembled. The simulations were performed via software package QSOFT developed at University of Leicester. This and all other presented simulations were performed for aligned optics with on-axis

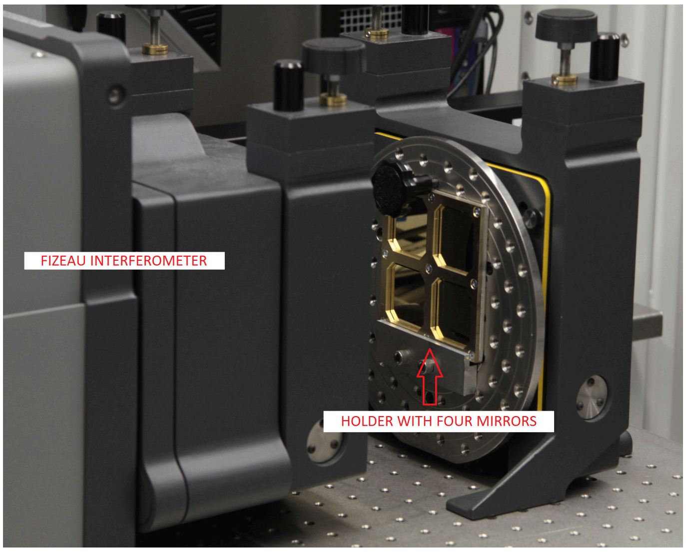

Figure 3. Setup for mirror profiles measurement using the Fizeau interferometer.

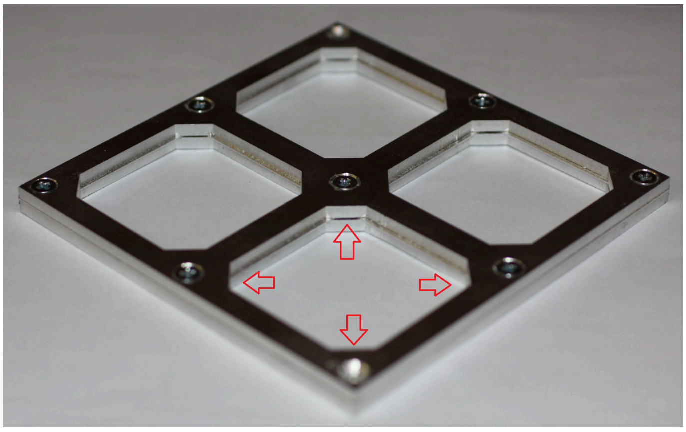

Figure 4. Holder for mirrors profile measurement.

source. As model of reflectivity, a look-up table of data acquired at Henke (2017) were used. The same incident energy of 1490 eV was used in the simulations and in the experiment.

The resulting simulated image for a perfect optic is shown in Fig. 8. The FWHM of the line focus equals 0.4 mm. This and all FWHM values in this paper were estimated as average of result of five simulations made with resolution

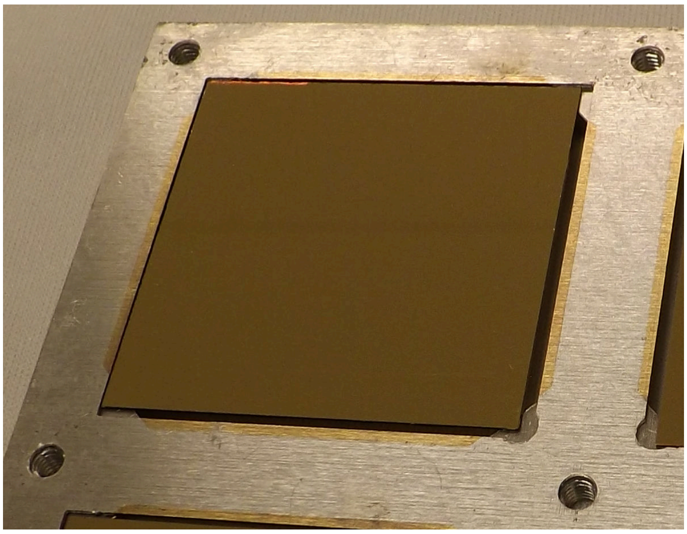

Figure 5. Mirror and holder internal structure detail.

of 0.1 mm. The average was rounded to tenths of mm. The image in Fig. 8 represents a typical image acquired by one-dimensional SLE for parallel incoming beam. The bright central line represents the line focus. It is formed by single reflections. Fainter lines laying beside the central line are formed by unreflected rays that come through the SLE directly. The outer strips are unreflected rays that penetrate between the outer plates and the housing.

5. Simulation of mirror intrinsic deformations

Measured mirror intrinsic deformations are irregular and differ from mirror to mirror. Usually, profile data were not acquired over the entire mirror area. For this reason, measured data cannot be directly used for modelling of mirror intrinsic deformations.

However, it was found that intrinsic mirror deformation in worse axis has wavelengths of around 20 mm and amplitudes (peak to peak) around 1 μm as seen in the Fizeau data. As a first approximation, a sine wave was chosen to model the deformation in one axis. I.e. the function $\delta = A\sin(x/\lambda - \phi)$ was used as a model of the deformation. A Gaussian distribution of mean value 0.5 μm and $\sigma = 0.125$ nm was used for random generation of amplitude A. For period λ, Gaussian distribution of mean value 20 mm and $\sigma = 5$ mm was used. For generating of phase ω, uniform distribution on interval $[0, 2\pi)$ was used. These numbers were individually generated for each mirror.

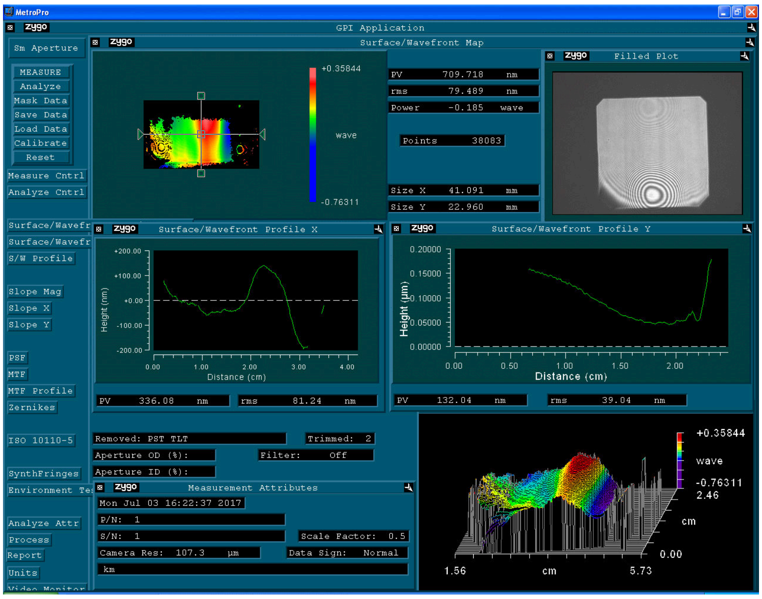

PV 709.718 nm
rms 79.489 nm
Power -0.185 wave
Points 38083
Size X 41.091 mm
Size Y 22.960 mm

PV 336.08 nm
rms 81.24 nm

PV 132.04 nm
rms 39.04 nm

Removed: PST TLT
Trimmed: 2
Aperture OD (%):
Filter: Off
Aperture ID (%):

Mon Jul 03 16:22:37 2017
P/N: 1
S/N: 1
Scale Factor: 0.5
Camera Res: 107.3 µm
Data Sign: Normal
km

Figure 6. Typical mirror profiles. In the left-hand middle panel, there is the lateral profile. In the right-hand middle pannel, there is the optical axis profile.

If the deformations are placed along the lateral axis, the deflections are so small and not seen in the result of simulations and the FWHM is unchanged. If the deformations are placed along the optical axis, FWHM increases to 0.6 mm. The resulting image is shown in Fig. 9.

6. Simulation of mirror positioning errors

Four randomly generated numbers were used to represent shifts in the corners of the mirrors. These shifts were individually generated for each mirror. They were added to values representing ideal positions of corners. Between the corners, linear interpolation was used to represent the profile of mirrors. This approach simulates first order mirror deformations that can be caused by the mirror supporting structure. A Gaussian distribution with various values of σ and zero mean was used. Results are shown in Fig. 10. Deviations in mirror positioning introduce tilt errors in the mirrors which cause a blurring of the line focus.

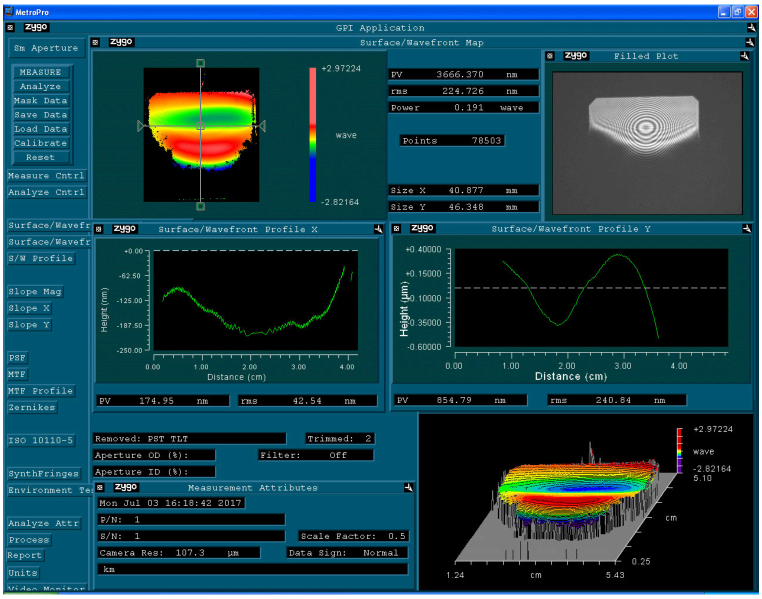

PV 3666.370 nm
rms 224.726 nm
Power 0.191 wave
Points 78503
Size X 40.877 mm
Size Y 46.348 mm

PV 174.95 nm
rms 42.54 nm

PV 854.79 nm
rms 240.84 nm

Removed: PST TLT
Trimmed: 2
Aperture OD (%):
Filter: Off
Aperture ID (%):

Mon Jul 03 16:18:42 2017
P/N: 1
S/N: 1
Scale Factor: 0.5
Camera Res: 107.3 µm
Data Sign: Normal
km

Figure 7. Typical mirror profiles. In the left-hand middle pannel, there is the optical axis profile. In the right-hand middle pannel, there is the lateral profile.

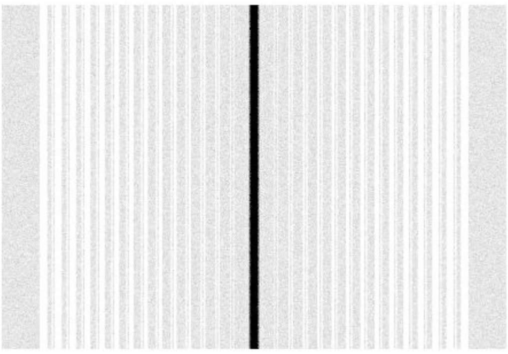

Figure 8. Results of simulation for ideally assembled SLE with ideally flat mirrors.

7. Experimental results with LTW-51

The Prototype lobster eye LTW-51 was tested at the XACT facility (Artale et al., 2004; Barbera et al., 2006) in the 35 m long X-ray beam-line. X-ray image at the focal plane has been taken with a microchannel plate (MCP) detector

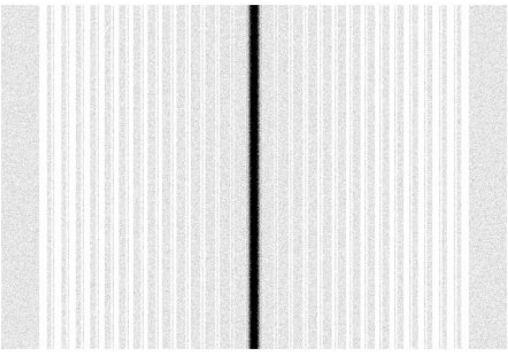

Figure 9. Results of simulation for ideally assembled SLE with mirrors including deformations in the optical axis.

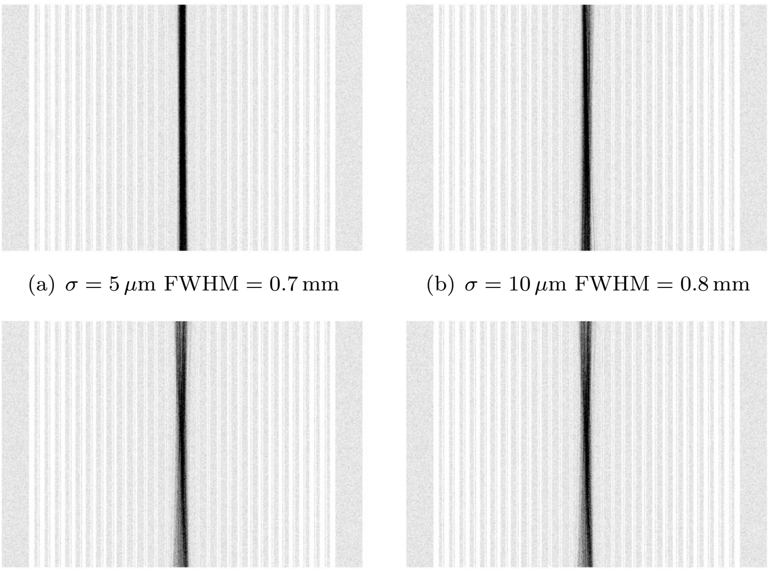

(a) $\sigma = 5\,\mu$m FWHM = 0.7 mm

(b) $\sigma = 10\,\mu$m FWHM = 0.8 mm

(c) $\sigma = 15\,\mu$m FWHM = 1.0 mm

(d) $\sigma = 20\,\mu$m FWHM = 1.3 mm

Figure 10. Simulation of deviations of supporting structure.

featuring a $100\,\mu$m spatial resolution at energy 1490 eV. The setup in the test chamber is shown in Fig. 11.

The image acquired at centered, on-axis position is shown in Fig. 12(a) FWHM reaches 0.7 mm. This value of FWHM was obtained in simulations us-

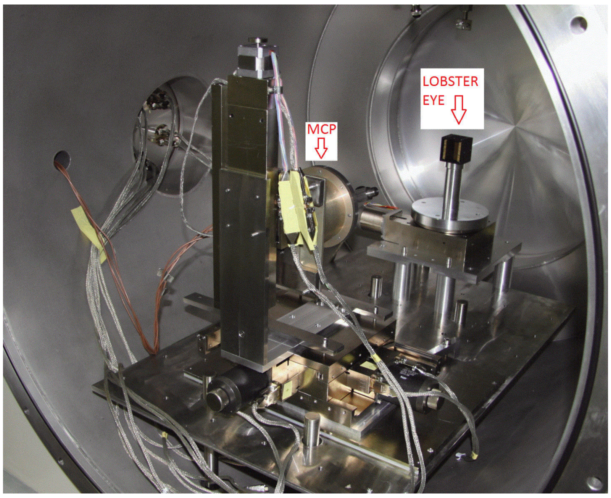

Figure 11. Test chamber setup.

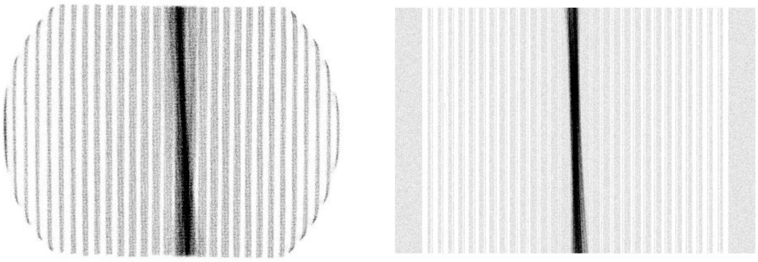

(a) Experimental image.

(b) Simulation including skew error $10\,\mu$m and mirror positioning error $\sigma = 5\,\mu$m.

Figure 12. Final results.

ing a positioning error of $\sigma = 5\,\mu$m. The small skew is caused by position shift between opposite parts of supporting structure and it was estimated as $10\,\mu$m. This skew was simulated as systematic shift of mirror corner points. The above values were used for the final simulation with the skew and supporting structure inaccuracy included. The result is shown in Fig. 12(b).

8. Conclusions

The principal manufacturing errors of Schmidt lobster eye have been described and simulated.

For a size of 51 cm focal length, 37 mm mirror size and ca. 1 mm mirror pitch, the results indicate that the critical task is to place mirrors into their ideal positions. To achieve the theoretically possible angular resolution, micron or submicron accuracy are necessary.

The glass employed shows significantly different deformations in different axes. The current results indicate that glass deformations are less significant or they are not significant if they are aligned laterally.

Acknowledgements. For the financial support, we thank to AHEAD (Integrated Activities in the High Energy Astrophysics Domain) project funded by the European Union as Research and Innovation Action under Grant No: 654215.

We would like to thank the Grant Agency of the Czech Republic for the financial support by grant number 13-33324S.

Authors would like to thank INAF-Osservatorio Astronomico di Palermo for providing the use of the X-ray beam-line for the experiment.

References

Angel, J. R. P., Lobster eyes as X-ray telescopes. 1979, *Astrophys. J.*, **233**, 364, DOI: 10.1086/157397

Artale, M. A., Barbera, M., Collura, A., et al., Calibration of the XRT-SOLARB flat mirror samples at the XACT Facility of INAF-OAPA. 2004, in Proc. SPIE, Vol. **5488**, *UV and Gamma-Ray Space Telescope Systems*, ed. G. Hasinger & M. J. L. Turner, 440–448

Baca, T., Platkevic, M., Jakubek, J., et al., Miniaturized X-ray telescope for VZLUSAT-1 nanosatellite with Timepix detector. 2016, *Journal of Instrumentation*, **11**, C10007, DOI: 10.1088/1748-0221/11/10/C10007

Barbera, M., Candia, R., Collura, A., et al., The Palermo XACT facility: a new 35 m long soft x-ray beam-line for the development and calibration of next-generation x-ray observatories. 2006, in Proc. SPIE, Vol. **6266**, *Society of Photo-Optical Instrumentation Engineers (SPIE) Conference Series*, 62663F

Fraser, G. W., Brunton, A. N., Bannister, N. P., et al., LOBSTER-ISS: an imaging x-ray all-sky monitor for the International Space Station. 2002, in Proc. SPIE, Vol. **4497**, *X-Ray and Gamma-Ray Instrumentation for Astronomy XII*, ed. K. A. Flanagan & O. H. W. Siegmund, 115–126

Gorenstein, P., Large-angle observatory with energy resolution for synoptic x-ray studies (LOBSTER-SXS). 2011, in Proc. SPIE, Vol. **8147**, *Society of Photo-Optical Instrumentation Engineers (SPIE) Conference Series*, 81471O

Henke. 2017, http://henke.lbl.gov/optical_constants/

Petre, R., Camp, J., Barthelmy, S., et al., ISS-Lobster: a low-cost wide-field X-ray transient detector on the ISS. 2015, in *APS Meeting Abstracts*

Pina, L., Hudec, R., Inneman, A., et al., X-ray monitoring for astrophysical applications on Cubesat. 2015, in Proc. SPIE, Vol. **9510**, *EUV and X-ray Optics: Synergy between Laboratory and Space IV*, 951005

Schmidt, W. K. H., A proposed X-ray focusing device with wide field of view for use in X-ray astronomy. 1975, *Nuclear Instruments and Methods*, **127**, 285, DOI: 10.1016/0029-554X(75)90501-7

Tichý, V., Barbera, M., Collura, A., et al., Tests of lobster eye optics for small space X-ray telescope. 2011, *Nuclear Instruments and Methods in Physics Research A*, **633**, S169, DOI: 10.1016/j.nima.2010.06.157

Tichý, V., Burrows, D. N., Prieskorn, Z., & Hudec, R., Optics for nano-satellite X-ray monitor. 2015, *Baltic Astronomy*, **24**, 243

Tichý, V., Hromčík, M., Hudec, R., et al., Small x-ray telescope based on lobster eye x-ray optics and pixel detector. 2009a, in Proc. SPIE, Vol. **7360**, *EUV and X-Ray Optics: Synergy between Laboratory and Space*, 736011

Tichý, V., Hromčík, M., Hudec, R., et al., Tests of Lobster-Eye Optics for a Small X-Ray Telescope. 2009b, *Baltic Astronomy*, **18**, 362

Šaroun, J. & Kulda, J., MC ray-tracing optimization of lobster-eye focusing devices with RESTRAX. 2006, *Physica B Condensed Matter*, **385**, 1250, DOI: 10.1016/j.physb.2006.06.022

Contrib. Astron. Obs. Skalnaté Pleso **48**, 416 – 420, (2018)

Image processing of historical astronomical plates

P. Skala[1] **and R. Hudec**[1,2]

[1] *Czech Technical University in Prague,*
Technicka 2, Prague 166 27, Czech Republic
(E-mail: skalape4@fel.cvut.cz)
[2] *Engelhardt Astronomical observatory, Kazan Federal University,*
Kremlyovskaya street 18, 420008 Kazan, Russian Federation

Received: December 17, 2017; Accepted: February 21, 2018

Abstract. Many fields of X–ray astrophysics require multifrequency data including optical. Long-term data, such as provided by data archives, have special value. Historical astronomical plates were main source of data for more than century, not only for photometry, but also for spectroscopy. There are still millions of plates worldwide which have never been processed by modern computers. There are some standard ways how to process images applicable on astronomic plates. But also many specific methods that must be developed for processing of plates.

Key words: Historical – Plates – Astrometry

1. Introduction

Historical continuity of observation is the main value of the astronomical plates nowadays. For more than century emulsion on glass plates served as main tool for image acquisition. Due to poor sensitivity, long exposures and large aperture were mandatory. Combination with wide field telescope caused distortion and other aberrations at the edges of the image. Then after evaluation, plates were stored in archives. For long term archivation certain conditions must be met. Low humidity and constant temperature as well as special folders are more or less exceptions. For these reasons many of the plates suffers from fungi, golden illness, emulsion peeling and others complications, that reduces image quality and plates durability. For this reason quick method of digitalization is needed, as the emulsion degradation can be fast.

For digitalization, Nikon D800E with high–quality lens was used. With resolution of 36 MPx it can yield high enough pixel density compared to grain of emulsion of middle sized astronomic al plates (Hudec & Hudec, 2013). For very small plates and negatives, such as spectral plates, the method provides very small pixel sizes. Plates are put on specialized lighting panel and after focusing and adjusting procedure many plates can be quickly photographed (Hudec & Hudec, 2014a). Not only glass plates but also photographic emulsions on plastics (planfims) can be digitized this way. The method is very fast and effective, one can easily digitize up to 1 000 plates in just one day, significantly more than can be achieved with another plate digitizing methods, e.g. plate scanners (which in addition have different scanning quality for each axis due to moving parts). So far, more than 30 000 astronomical plates (not only direct images but also low–dispersive spectral images and spectra) were digitized by our team with this method. For the detailed technique and hardware description see (Hudec & Hudec, 2014b).

After digitalization, phase of data restoration follows. Image processing is complicated by fact that telescope used for acquisition usually introduces some small distortion, but when the plates are digitalized by camera, then distortion of lenses is introduced too. For this reason chessboard test image is photographed as target for lens distortion removal. Also when plates doesn't fill the image, then automatic cropping is applied to save archive space. Typical digitalized image is shown in Fig. 1.

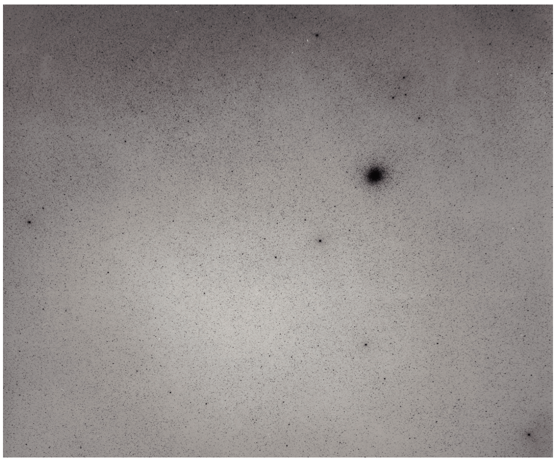

Figure 1. Digitalized and cropped image of M22 star cluster. Field of view is 200×240 arcminutes. Focal length is 310 mm.

2. Astrometric calibration

First experiments were made with astrometric calibration to verify precision of digitalization. WCS header (Calabretta & Greisen, 2002) was created using Astrometry.net (Lang et al., 2010). This service enables usage of linear coordinates but also tweak coordinates using second or higher polynomials. As Fig. 2 shows image is well fitted using even only linear calibration. However, apparent trend is visible in right ascension meantime declination axis is very precisely fitted.

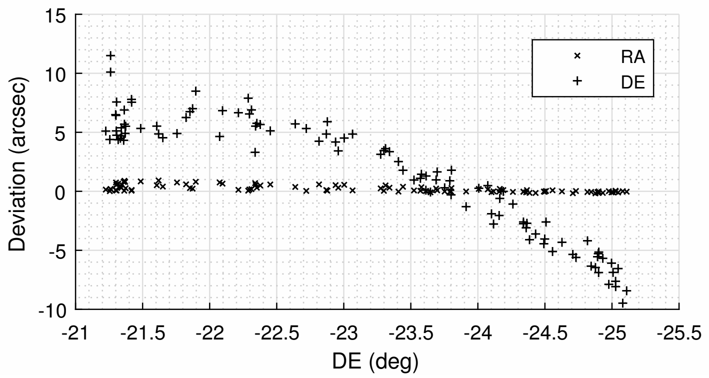

Figure 2. 3D plot of angular deviations from linear astrometric solution view from declination - deviation plane. Right ascension axis is oriented towards inwards.

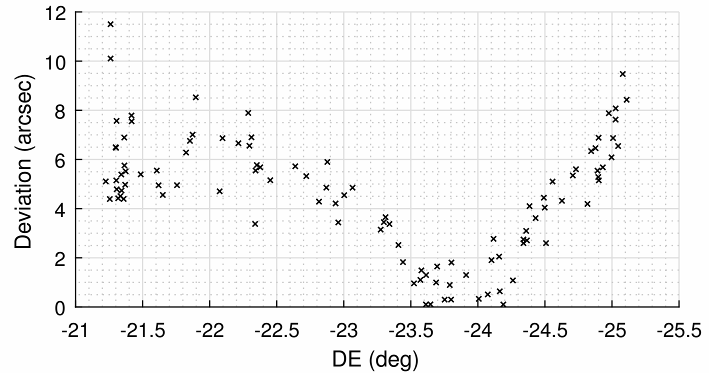

Figure 3. 3D plot of angular deviations from linear astrometric solution combined data RA and DE view from declination - deviation plane. Right ascension axis is oriented towards inwards.

In the Fig. 3 quadratic sum of deviations both RA and DE is shown. In Fig. 4 we show the positional residuals if a third order polynomial is used, together with the stars used to compute the astrometric solution. Evident trend is recognized again. It is clear that for really precise coordinates retrieval SIP (Simple Image Polynomial) of second or even third order should be used. But problem is with FITS WCS header standards. None of the standard programs tested fully support usage of SIP – Aladin, DS9 (Smithsonian Astrophysical Observatory, 2000; Bonnarel et al., 2000). Therefore next work will be put on tool for coordinates retrieval and evaluation.

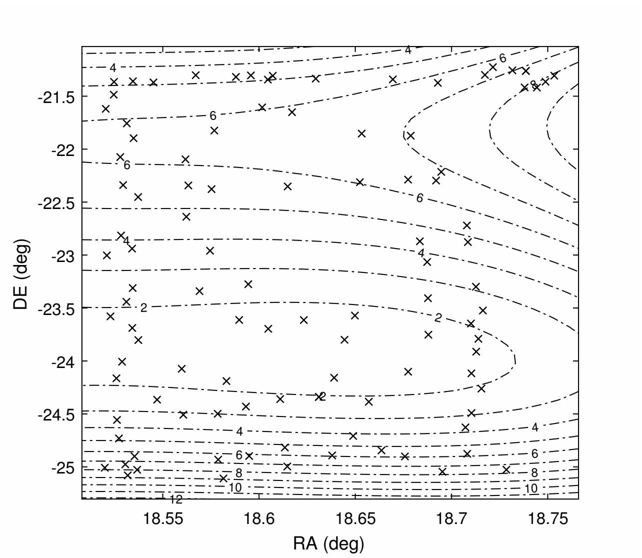

Figure 4. Contour plot of angular deviations in arcseconds combined from both RA and DE with measured stars marked.

3. Conclusion

With no really dedicated software for astronomical plates processing, we are at beginning of process to design and implement all procedures ourselves. Process of digitalization by digital camera gives good results and astrometry can be done with enough precision to identify targets in catalogs. In future we plan to implement SIP to increase precision in corners.

Acknowledgements. This work was supported by the Grant Agency of the Czech Technical University in Prague, grant No.SGS16/169/OHK3/2T/13.

References

Bonnarel, F., Fernique, P., Bienaymé, O., et al., The ALADIN interactive sky atlas. A reference tool for identification of astronomical sources. 2000, *Astron. Astrophys., Suppl.*, **143**, 33, DOI: 10.1051/aas:2000331

Calabretta, M. R. & Greisen, E. W., Representations of celestial coordinates in FITS. 2002, *Astron. Astrophys.*, **395**, 1077, DOI: 10.1051/0004-6361:20021327

Hudec, R. & Hudec, L., Finding Hidden Treasures: Investigations in US Astronomical Plate Archives. 2013, *Acta Polytechnica*, **53**, 23

Hudec, R. & Hudec, L., Alternative technique for astronomical plate scanning. 2014a, in *Astroplate 2014*, 65

Hudec, R. & Hudec, L., US Astronomical Photographic Data Archives: Hidden Treasures and Importance for High-Energy Astrophysics. 2014b, in *Multifrequency Behaviour of High Energy Cosmic Sources*, 316–319

Lang, D., Hogg, D. W., Mierle, K., Blanton, M., & Roweis, S., Astrometry.net: Blind Astrometric Calibration of Arbitrary Astronomical Images. 2010, *Astron. J.*, **139**, 1782, DOI: 10.1088/0004-6256/139/5/1782

Smithsonian Astrophysical Observatory. 2000, SAOImage DS9: A utility for displaying astronomical images in the X11 window environment, Astrophysics Source Code Library

Contrib. Astron. Obs. Skalnaté Pleso **48**, 421 – 429, (2018)

Investigation of the long-term activity of the binary X-ray sources with the planned satellites

V. Šimon[1,2]

[1] *Czech Technical University in Prague, Technická 2, 16627 Prague, Czech Republic (E-mail: simonvo1@fel.cvut.cz)*

[2] *Astronomical Institute, The Czech Academy of Sciences, 25165 Ondřejov, Czech Republic (E-mail: simon@asu.cas.cz)*

Received: December 20, 2017; Accepted: March 26, 2018

Abstract. Monitors of X-ray emission are important instruments for observing the long-term activity of cosmic sources on the long timescales (e.g. years). We show the perspectives and possibilities of observing the selected types of X-ray binary sources with the planned satellites *THESEUS* and *eXTP*. The hardness of the X-ray spectrum largely determines the observability of a given object (or a type of objects) with a monitor operating in the specific band. We show the perspectives of detecting and observing outbursts in the soft X-ray transients with the hard X-ray monitors *eXTP*/WFM and *THESEUS*/XGIS. Their broad energy bands and energy resolution will enable to detect the outbursts and the complex spectral changes during these events. We also show the perspectives of observing the binary supersoft X-ray sources with the planned *THESEUS*/SXI. These sources sometimes have the luminosity close to the Eddington limit but their X-ray emission is usually below the band used by the monitors.

Key words: Accretion, accretion disks – X-rays: binaries – stars: neutron – stars: black holes – white dwarfs

1. Introduction

Monitors of X-ray emission are important instruments for observing the long-term activity of cosmic sources on the long timescales (e.g. years and decades). Hardness of the X-ray spectrum determines the observability of a given object (or a type of objects) with a monitor operating in the specific band, so the X-ray emission of some types of objects can remain undetected by some instruments. We show the perspectives and possibilities of observing this activity in the selected types of such sources with the planned satellites *THESEUS* and *eXTP*.

2. Hard X-ray observing with *eXTP*/WFM and *THESEUS*/XGIS

WFM monitor (a set of three coded mask wide field units) onboard *eXTP*, planned to observe in the 2–50 keV band (Zhang et al., 2016), will be suitable for observing the long-term activity of X-ray binaries. Also *THESEUS*/XGIS (2 keV–20 MeV) (Campana et al., 2016) can be used for this purpose because X-ray binaries (the systems in which the neutron star (NS) or the black hole (BH) accretes matter from its close companion (Lewin et al., 1995)) often produce hard X-ray emission (e.g. with energy E of tens of keV), well within the band of WFM and XGIS. The continuum emission (often a composition of the emission components from the inner disk region (thermal radiation) and from the Comptonizing cloud around the accretor – inverse Compton scattering) of these objects by far dominates the X-ray spectrum (e.g. Lewin et al. (1995)).

What can we expect from the data from X-ray monitors? The characteristic features of the long-term activity of a type of X-ray binaries, the outbursts of the soft X-ray transients (SXTs), caused by a thermal-viscous instability of the accretion disk (e.g. Dubus et al. (2001)), can be investigated even in a single-band X-ray light curve (monitors typically observe X-rays with E of a few keV). Even some model predictions regarding to the mass accretion rate (approximated as the soft X-ray flux) are already available in a model of Dubus et al. (2001). These spectral variations are reflected in the differences between the X-ray light curves in various X-ray bands. The light curves from the planned WFM or XGIS observations, divided into several energy sub-bands, will be very important because their broad energy band and their energy resolution will enable to resolve the complex changes during the outbursts.

As an illustration of the features of the long-term activity of the SXTs, we show an outburst of Aql X-1 (Koyama et al., 1981; Chevalier & Ilovaisky, 1991) in Fig. 1. It is a combination of the one-day means of the data from the monitors *ISS*/MAXI (Matsuoka et al., 2009) and *Swift*/BAT (Krimm et al., 2013).

Fig. 1b shows the time evolution of the one-day means of the hardness ratios. These ratios, determined from the MAXI data, are $HR1 = \frac{I_{\rm B}}{I_{\rm A}}$ and $HR2 = \frac{I_{\rm C}}{I_{\rm B}}$. The flux $I_{\rm A}$ is for the 2–4 keV band, $I_{\rm B}$ for the 4–10 keV band, and $I_{\rm C}$ for the 10–20 keV band from Fig. 1a. A large difference between the light curve of the outburst in the 15–50 keV band (Fig. 1c) and in the softer bands in Fig. 1a shows the importance of monitoring in the very broad bands like those of *eXTP*/WFM and *THESEUS*/XGIS. Their data can be used for an investigation of the mutually different X-ray light curves in the different E (and the hardness ratios) of such events. This monitoring in a very broad energy band also enables to determine the color vs. color diagrams from the X-ray light curves (Asai et al., 2016).

A division of the observed X-ray emission into several sub-bands can help to assess the role of the emission mechanisms and their evolution with time. Of course, the bands used for Fig. 1 can be modified for the sub-bands into which the WFM or XGIS measurements can be divided. Since most features of the long-term activity occur on the timescales longer than a day, the features in the light curves of outbursts can be well defined even when the data are sampled and binned in time (e.g. when the one-day means are used). This binning enables to increase the signal-to-noise ratio.

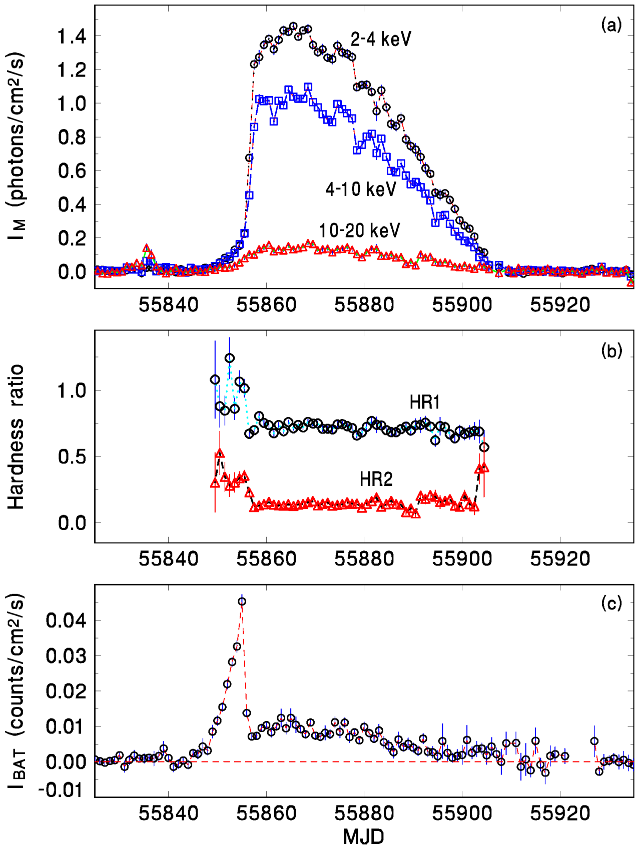

Figure 1. **(a)** Light curve of an example of the outburst of the soft X-ray transient Aql X-1 (MAXI data). Time is expressed as the Modified Julian Date (MJD). Energies of the individual bands are marked. **(b)** The hardness ratios $HR1$ and $HR2$. They are explained in the text. **(c)** Light curve of Aql X-1 in the 15–50 keV band of *Swift*/BAT.

Since both the width and the position of the peak of the outburst largely differ for various energy bands (2–20 keV versus 15–50 keV) (Fig. 1), the large variations of the emitting regions during the outburst are suggested. Ono et al. (2017) present a model consisting of a multi-color disk (MCD) and a Comptonized blackbody, with the flux of the MCD making the dominant peak of the whole outburst. As a result, the light curves in the different X-ray bands differ from each other because of the different dominant emission regions and processes.

The conditions in the disks of the SXTs can be affected by the presence of a very hot inner disk region; it can act as an irradiating source during outburst and is thought to modify the disk structure (e.g. Dubus et al. (2001)). This configuration very strongly influences the X-ray light curve of the outburst. Also the determination of the hardness ratios is important to show the time evolution of the emitting regions. The accompanying variations between the light curves in the different bands of WFM will be important for this research. The duration of the outbursts of the SXTs is from days to months, so even a one-day binning of the WFM data will be sufficient.

The light curve in Fig. 1 shows no clear sign of an exponential decay of the outburst of Aql X-1. This suggests no irradiation of the disk, when the model of Dubus et al. (2001) is applied. This is an important feature because the decaying branches observed in the 1.5–12 keV band by the *RXTE*/ASM monitor (Levine et al., 1996) differed for the individual outbursts in a similar object, 4U 1608–52 (Šimon, 2004).

Investigations of the recurrence time of the outbursts of the SXTs, $T_{\rm C}$, require the X-ray monitors. The reason is that while the typical durations of the outbursts of the SXTs are from weeks to months, $T_{\rm C}$ are from months to decades (e.g. Lewin et al. (1995)). It is therefore reasonable to expect that *eXTP*/WFM and *THESEUS*/XGIS will observe a series of outbursts of some SXTs with frequent outbursts ($T_{\rm C}$ of less than 1 year) like e.g. Aql X-1 (e.g. Šimon (2002)) or 4U 1608-52 (e.g. Šimon (2004)). Because a given monitor is able to operate for several years, even a basic knowledge of the time evolution of $T_{\rm C}$ of most SXTs requires the data from several monitors.

The individual outbursts of a given SXT can have very different energy outputs (fluences) (fluence is the flux integrated over the duration of the whole outburst in a given band). This parameter, measurable by the monitors, sometimes largely differs even for the neighboring outbursts but this difference of the energy output does not influence the length of $T_{\rm C}$ of a given SXT. In the interpretation, only a small fraction of mass of the accretion disk is accreted during a single outburst in such a case. The analyses of Šimon (2002) and Šimon (2017) show that the length of $T_{\rm C}$ displays episodes both of a decrease and an increase of the length. The available data show that the length of $T_{\rm C}$ varies much more gradually than the fluence or the peak intensity of the outbursts.

Another important role of the X-ray monitors sensitive in a broad band are the observations of the cycles like the one superimposed on a very long (about 600 d) outburst of the LMXB SXT XTE J1701–462. Its length displayed a large and gradual increase from ∼16 to ∼26 days. Since this cycle was detected only by *RXTE*/ASM (1.5–12 keV), but not by *Swift*/BAT (15–50 keV), it was interpreted as coming only from the component emitting the soft X-rays (a superorbital cycle caused by tilting and warping of the irradiated disk) (Šimon, 2015). The complexity of the detected features of the time variations was caused by the fact that this source emitted X-rays from several regions (Homan et al., 2007; Lin et al., 2009).

3. Supersoft X-ray sources with *THESEUS*/SXI

The binary supersoft X-ray sources are the very unique emitters because their matter is accreted onto the white dwarf (WD) from a close companion at an extremely high rate. This leads to steady-state thermonuclear burning of accreted hydrogen on the surface of the WD (van den Heuvel et al., 1992). It largely contributes to their luminosity.

An X-ray emission of the very hot atmosphere of the WD (with the spectrum similar to black body and the luminosity even at the Eddington limit) in the band with $E < 1.5\,\mathrm{keV}$ is produced (Popham & di Stefano, 1996). In the absence of absorption which steeply increases with the decreasing E (Morrison & McCammon, 1983), the peak luminosity occurs at $E \approx 0.3\,\mathrm{keV}$. The intensity then steeply decreases with growing E, being by more than about three orders of magnitude smaller at $E \approx 1.5\,\mathrm{keV}$.

The observed anti-correlation of the optical and soft X-ray intensities in the long-term activity of some of these objects is interpreted in terms of the very large sensitivity of the supersoft X-ray emission to two effects: absorption intrinsic to the source (Greiner & van Teeseling, 1998), and changes of the radius of the hydrogen burning envelope on the WD (Reinsch et al., 2000). A division of the observed X-ray emission into several energy bands can help to assess the role of the above-mentioned mechanisms and their evolution with time. However, this very soft X-ray emission is beyond the band of sensitivity of most X-ray monitors, so the investigations of the long-term activity of these objects are usually conducted in the optical band.

V Sge with the orbital period $P_{\mathrm{orb}} = 0.514195\,\mathrm{d}$ (Herbig et al., 1965) can serve as an example of the complex long-term activity of the transient supersoft X-ray sources (Hachisu & Kato, 2003). The optical luminosity, generated mainly by the accretion disk, is roughly anti-correlated with the X-ray luminosity (mainly from the hydrogen burning) (Greiner & van Teeseling, 1998). The positions of their X-ray measurements are included in Fig. 2a. When the X-ray spectrum of V Sge in the 0.1–2.4 keV band is “very soft”, the X-ray luminosity is significantly higher than when it is “hard”.

Transitions between the states of activity of V Sge are usually considerably faster than the duration of the state, so an observing within a given state is expected by *THESEUS*/SXI (O’Brien et al., 2018) (Fig. 2a). The WWZ-transform (method of Foster (1996)) shows an evolution of activity with time (Fig. 2b). The value of WWZ indicates whether or not there is a periodic fluctuation at a given time at a given frequency. Although the transitions between the high and low states are cyclic (Fig. 2b), this cycle displays a complicated evolution and is only intermittently present. These transitions sometimes even temporarily disappear (Šimon & Mattei, 1999).

Also RX J0513–69 displays the long-term activity similar to that of V Sge. It is detectable as a very soft X-ray source only during its recurrent optical low-state episodes (Reinsch et al., 2000). The anti-correlation of the very soft

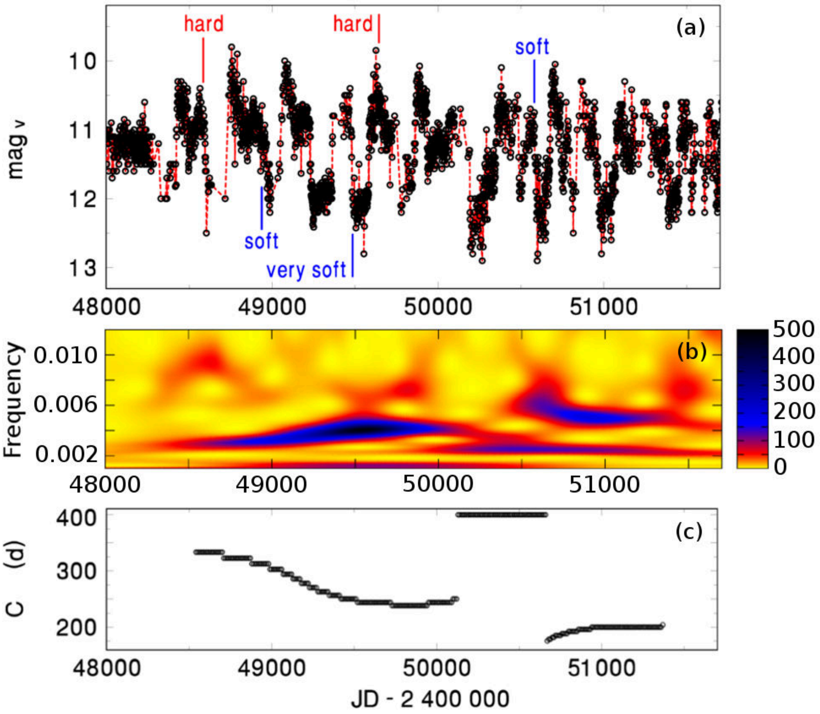

Figure 2. **(a)** The optical long-term activity of the supersoft X-ray source V Sge (one-day means of the AAVSO and AFOEV data (Kafka, 2016)). The times and characteristics of the X-ray spectra in the *ROSAT* observations are from Greiner & van Teeseling (1998). **(b)** Cycles in the high-low state transitions (method of the WWZ–transform of Foster (1996)). Frequency is given in d^{-1}. The color scale represents the values of WWZ (see the scale). The higher the WWZ value, the better defined the cycle-length. **(c)** The best cycle-length C measured in days. Only the segments with the amplitude larger than 38 percent of its peak value were included. Updated from Šimon (2016).

X-ray and the optical fluxes argues for a multifrequency monitoring e.g. with the instruments SXI (O'Brien et al., 2018) and IRT (Götz et al., 2018) onboard *THESEUS*. Monitoring of various binary supersoft X-ray sources can shed more light on the activity of such objects and its more structured classification.

We also emphasize that it is important to answer the question in which states of activity such objects are detectable in the X-ray band and how this activity evolves on the long timescales (months, years). The monitor which is planned to observe in the band with $E < 1.5\,\mathrm{keV}$ can help us to detect the long-term activity of these sources in the X-ray band.

4. Conclusions

The detectability of an object strongly depends on the energy band of the X-ray monitor. We also emphasize that the soft X-ray activity of a given source can be different from that in the hard X-ray band.

The hard X-ray monitors (*THESEUS*/XGIS, *eXTP*/WFM) are suitable for observing the NS and the BH accretors. The soft X-ray monitor *THESEUS*/SXI can be used also for observing the binary supersoft X-ray sources.

The outbursts of the SXTs are usually unpredictable. Their average T_{C} and its complicated variations can be determined only from a long (years to decades) series of observations. Since the time of operation of a given monitor is often several years, also a follow-up observing with the future monitors is very needed.

The light curves of the SXT outbursts in a given X-ray band differ for the individual events even in the same object. The large structural changes of the emitting regions occur during the outburst (e.g. the time of the peak flux of the far X-ray emission (15–50 keV) can occur when the soft X-ray flux (e.g. 2–4 keV) is still rising to its peak).

The near-IR monitor *THESEUS*/IRT is suitable for observing all types of binary X-ray sources, but it appears to be very important also for detecting and/or observing of the optical counterparts of X-ray transients and the correlations of the optical and X-ray states in the binary supersoft X-ray sources.

Acknowledgements. This study was supported by grant 13-33324S provided by the Grant Agency of the Czech Republic. This research has made use of the observations provided by the ASM/RXTE team, public data from Swift/BAT transient monitor provided by the Swift/BAT team, and the MAXI team. This research has also made use of the observations from AAVSO International database (USA) and the AFOEV database (France). I thank the variable star observers worldwide. I used the code developed by Dr. G. Foster and available at www.aavso.org/winwwz. I also thank Prof. Petr Harmanec for providing me with the code HEC13. The Fortran source version, compiled version and brief instructions on how to use the program can be obtained at http://astro.troja.mff.cuni.cz/ftp/hec/HEC13/

References

Asai, K., Mihara, T., Mastuoka, M., & Sugizaki, M., Hard-tail emission in the soft state of low-mass X-ray binaries and their relation to the neutron star magnetic field. 2016, *PASJ*, **68, Issue 4**, id.50, DOI: 10.1093/pasj/psw048

Campana, R., Fuschino, F., Labanti, C., et al., A compact and modular x- and gamma-ray detector with a CsI scintillator and double-readout Silicon Drift Detectors. 2016, in Proceedings of the SPIE, Vol. **9905**, *Proceedings of the SPIE*, 10

Chevalier, C. & Ilovaisky, S. A., Discovery of a 19-hour period in Aquila X-1. 1991, *A&A*, **251**, L11

Dubus, G., Hameury, J.-M., & Lasota, J.-P., The disc instability model for X-ray transients: Evidence for truncation and irradiation. 2001, *A&A*, **373**, 251, DOI: 10.1051/0004-6361:20010632

Foster, G., Wavelets for period analysis of unevenly sampled time series. 1996, *Astron. J.*, **112**, 1709, DOI: 10.1086/118137

Götz, D., Boulade, O., Cordier, B., et al., The Infra-Red Telescope on board the THESEUS mission. 2018, in *the Proceedings of the THESEUS Workshop 2017 (http://www.isdc.unige.ch/theseus/workshop2017.html)*, Journal of the Italian Astronomical Society (Mem.SAIt)

Greiner, J. & van Teeseling, A., On the X-ray properties of V Sge and its relation to the supersoft X-ray binaries. 1998, *A&A*, **339**, L21

Hachisu, I. & Kato, M., A Limit Cycle Model For Long-Term Optical Variations of V Sagittae: The Second Example of Accretion Wind Evolution. 2003, *Astrophys. J.*, **598**, 527, DOI: 10.1086/378848

Herbig, G. H., Preston, G. W., Smak, J., & Paczynski, B., The Nova-Like Variable V Sagittae as a Short-Period Eclipsing Binary. 1965, *Astrophys. J.*, **141**, 617, DOI: 10.1086/148149

Homan, J., van der Klis, M., Wijnands, R., et al., Rossi X-Ray Timing Explorer Observations of the First Transient Z Source XTE J1701-462: Shedding New Light on Mass Accretion in Luminous Neutron Star X-Ray Binaries. 2007, *Astrophys. J.*, **656**, 420, DOI: 10.1086/510447

Kafka, S., Observations from the AAVSO International Database . 2016, in *http://www.aavso.org*

Koyama, K., Inoue, H., Makishima, K., et al., Discovery of X-ray bursts from Aquila X-1. 1981, *Astrophys. J.*, **247**, L27

Krimm, H. A., Holland, S. T., Corbet, R. H. D., et al., The Swift/BAT Hard X-Ray Transient Monitor. 2013, *ApJS*, **209**, 14, DOI: 10.1088/0067-0049/209/1/14

Levine, A. M., Bradt, H., Cui, W., et al., First Results from the All-Sky Monitor on the Rossi X-Ray Timing Explorer. 1996, *Astrophys. J., Lett.*, **469**, L33, DOI: 10.1086/310260

Lewin, W. H. G., van Paradijs, J., & van den Heuvel, E. P. J., X-ray binaries, Cambridge Astrophysics Series, Cambridge, MA: Cambridge University Press. 1995

Lin, D., Remillard, R. A., & Homan, J., Spectral States of XTE J1701 - 462: Link Between Z and Atoll Sources. 2009, *Astrophys. J.*, **696**, 1257, DOI: 10.1088/0004-637X/696/2/1257

Matsuoka, M., Kawasaki, K., Ueno, S., et al., The MAXI Mission on the ISS: Science and Instruments for Monitoring All-Sky X-Ray Images. 2009, *PASJ*, **61**, 999, DOI: 10.1093/pasj/61.5.999

Morrison, R. & McCammon, D., Interstellar photoelectric absorption cross sections, 0.03-10 keV. 1983, *ApJ*, **270**, 119, DOI: 10.1086/161102

O'Brien, P., Bozzo, E., Willingale, R., et al., The Soft X-ray Imager (SXI) on-board the THESEUS mission. 2018, in *the Proceedings of the THESEUS Workshop 2017* *(http://www.isdc.unige.ch/theseus/workshop2017.html)*, Journal of the Italian Astronomical Society (Mem.SAIt)

Ono, K., Makishima, K., Sakurai, S., et al., A hard-to-soft state transition of Aquila X-1 observed with Suzaku. 2017, *PASJ*, **69**, id.23, DOI: 10.1093/pasj/psw126

Popham, R. & di Stefano, R., Accretion Disks in Supersoft X-Ray Sources. 1996, *Lecture Notes in Physics*, **472**, 65, DOI: 10.1007/BFb0102247

Reinsch, K., van Teeseling, A., King, A. R., & Beuermann, K., A limit-cycle model for the binary supersoft X-ray source RX J0513.9-6951. 2000, *A&A*, **354**, L37

Šimon, V., On the recurrence time and outburst properties of the soft X-ray transient Aquila X-1. 2002, *A&A*, **381**, 151, DOI: 10.1051/0004-6361:20011470

Šimon, V., The properties of outbursts and long-term activity of the soft X-ray transient 4U 1608-52 (QX Nor). 2004, *A&A*, **418**, 617, DOI: 10.1051/0004-6361:20040037

Šimon, V., Cataclysmic variables - A research laboratory for accretion processes. 2016, in Proceedings of Science, Vol. **FRAPWS 2016**, *2nd Frontier Research in Astrophysics*

Šimon, V., The long-term activity of dwarf novae and soft X-ray transients. 2017, in *The Golden Age of Cataclysmic Variables and Related Objects - IV*, Proceedings of Science (submitted)

Šimon, V. & Mattei, J. A., The peculiar binary V Sagittae: Properties of its long-term light changes. 1999, *Astronomy and Astrophysics Supplement*, **139**, 75, DOI: 10.1051/aas:1999381

Šimon, V., Evolution of the complicated decaying branch of the very long outburst in XTE J1701-462. 2015, *New Astronomy*, **37**, 26, DOI: 10.1016/j.newast.2014.11.005

van den Heuvel, E. P. J., Bhattacharya, D., Nomoto, K., & Rappaport, S. A., Accreting white dwarf models for CAL 83, CAL 87 and other ultrasoft X-ray sources in the LMC. 1992, *A&A*, **262**, 97

Zhang, S. N., Feroci, M., Santangelo, A., et al., eXTP: Enhanced X-ray Timing and Polarization mission. 2016, in Proceedings of the SPIE, Vol. **9905**, *Proceedings Volume 9905, Space Telescopes and Instrumentation 2016: Ultraviolet to Gamma Ray*, 16

Contrib. Astron. Obs. Skalnaté Pleso **48**, 430 – 436, (2018)

JEUMICO and TRILAMICO: Dimensions of successful Bavarian-Czech cooperation

T. Döhring[1] **and R. Hudec**[2]

[1] *Aschaffenburg University of Applied Sciences,*
Würzburger Strasse 45, 63743 Aschaffenburg, Germany
(E-mail: thorsten.doehring@h-ab.de)
[2] *Czech Technical University in Prague,*
Technicka 2, Prague 166 27, Czech Republic (E-mail: hudecren@fel.cvut.cz)

Received: December 20, 2017; Accepted: February 14, 2018

Abstract. In December 2017 the two projects JEUMICO (an acronym for Joint European Mirror Cooperation) and TRILAMICO (standing for Trilateral Mirror Collaboration) are ending. Different aspects of this Bavarian-Czech collaboration between Aschaffenburg University and the Czech Technical University in Prague are discussed. The multiple dimensions of this cooperation are scientific achievements, public relation measures, internationalization of education, financial aspects, inter-cultural communication, and also the actual political situation within Europe.

Key words: X-ray optics – international – cooperation

1. Introduction

The Bavarian-Czech Academic Agency BTHA, which is a German abbreviation for Bayerisch-Tschechische Hochschulagentur, is a department of the Bavarian Academic Center for Central, Eastern and Southeastern Europe (BAYHOST). BTHA coordinates the bilateral cooperation between Bavaria and the Czech Republic in the field of higher education and science. Thereby funding provided by BTHA includes grants for students visiting the partner country, as well as mobility grants for internships, research travels, or excursions. Moreover significant funding is supporting selected bilateral academic projects and conferences in Bavaria and in the Czech Republic. It is the goal of the Bavarian-Czech Academic Agency to support the academic collaboration in research and education and to contribute to an increased cooperation of the two neighbored countries in general (Hudec & Döhring, 2017).

Aschaffenburg University of Applied Sciences and the Czech Technical University in Prague successfully applied for grants on two joint projects. The JEUMICO project (an acronym for Joint European Mirror Cooperation) was financed via BTHA during 2016 and 2017, based on a joint initiative of the Bavarian State Ministry of Education, Science and Arts and the Ministry of Education, Youth and Sports of the Czech Republic (Hudec & Döhring, 2017).

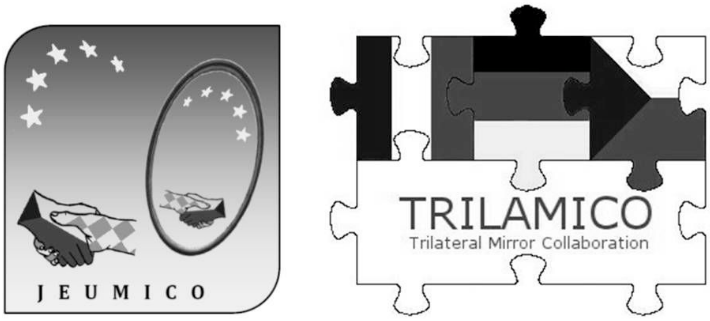

Figure 1. The logo of the projects JEUMICO and TRILAMICO.

The TRILAMICO project (standing for Trilateral Mirror Collaboration) was funded in 2017 by the Bavarian-Czech Academic Agency as part of a wider trilateral collaboration including the Institute Fresnel in Marseille (France). The logos of the two projects are shown in figure 1, depicting the international cooperation. As both projects have been recently finalized successfully, it is time now to resume and to discuss the different dimensions of such collaborations.

2. Technical content and scientific output

Within the bilateral projects JEUMICO and TRILAMICO emphasis is given to the development of innovative thin and very lightweight X-ray mirrors for satellites (Hudec & Döhring, 2017). The mirrors thickness is below 1 mm and they are coated by thin reflective layers (Döhring et al., 2017b). Hereby especially astrophysical applications are considered (Stehlíková et al., 2017). Other topics of cooperative work have been a market study on astronomical filters, the environmental testing of satellite sensors, and the commission of an UV-VIS micro-spectrometer.

Based on a bionic approach we had chosen a special Lobster Eye optics design in Schmidts arrangement, which uses dual reflections to increase the collecting area of astronomical X-ray telescopes (Stehlikova et al., 2017). The individual mirrors of this wide-field telescope are made of flat silicon wafers coated with reflecting iridium (Ir) coatings, as this material is promising high reflectivity in the X-ray range of interest (3 keV to 10 keV). The new optics is designed as a hybrid between two types of reflective optics, of the Kirkpatrick-Baez design, which uses parabolic curved mirrors, and of the Lobster Eye design in Schmidts arrangement, using two sets of flat mirrors. Thereby this hybrid approach consists of two separated mirrors sets, turned for 90 degrees (Stehlikova et al., 2017). Radio frequency (rf) magnetron sputtering technology is available at Aschaffenburg University of Applied Sciences for the mirror coating processes (Döhring

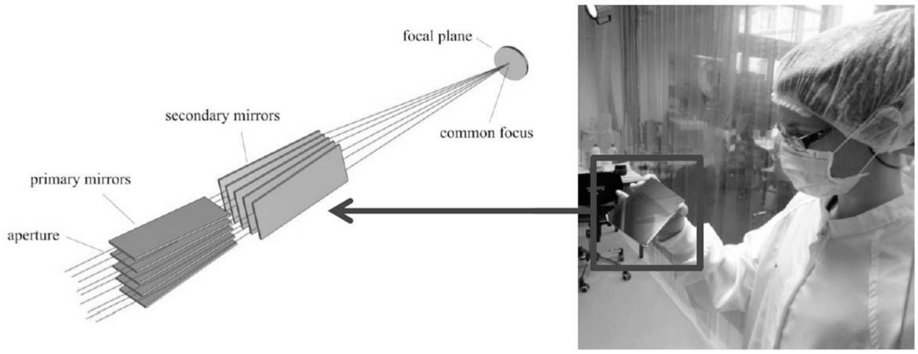

Figure 2. The optics design of a Lobster-Eye telescope.

et al., 2017a). Superpolished silicon wafers have been chosen as substrates for the X-ray mirrors of the Lobster Eye telescope. By applying an intermediate chromium adhesion layer a suitable mirror coating was achieved, resulting in a first mirror prototype (Döhring et al., 2017b). The telescope design and a mirror prototype are depicted in figure 2. The joint effort within the two projects resulted in more than ten papers and several conference contributions like talks and posters (see figure 3). Authorship of such publications is especially important for the involved young scientists in the early stages of their scientific careers.

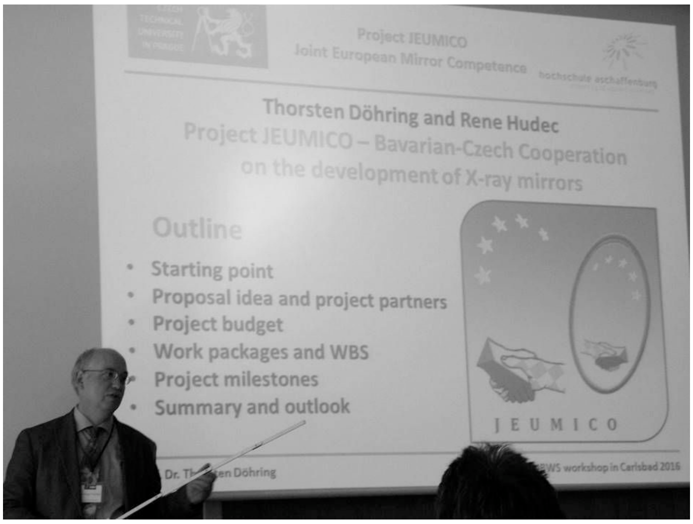
Project JEUMICO
Joint European Mirror Competence

Thorsten Döhring and Rene Hudec
Project JEUMICO – Bavarian-Czech Cooperation
on the development of X-ray mirrors

Outline

- Starting point
- Proposal idea and project partners
- Project budget
- Work packages and WBS
- Project milestones
- Summary and outlook

Dr. Th en Döhring
WS workshop in Carlsbad 2016

Figure 3. JEUMICO presentation at a scientific conference.

3. Internationalization of education and science

One main aim of the BTHA funding programs is to enhance the bi-national cross-border cooperation between Bavaria and the Czech Republic. Within the two granted projects an exchange of scientific staff between the involved partner organizations took place. In this context research stays at Aschaffenburg University of four young Czech Ph.D. students have been organized in the framework of the bilateral projects (Hudec & Döhring, 2017). A visual impression of such visit is given in figure 4. Note that during their studies Czech PhD students have to stay one semester abroad to get international research experience. The financing of such mandatory research stays is often difficult for them, but within the bilateral BTHA projects the possibility to give grants for research stays helped a lot. In the other direction several German students participated at the POSTER conference in Prague, a conference especially dedicated to give young scientists first experience at international scientific conferences. On an institutional level Aschaffenburg University of Applied Sciences and the Czech Technical University in Prague officially signed an ERASMUS+ contract in 2016 to fund the cross-border exchange of students (Hudec & Döhring, 2017). Following the university goal of internationalization the bilateral cooperation got valuable support from the university management. On top management level a delegation of Czech university presidents visited Bavaria in October 2017, and a delegation of Bavarian university presidents visited Czech universities the same months. One can state that the collaboration in education and science between the two neighbored regions in Europe is on a promising way into the future.

Figure 4. Research stay of Czech PhD students in Bavaria.

4. Aspects of project management

Both projects had to be managed with relatively small financial budgets. The granted funding was mainly dedicated to costs for traveling and accommodation of the involved team members. Thereby the regulations followed the principle of reciprocity: The Bavarian budget could be used for visit of Czech scientists in Bavaria and the Czech budget for visit of Bavarian scientists in the Czech Republic. However, also some hardware procurement was possible and a small salary for a PhD student could be paid to compensate his additional coordination effort. In general German Universities of Applied Sciences faces a lack of research funding and they usually have no permanent research staff. Nevertheless more and more research activities are done at German Universities of Applied Sciences. At Aschaffenburg University the granted bi-national funding allowed an interesting combination of research activities and internationalization. On the Czech side the granted funding co-sponsored IBWS workshops and AXRO conferences, both organized by the Czech partners. This gave more organizational flexibility and resulted in successful events. However, additional resources from other funding sources were needed on both sides to execute the joint projects successfully. The project management was also challenged by intercultural differences and there are some lessons learned. For Germans project planning is more important - which has pros and cons - whereas Czech people are more flexible here. There seem to be more bureaucracy in the Czech Republic for the submission of proposals than in Germany. Technically a joint field of work is needed for such cooperation, resulting in a common scientific goal. Thereby the complementary qualification respectively complementary technical equipment was beneficial for the project execution. The trilateral cooperation between Germany, the Czech Republic, and France was more difficult to organize. Direct meetings between French scientists and Czech scientists could not be financed by the granted bilateral budgets, which was a disadvantage in the intended three-party collaboration.

5. Public Relation Management

Publicity is another dimension of such cooperative projects. One should not underestimate the importance of public relation measures. They help for the visibility and the acceptance of the presented project inside and outside the university. For stakeholders like funding agencies, university management, and ministries this is often the most important output of a project. Here press releases on the two bilateral projects have been placed at the home-pages of both institutions. An example is shown in figure 5. In addition the joint projects have been presented with posters and talks at scientific conferences which is a scientific output as well as a valuable project marketing event in parallel. Furthermore the project team was present at public events of the funding agency

BTHA and even some public articles have been initiated in local newspapers and in Internet news.

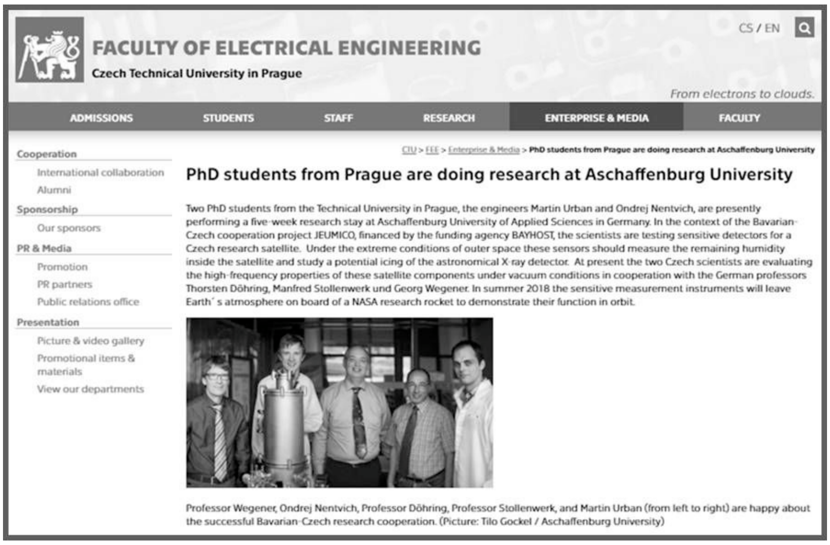

PhD students from Prague are doing research at Aschaffenburg University

Two PhD students from the Technical University in Prague, the engineers Martin Urban and Ondrej Nentvich, are presently performing a five-week research stay at Aschaffenburg University of Applied Sciences in Germany. In the context of the Bavarian-Czech cooperation project JEUMICO, financed by the funding agency BAYHOST, the scientists are testing sensitive detectors for a Czech research satellite. Under the extreme conditions of outer space these sensors should measure the remaining humidity inside the satellite and study a potential icing of the astronomical X-ray detector. At present the two Czech scientists are evaluating the high-frequency properties of these satellite components under vacuum conditions in cooperation with the German professors Thorsten Döhring, Manfred Stollenwerk und Georg Wegener. In summer 2018 the sensitive measurement instruments will leave Earth´ s atmosphere on board of a NASA research rocket to demonstrate their function in orbit.

Professor Wegener, Ondrej Nentvich, Professor Döhring, Professor Stollenwerk, and Martin Urban (from left to right) are happy about the successful Bavarian-Czech research cooperation. (Picture: Tilo Gockel / Aschaffenburg University)

Figure 5. JEUMICO press release on the CVUT homepage.

6. Summary and outlook

In December 2017 the two bi-national projects JEUMICO and TRILAMICO will run out. The multiple dimensions of this successful Bavarian-Czech collaboration between Aschaffenburg University and the Czech Technical University in Prague have been discussed. Scientific cooperation and exchange in an international context - here between Bavaria and the Czech Republic - and also corresponding private contacts are important contributions for political stability and for joint economic development in both countries. Thereby one should not underestimate the positive effect of informal communication while socializing in the evening (see figure 6).

The two projects also paved the way for future cooperation. A proposal on another joint project (AMAFUSMI Advanced materials for future space missions) have already been submitted to the funding agency BTHA. However, this call got a large interest from many other joint Czech-Bavarian proposal teams and the chances for funding are therefore quite small. Other options for joint proposals, especially for European funding programs like Horizon2020 are under consideration between the project partners. There is the strong intention on both sides to continue the established partnership also in the future.

Figure 6. Social dinner of the joint bi-national project team.

Acknowledgements. The JEUMICO project was gratefully funded by a Joint Call of the Bavarian State Ministry for Education and Culture, Sciences and Art and the Ministry of Education, Youth and Sports of the Czech Republic.The TRILAMICO project was financed by a grant from the Bavarian-Czech Academic Agency BTHA.

References

Döhring, T., Probst, A.-C., Emmerich, F., et al., Development of iridium coated x-ray mirrors for astronomical applications. 2017a, in Society of Photo-Optical Instrumentation Engineers (SPIE) Conference Series, Vol. **10399**, *Society of Photo-Optical Instrumentation Engineers (SPIE) Conference Series*, 103991C

Döhring, T., Probst, A.-C., Stollenwerk, M., et al., Prototyping iridium coated mirrors for x-ray astronomy. 2017b, in Society of Photo-Optical Instrumentation Engineers (SPIE) Conference Series, Vol. **10235**, *Society of Photo-Optical Instrumentation Engineers (SPIE) Conference Series*, 1023504

Hudec, R. & Döhring, T., JEUMICO: Czech-Bavarian astronomical X-ray optics project. 2017, *Contributions of the Astronomical Observatory Skalnate Pleso*, **47**, 170

Stehlíková, V., Proserpio, L., Friedrich, P., et al., Indirect glass slumping of grazing incidence mirror segments for lightweight x-ray telescopes. 2017, in Society of Photo-Optical Instrumentation Engineers (SPIE) Conference Series, Vol. **10399**, *Society of Photo-Optical Instrumentation Engineers (SPIE) Conference Series*, 103990Z

Stehlikova, V., Urban, M., Nentvich, O., et al., Study of lobster eye optics with iridium coated x-ray mirrors for a rocket experiment. 2017, in Society of Photo-Optical Instrumentation Engineers (SPIE) Conference Series, Vol. **10235**, *Society of Photo-Optical Instrumentation Engineers (SPIE) Conference Series*, 1023505

Contrib. Astron. Obs. Skalnaté Pleso **48**, 437 – 445, (2018)

Kirkpatrick Baez X–ray optics for astrophysics: Recent status

R. Hudec[1,2], **L. Pina**[3], **V. Marsikova**[1], **O. Nentvich**[1], **M. Urban**[1] and **A. Inneman**[1]

[1] *Czech Technical University in Prague, Faculty of Electrical Engineering*
Technicka 2, Prague 166 27, Czech Republic
(E-mail: hudecren@fel.cvut.cz)

[2] *Engelhardt Astronomical observatory, Kazan Federal University,*
Kremlyovskaya street 18, 420008 Kazan, Russian Federation

[3] *Czech Technical University in Prague, Faculty of Nuclear Sciences and*
Physical Engineering, Brehova 7, Prague 115 19, Czech Republic

Received: December 22, 2017; Accepted: March 5, 2018

Abstract. X-ray optics in Kirkpatrick Baez arrangement represent promising alternative to Wolter optics in common use. We present briefly recent status of design, developments, and tests of this kind of X–ray optics including Kirkpatrick Baez module developed and tested within the EU AHEAD project.

Key words: X–ray optics – X-ray telescopes – X–ray astrophysics

1. Introduction

X-ray optics in Kirkpatrick Baez (KB) arrangement illustrated in Fig. 1 represent promising alternative to Wolter optics in common use (Hudec, 2011). We present a review of the recent status of design, simulations, development, assembly and tests of X–ray optics including the KB module developed and tested within the EU AHEAD project. Various KB test modules were simulated, designed, assembled and tested at several X–ray test facilities. Selected results are briefly presented and discussed below.

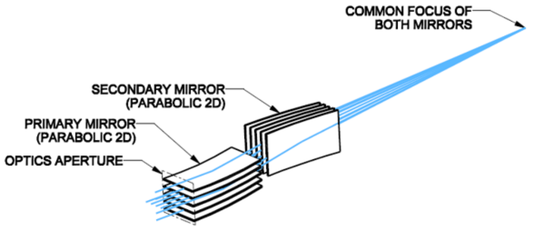

Figure 1. The principle of KB X–ray multifoil optical system.

2. Alternative Design for Astronomical X-ray Telescopes: Kirkpatrick-Baez X-Ray Optics.

The KB X–ray optics was the first X-ray imaging system proposed (Kirkpatrick & Baez, 1948). Kirkpatrick-Baez were not only proposing the geometry but they built and demonstrated a microscope using two crossed spheres. The KB X–ray optics is frequently used in laboratory and synchrotron as imaging system with high angular resolution. In space, it was used only on rockets at the early stages of X–ray astronomy (Gorenstein et al., 1971a,b,c) so far. Various modifications of the KB design exist (parabolic vs. elliptical, various number of reflections, 2 to 4).

Kirkpatrick-Baez is a double reflection X-ray optics and hence consists of two mirror sets one is aligned vertically and the second is aligned horizontally (Fig. 1). The quality of the focal spot image depends on the quality of substrates (shape, micro-roughness, etc.). Thin float glass foils and/or silicon wafers were used in the KB modules developed and tested. These substrates were mostly of standard quality, hence additional improvements can be expected if superior quality substrates will be used.

In the KB system, both mirrors are curved parabolically – the first mirror focuses in vertical plane and the second mirror focuses in horizontal plane in left picture of Fig. 2. Single focal point is formed in the crossection of the two focal planes as is shown in right picture of Fig. 2. Nested systems in order to increase the collection area are possible.

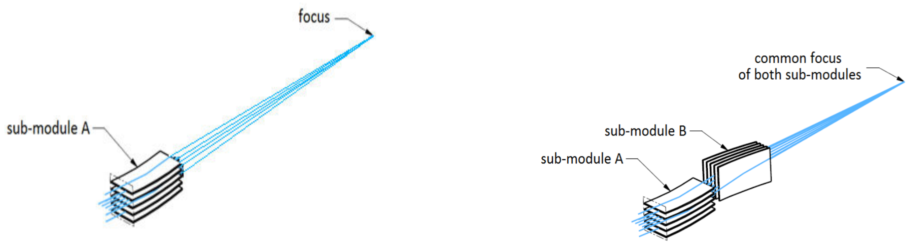

Figure 2. 1D (left) and 2D (right) X-ray optics of Kirk-Patrick Baez type both sub-modules (A and B) have common focus .

The technology of manufacture of KB modules is not necessarily based on precise and expensive mandrels (the KB reflecting substrates are almost flat plates, with curvatures of order of km), hence cost–effective manufacture (recent requirements of space agencies) of a high angular resolution (~ 5 arcsec) X–ray optics is feasible at affordable cost (Pina et al., 2011).

Historically, KB telescope applications were based on thin sheets of float glass because the quality of substrates for silicon wafers was inadequate for X–ray optics. The recent availability of substrates with considerably improved parameters and flatness now makes silicon wafers a more promising choice, especially for segmented telescopes (Hudec et al., 2006, 2008a,b; Willingale & Spaan, 2009). Novel methods also exist for further improving the quality of thin float glass (e.g., by thermally shaping the sheets on flat mandrels). Next–generation materials and substrates for glass foils and silicon wafers must also be thin and light (Hudec et al., 2009). Shaping them to small radii, as called for in Wolter designs, is not an easy task. KB arrangements consequently represent a less-laborious and hence less-expensive alternative.

3. Simulations

For every KB test module developed and assembled, ray–tracing simulations were performed in order to simulate the ideal imaging performance. Few selected results are given in Tab. 1 and in Fig. 3 and 4.

Table 1. Maximum intensity and FWHM dependence on used X–ray source

Energy (eV)	Maximum Intensity (counts)	FWHM (arcsec)
100 % reflection	5 329	3.8
280 (C)	4 893	3.7
1 500 (Al)	4 865	3.7
4 500 (Ti)	4 235	3.7
8 000 (Cu)	4 432	3.7
11 200 (Se)	4 394	3.7
17 500 (Mo)	2 036	3.4
25 300	1 075	3.1
30 000	575	2.9

4. X–ray tests at Boulder and Pennstate

Several KB modules were prepared for X–ray tests at the US test facilities. Typical KB module consisted of 144 commercially available 525 μm thick Si wafers with Au surface coating. For focus to focus tests, the mirrors arranged into planar-ellipsoidal shape with axial symmetry, with the 1st mirror at a distance of approx. 16 mm from optical axis. Typical mirror size was 100 × 100 mm with 3 sets of 24 (18+6) reflecting substrates in each module. Spacing between substrates was 1.5 to 2.5 mm with wedge smaller than 10 microns.

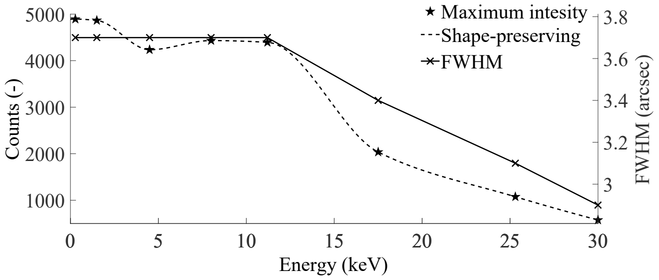

Figure 3. KB modules – ray tracing simulations, dependence on energy. Input parameters (mirror material properties, arrangement of mirrors in modules, experiment geometry, etc.) are the same as in the experiment. Point source was considered.

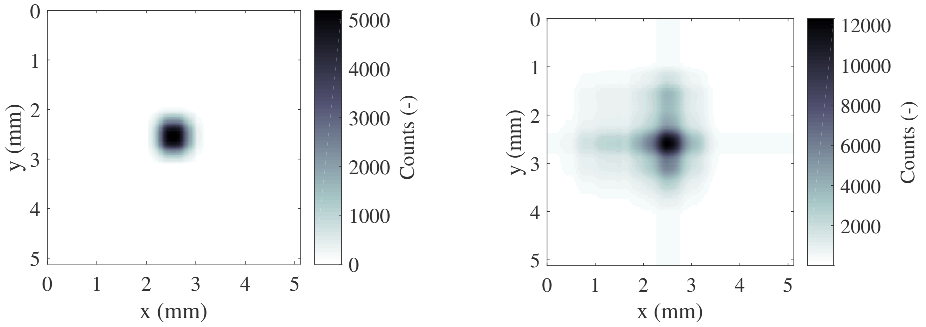

Figure 4. KB modules – ray tracing simulations. Input parameters (mirror material properties, arrangement of mirrors in modules, experiment geometry, etc.) are the same as in the experiment, for energy 453 eV (Ti L alpha). Left: Theoretical focus: FWHM = 0.58 mm 3.7 arcsec, right: Theoretical focus with 0.2 mm source diameter and 2 microns manufacturing errors: FWHM = 0.59 mm.

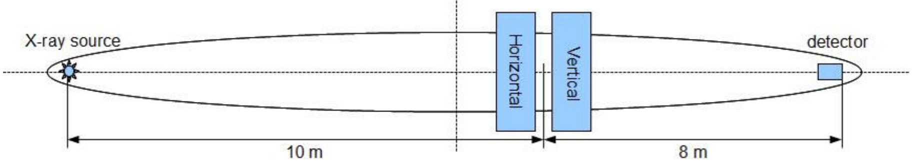

Figure 5. Experimental setup of the Boulder X–ray test experiment.

Modules were designed for vacuum chamber tests at CASA University of Colorado at Boulder, with small modifications for Pennsate tests.

KB modules were tested in vacuum chamber at CASA UC (Fig. 5), taking into account the experimental arrangement of the test facility (focus to focus) the KB test modules were of elliptical geometry, with source to optics distance: 10 m, optics to detector distance: 8 m, module position adjustment in visible light (Xe lamp), and a MCP detector as X–ray focal plane detector, with diameter of 1 inch (Figs. 6, 7). The examples of KB modules tested are in Fig. 8. For Pennstate tests, Timepix detector (Jakubek et al., 2014) was used to record the images (Fig. 9).

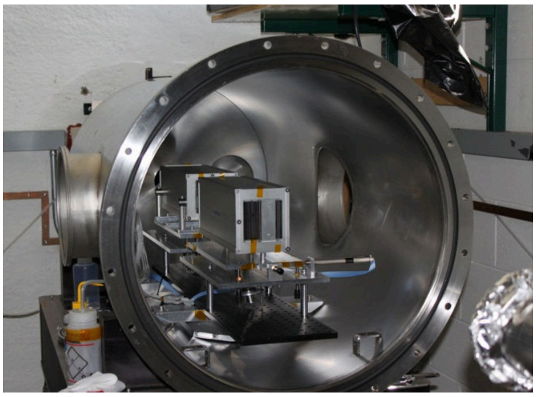

Figure 6. KB test modules – Boulder tests experimental arrangement.

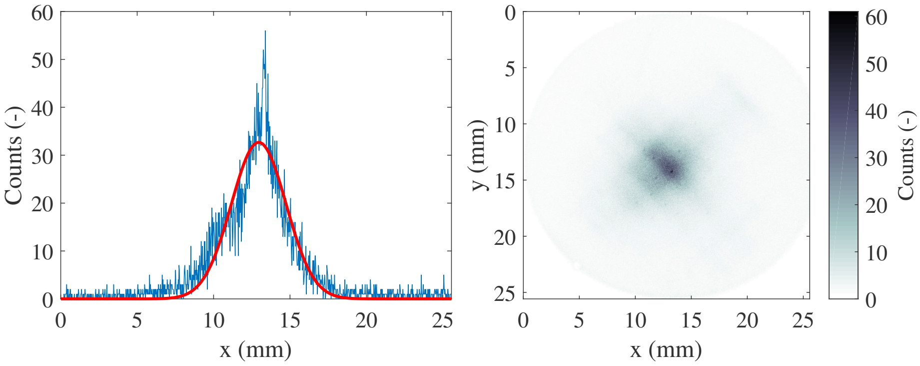

Figure 7. KB modules Boulder X-ray test results. MCP detector, diameter 1” Energy of X-rays: 453 eV, FWHM = 2.75 mm, Angular resolution: 10.2 arcsec (after ellips. correction).

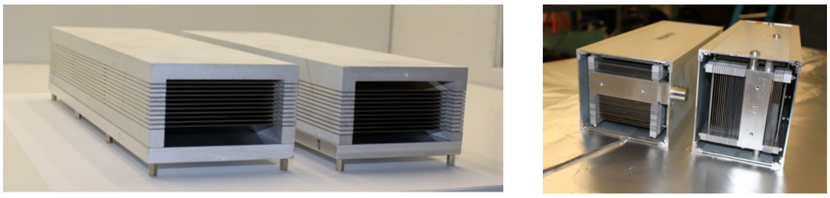

Figure 8. KB modules tested at Boulder (left) and Pennstate (right) X-ray test facilities.

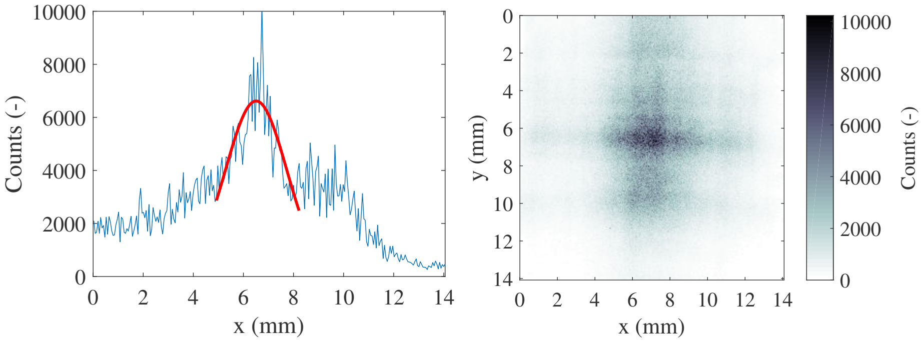

Figure 9. KB modules – Pennstate X–ray test results. Timepix detector (IEAP CTU in Prague), size 14 mm, 500 nm Al filter, Energy of X-rays: 4.5 keV, FWHM = 2.97 mm, Angular resolution FWHM: 8.7 arcsec (after ellips. correction).

5. X–ray tests at PANTER

The full illumination X–ray tests of the first KB module (see Fig. 10 and Tab. 2) designed and assembled within the AHEAD project (Piro et al., 2015) were performed at the Max Planck Institute for extraterrestrial Physics at PANTER facility in Neuried, Germany in 2017, with preliminary results shown in Fig. 11. More details on these tests (including other types of X–ray optics) are given in another paper in this volume (Pina et al., 2018).

Table 2. Parameters of KB X-ray optics module for PANTER X ray tests. These parameters are for one 1D KB sub-module. Full 2D KB system is represented by 2 analogous modules.

Properties	Value
Number of foils in one sub–module	17
Dimension of foils	$50 \times 100 \times 0.625\,\mathrm{mm}^3$
Spacing	4.5 mm
Reflective surface	Au
Dimension of sub–module	$105 \times 105 \times 50\,\mathrm{mm}^3$
Aperture	$80 \times 80\,\mathrm{mm}^2$
Focus z_α/z_β	6 500 mm
Source distance	123 m
Detector resolution	256×256 pixels
Pixel size	75 μm

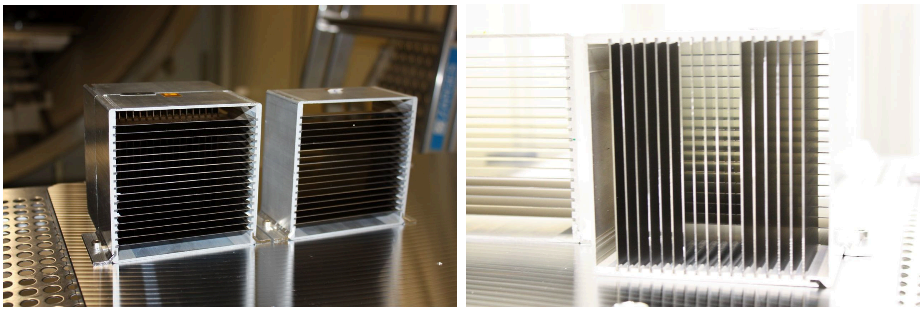

Figure 10. AHEAD KB X–ray optics

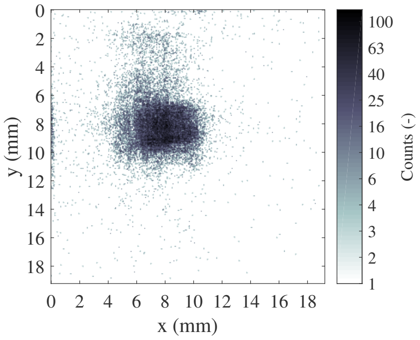

Figure 11. AHEAD KB 2D X–ray optics – the best 2D focus at 1.49 keV (33 arcsec FWHM).

6. Conclusions

Various Kirkpatrick Baez X–ray optics modules were assembled and tested, based either on glass foils or high–quality silicon wafers, all of them in multi–foil arrangement, i.e. as stacked modules with typically 72 nested parabolic or elliptic X–ray reflecting substrates 10 × 10 cm each. These modules were tested at several X–ray test facilities, with very promising results, with around 10 arcsec FWHM for the full stack.

The KB X–ray optics represent promising alternative to widely used Wolter mirrors, mainly because of less expensive manufacture (no need for expensive mandrels, use of commercially available parts such as silicon wafers etc.).

In summary, the availability of high-quality novel materials such as superior silicon wafers and/or glass foils will enable the design and construction of KB X-ray optical systems with very high angular resolution at reasonable cost for various applications both in space, astronomy, as well as in the laboratory. In the near future, we plan to continue the development of advanced astronomical KB X–ray test optics with assembling and testing both in visible light and in X–rays, stacked KB modules with longer focal length and improved performance, based on superior quality substrates, e.g. Si wafers with further improved flatness and surface quality.

Acknowledgements.

We acknowledge GA CR grant 13-33324S and AHEAD EU Horizon 2020 project (Integrated Activities in the High Energy Astrophysics Domain), grant agreement n. 654215. We thanks the teams at the X–ray test facilities at Boulder, Pennstate, and MPE PANTER for their assistance and help with or measurements there. This work was partly supported by the Grant Agency of the Czech Technical University in Prague, grant No. SGS18/186/OHK3/3T/13 and MEYS RVO 68407700 as well.

References

Gorenstein, P., Harris, B., Gursky, H., & Giacconi, R., A Rocket Payload Using Focusing X-Ray Optics for the Observation of Soft Cosmic X-Rays. 1971a, in IAU Symposium, Vol. **41**, *New techniques in Space Astronomy*, ed. F. Labuhn & R. Lust, 183

Gorenstein, P., Harris, B., Gursky, H., & Giacconi, R., A rocket payload using focusing X-ray optics for the observations of soft cosmic X-rays. 1971b, *Nuclear Instruments and Methods*, **91**, 451, DOI: 10.1016/S0029-554X(71)80022-8

Gorenstein, P., Harris, B., Gursky, H., et al., X-ray Structure of the Cygnus Loop. 1971c, *Science*, **172**, 369, DOI: 10.1126/science.172.3981.369

Hudec, R., Kirkpatrick-Baez x-ray optics: a review. 2011, in Proc. SPIE, Vol. **8076**, *EUV and X-Ray Optics: Synergy between Laboratory and Space II*, 807607

Hudec, R., Marsikova, V., Mika, M., et al., Advanced x-ray optics with Si wafers and slumped glass. 2009, in Proc. SPIE, Vol. **7437**, *Optics for EUV, X-Ray, and Gamma-Ray Astronomy IV*, 74370S

Hudec, R., Pina, L., Sveda, L., et al., Novel Approaches in Technologies for Large Light-Weight X-ray Space Telescopes. 2006, in ESA Special Publication, Vol. **604**, *The X-ray Universe 2005*, ed. A. Wilson, 969

Hudec, R., Semencová, V., Inneman, A., et al., Novel Technologies for Astronomical X-ray Telescopes. 2008a, in *The X-ray Universe 2008*, 254

Hudec, R., Sik, J., Lorenc, M., et al., Recent progress with x-ray optics based on Si wafers and glass foils. 2008b, in Proc. SPIE, Vol. **7011**, *Space Telescopes and Instrumentation 2008: Ultraviolet to Gamma Ray*, 701116

Jakubek, J., Jakubek, M., Platkevic, M., et al., Large area pixel detector WIDEPIX with full area sensitivity composed of 100 Timepix assemblies with edgeless sensors. 2014, *Journal of Instrumentation*, **9**, C04018, DOI: 10.1088/1748-0221/9/04/C04018

Kirkpatrick, P. & Baez, A. V., Formation of optical images by x-rays. 1948, *Journal of the Optical Society of America (1917-1983)*, **38**, 766

Pina, L., Hudec, R., Inneman, A., et al., Multi Foil X-ray Optics Tests at PANTER: Preliminary Results. 2018, *Contributions of the Astronomical Observatory Skalnaté Pleso*

Pina, L., Marsikova, V., Hudec, R., et al., Full-aperture x-ray tests of Kirkpatrick-Baez modules: preliminary results. 2011, in Proc. SPIE, Vol. **8076**, *EUV and X-Ray Optics: Synergy between Laboratory and Space II*, 807609

Piro, L., Natalucci, L., & Ahead Consortium, AHEAD: Integrated Activities in the High Energy Astrophysics Domain. 2015, in *Exploring the Hot and Energetic Universe: The first scientific conference dedicated to the Athena X-ray observatory*, ed. M. Ehle, 74

Willingale, R. & Spaan, F. H., The design, manufacture and predicted performance of Kirkpatrick-Baez Silicon stacks for the International X-ray Observatory or similar applications. 2009, in Proc. SPIE, Vol. **7437**, *Optics for EUV, X-Ray, and Gamma-Ray Astronomy IV*, 74370B

Contrib. Astron. Obs. Skalnaté Pleso **48**, 446 – 455, (2018)

Light rays and wave fronts in strong gravity

V. Karas[1], **Y. Kojima**[2] **and D. Kunneriath**[3]

[1] *Astronomical Institute of the Czech Academy of Sciences,*
Boční II 1401, CZ-14100 Prague, Czech Republic
(E-mail: vladimir.karas@cuni.cz)

[2] *Department of Physics, Hiroshima University, Higashi-Hiroshima,*
Hiroshima 739-8526, Japan

[3] *National Radio Astronomy Observatory, 520 Edgemont Road,*
Charlottesville 22903 (VA), USA

Received: December 18, 2017; Accepted: January 23, 2018

Abstract. Accretion onto black holes often proceeds via an accretion disk or a temporary disk-like pattern. Variability features observed in light curves as well as theoretical models of accretion flows suggest that accretion disks tend to be inhomogeneous – variety of substructures (clumps) emerge within the flow. Rapid orbital motion of individual clumps then modulates the observed signal in X-rays. Furthermore, changes of spectral lines and polarization properties of the observed signal (or the absence of changes) constrain the models and reveal information about general relativity (GR) effects. In this write-up we summarize the basic equations that have been employed to study light propagation near black holes and to derive the radiation signal that can be expected at a detector within the framework of geometrical optics approximation.

Key words: Black holes – Accretion, accretion disks – General relativity

1. Introduction

Accreting black holes are thought to be the most likely agents driving active galactic nuclei and compact binaries. Nonetheless, various aspects of the picture still need to be understood and several viable alternatives have been proposed (see, e.g., an overview in Eckart et al., 2017). Numerical and semi-analytical computations of emission continua and emission-line profiles are important tools for verification of models with black-hole accretion disks (Gerbal & Pelat, 1981; Fabian et al., 1989; Kojima, 1991; Laor, 1991; Karas et al., 1992). Here we briefly outline the underlying ideas, believing that the disk radiation must be affected by the orbital motion of its elements. An intrinsically narrow spectral line with a single, well-defined peak in the local rest frame co-moving with the disk material becomes broader or it can be split into more components in the frame of a distant observer. This has to be modelled in a manner consistent with the underlying continuum, taking into account the interplay of parameters describing the system (Fabian et al., 2000).

We adopt the standard black-hole accretion disk scenario (Frank et al., 1992), where the radiation signal emerges from the surface of the disk along the range of radius, $R_{\rm in} < R < R_{\rm out}$. Because of the temperature profile, the main contribution to the bulk emissivity of low ionization lines originates in the distant region of $\approx 10^4 R_{\rm g}$, i.e. near $R_{\rm out}$.[1] In addition, there is Doppler-boosted radiation coming from $R \approx R_{\rm in}$. As a result, two peaks appear in the line profile. Assuming Keplerian rotation, the orbital velocity corresponding to these peaks satisfies the relation

$$\frac{v_{{\rm K}|R=R_{\rm in}}}{v_{{\rm K}|R=R_{\rm out}}} \simeq \sqrt{\frac{R_{\rm out}}{R_{\rm in}}}, \tag{1}$$

which is independent of the disk inclination angle. This ratio gives us the first estimate of the disk size (GR effects will modify this to certain extent). Typically, for $M \approx M_\odot$ one obtains $R_{\rm out} \approx (10^4\text{–}10^5) R_{\rm g}$. The observer view angle has to be determined independently.

A direct consequence of predominantly azimuthal motion of the radiating matter is the onset of a double-peaked line core, as in a self-absorbed line. Near the inner rim of the accretion flow the velocity of the bulk motion grows and it becomes comparable with the speed of light. Naturally, fast motion leads to the spectral-line broadening. However, double-peaked profiles are only rarely observed (Chen & Halpern, 1989; Eracleous & Halpern, 1994): the lines are usually filled in. This is also the evidence for large $R_{\rm out}$. On the other hand, general-relativistic light-bending and the significant frequency shifts arise at small radii, in the immediate neighbourhood of the black-hole horizon, and they also contribute to the line asymmetry and broadening (Kojima, 1991; Laor, 1991; Kojima & Fukue, 1992; Karas et al., 1995).

The Doppler effect transforms photons of radiation emitted at wavelength $\lambda_{\rm em}$ to the observed wavelength

$$\lambda_{\rm obs} = \lambda_{\rm em}\,\frac{(1-\beta y)}{\sqrt{1-\beta^2}} \approx \lambda_{\rm em}\left(1 + \frac{1}{2}\beta^2 - \beta y\right), \tag{2}$$

where $\beta = v/c$, $y = \sin\phi \sin\theta_{\rm obs}$ (ϕ is the azimuthal coordinate in the disk plane and $\theta_{\rm obs}$ is the inclination of the observer). Analogously, the gravitational redshift is

$$\lambda_{\rm obs} = \frac{\lambda_{\rm em}}{1-\beta^2}. \tag{3}$$

The position of the centroid of the line is independent of the disk inclination. Naturally, one cannot separate Doppler and gravitational shifts in a complete, self-consistent relativistic treatment of the problem. The centroid wavelength depends on inclination, when the wavelength shift, anisotropic emissivity of the

---

[1] The Schwarzschild radius $R_{\rm g}$ is defined in terms of the black hole mass $M_\bullet$: $R_{\rm g} \equiv 2GM_\bullet/c^2 \sim 3\times10^{13}\,M_8\,$cm, where $M_8 = M_\bullet/10^8 M_\odot$ and $M_\odot$ denotes the mass of the Sun. $R_{\rm g}$ defines the linear size of a non-rotating black hole, whereas a maximally rotating (Kerr) black hole has the size half $R_{\rm g}$.

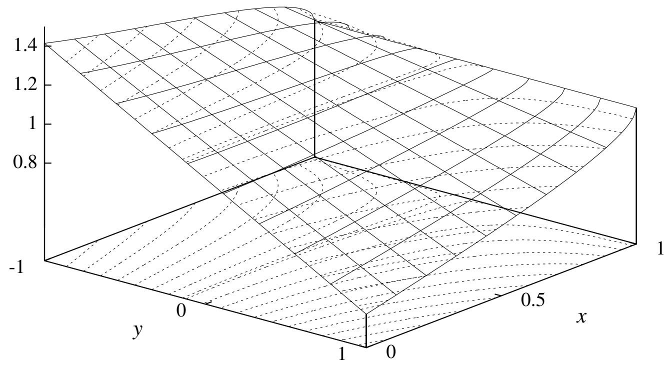

Figure 1. Redshift function $g(x, y)$ in dependence on two dimensionless spatial coordinates within the disk plane, $y = \sin\phi \sin\theta_{\mathrm{obs}}$ and $x = 1 - 3R_{\mathrm{g}}/R$. Different components of the overall energy shift add up to produce energy decrease ($g > 1$) or enhancement ($g < 1$) in different regions of the disk. This definition of (x, y) allows us to capture the entire disk plane from circular photon orbit at $r = 3R_{\mathrm{g}}$ up to infinity, $r \to \infty$ (Murphy et al., 2009).

material depending on the emission angle, and gravitational focusation of light rays are properly taken into account.

2. Calculating the observed spectral line profiles

The radiation originating from the gaseous elements at the inner edge of the disk experiences stronger gravitational and transverse Doppler redshift than the radiation from regions located further out. This results in a redward asymmetry of the skewed line. In addition, the Doppler-boosted radiation from the approaching material contributes to an enhanced peak of the blue wing of the line. Elements of the ring emit radiation with frequency $\nu = \nu_{\mathrm{em}}$ that represents the Dirac δ-function in the local rest frame. The line profile results from a superposition of individual contributions affected by a competition of the overall Doppler effect and the gravitational redshift. This observed profile depends on the inclination θ_{obs}. For the case of a disk, the line profile can be obtained by splitting the disk into a number of concentric rings, each emitting with its own local frequency and intensity, and summing their total radiation together.

Graphs of the relative frequency shift (the redshift factor)

$$1 + z \equiv g \equiv \frac{\lambda_{\mathrm{obs}}}{\lambda_{\mathrm{em}}} \tag{4}$$

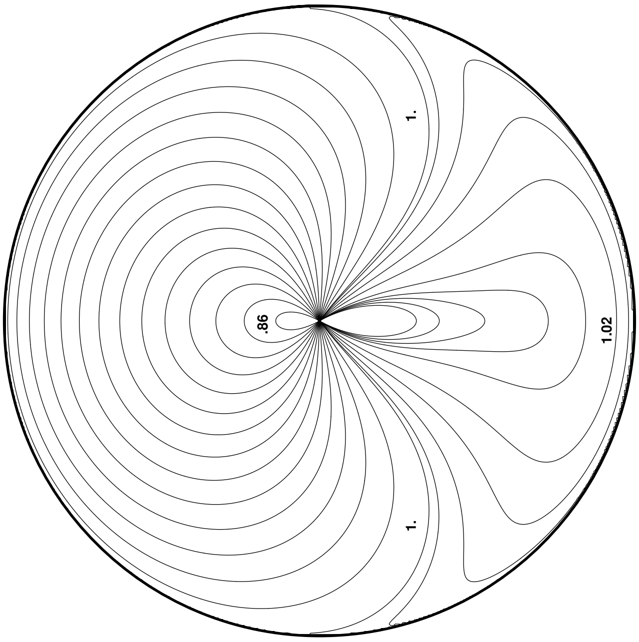

Figure 2. Isocontours of g in the disk surface – a projection along the disk axis. Radial coordinate of the circle (x) is defined as in the previous figure, the azimuthal coordinate is ϕ here. A distant observer is located on the right side of the disk with a fixed value of view angle inclination, $\theta_{\rm obs} = 15\,{\rm deg}$. Values of $g > 1$ and $g < 1$ correspond to redshifted and blueshifted radiation, respectively.

along the Keplerian disk surface are shown in figures 1–2, taking into account general relativistic effects on the radiation. The formula (4) can be rewritten in a simpler form within the pseudo-Newtonian approximation,

$$g = \sqrt{\frac{R - 2R_{\rm g}}{(R - 3R_{\rm g})\,R}}\left(\sqrt{R - 2R_{\rm g}} - y\right). \tag{5}$$

The formula (5) is valid for a non-rotating black hole, however, a more complicated expression can be derived also in the rotating (Kerr) case, where it depends on the black-hole spin (and thus it enables to constrain the black hole rotation by fitting the observed spectra). An algorithm for the calculation of the predicted effects in spectral line profiles has been implemented in variety of modifications and under various assumptions (see Karas, 2006, and references cited therein). It can be outlined in a few steps as follows. Let us remind the reader that we assume the approximation of geometrical optics ($\lambda \ll R_{\rm g}$).

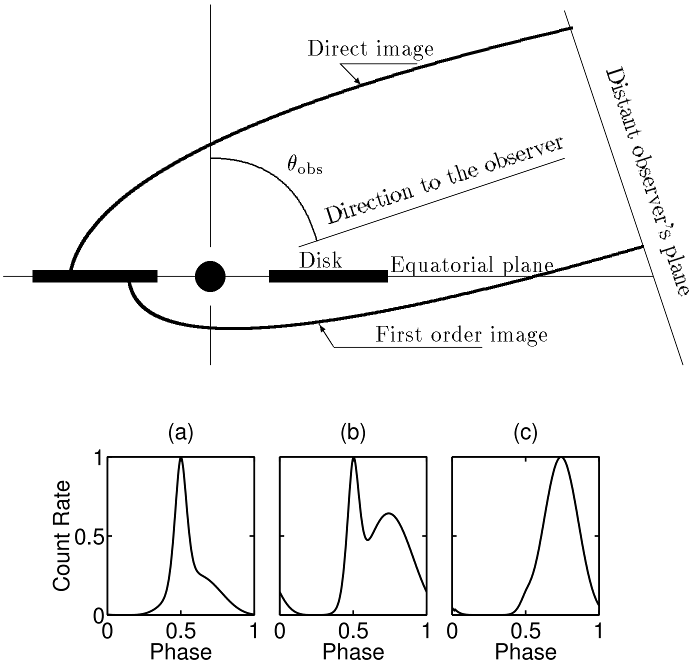

Figure 3. Top: a schematic illustration of the arrangement for a simulated image of the black-hole accretion disk, shown here in the poloidal cross-section. Bottom: Typical light-curves from a spot orbiting over one complete revolution on the surface of an accretion disk. Parameters: (a) $r = 3R_{\rm g}$, $\theta_{\rm obs} = 80$ deg (lensing peak dominates the lightcurve near the orbital phase 0.5); (b) $r = 44R_{\rm g}$, $\theta_{\rm obs} = 80$ deg; (c) $r = 44R_{\rm g}$, $\theta_{\rm obs} = 20$ deg (Doppler peak dominates near the phase 0.75). For further details, see Karas & Kraus (1996); Dovčiak et al. (2004); Karas (2006).

Firstly, we calculate (or define) the disk surface, $z \equiv z(R)$, and determine the intensity of radiation $I^{\rm R}(R)$ which is emitted from the surface as a function of radius, frequency of radiation and direction with respect to the disk surface in the frame co-rotating with the disk material. As we saw earlier, in the simplified formulation of the standard model one assumes thermal radiation with an isotropic distribution in all directions arising from the equatorial plane, $z = 0$, but the problem becomes much more complex if it is to be solved self-consistently with the equation of radiative transfer. In vacuum, wave fronts of emerging radiation can be solved via the eikonal equation, which in the Schwarzschild metric reads (Hanni, 1977)

$$-\left(1-\frac{2M}{r}\right)(\psi_{,r})^2+\left(1-\frac{2M}{r}\right)^{-1}(\psi_{,t})^2-r^{-2}(\psi_{,\phi})^2=0. \qquad (6)$$

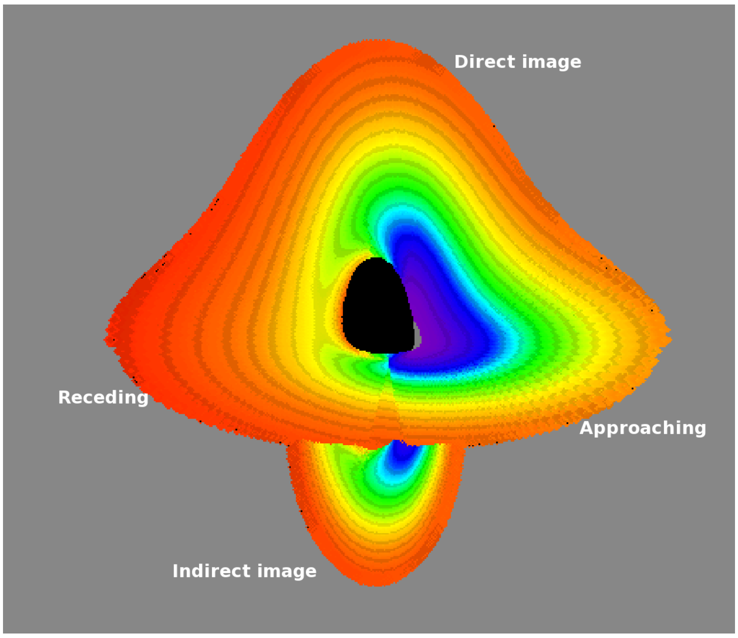

Figure 4. A synthetic image of a thin disk as projected onto the detector plane and viewed by a distant observer; the case of a rotating black hole in the center (colour coded by energy of photons at the detector plane; $a/M = 0.99$, $\theta_{\rm obs} = 85$ deg). The inner rim has been set at the innermost stable circular orbit (ISCO), while the outer radius is set at a somewhat arbitrary value. Part of the direct image from the region of the disk behind the central object with respect to the observer acquires a significant distortion and it appears to be elevated more above the equatorial plane. In addition, the observer can also see the first order (indirect) image, which has been formed by the rays crossing the equatorial plane once (in the bottom part of the picture). The contribution of the first and the higher order images to the total radiation flux depends on inclination of the distant observer, optical thickness of the disk, and a number of other parameters. The colour scale ranges from $g = 0.6$ (blue, the approaching side) to $g = 1.4$ (red, the receding part), corresponding to energy blueshift and redshift of the emerging photons, respectively; see fig. 5 for a different representation of the redshift function across the disk plane.

Eq. (6) can be solved by separation of variables, $\psi(t,r,\phi) \equiv R(r) + \alpha\phi - \omega t$. Photon propagation in the vacuum curved spacetime can be formally represented in terms of wave fronts $\psi = \text{const}$ distorted by the influence of material media in the flat spacetime. Also in Kerr metric the wave fronts can be defined and solved analytically, however, the structure of the eikonal equation is more complicated because of frame dragging.

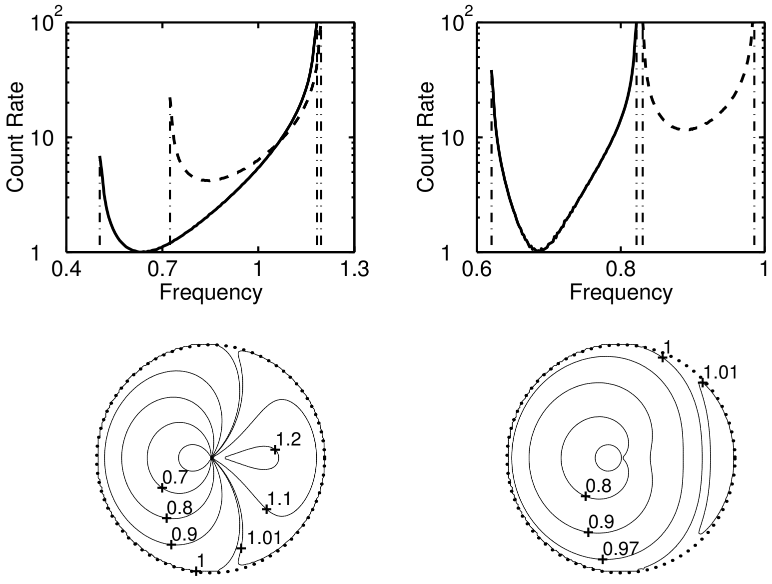

(a) (b)

Figure 5. The range and the distribution of the redshift function across the equatorial accretion disk. Lower panels: lines of equal value of frequency shift g on a disk in Keplerian rotation around a Schwarzschild black hole, constructed in a way similar to fig. 2: an observer looks from the bottom of the page ($\phi = 0$). and both plots are drawn with the radial coordinate $x \equiv 1 - 3\,R_{\rm g}/r$ ($0 \leq x \leq 1$). Values of g-factor are indicated in the figure. The whole equatorial plane outside the inner edge of the disk is thus captured in this illustration; dotted circles correspond to $x = 1$. Observer inclination is (a) 85 deg (almost edge-on view), and (b) 20 deg (almost pole-on view). Upper panels: The corresponding observed photon count rates, i.e., the incoming photon flux (in arbitrary units) from a point-like source orbiting in the disk plane at $r_{\rm em} = 3R_{\rm g}$ (solid line) and $r_{\rm em} = 8R_{\rm g}$ (dashed line), averaged over the entire revolution. Effectively, the shape represents an observed profile of an narrow emission ring of a given radius emitting intrinsically at a single frequency $\nu = \nu_{\rm em}$. This shows how the photon energy is influenced by strong gravity of the black hole at different location of the accretion disk. The count rate is in arbitrary units and the frequency is normalized to the unit emission frequency ($\nu_{\rm em} = 1$; see Karas & Kraus, 1996, for further details).

Let us note at this point that for definiteness of examples and illustration purposes we adopt the standard (relativistic) black-hole accretion disk scenario (Frank et al., 1992; Kato et al., 2008), where the locally emitted spectrum is described by multi-temperature thermal radiation (a superposition of black body spectra with the temperature changing as a function of radius). Also, we remind the reader that our discussion concerns only the gravitational effects on the light rays that propagate through empty (curved) space-time of the black hole. In the other words, the entire volume above the accretion disk is treated as optically thin. A more realistic description will require to take the scattering effects on the photon propagation into account in the disk corona.

Secondly, we have to specify location of a distant observer with respect to the disk axis. In the usual notation, inclination angle of $\theta_{\rm obs} = 90\,{\rm deg}$ means edge-on view while $\theta_{\rm obs} = 0\,{\rm deg}$ means pole-on view. Distant observer's plane (i.e., a "detector plane") is perpendicular to the direction $\theta = \theta_{\rm obs}$ at an infinite spatial distance from the source. One has to choose a convenient integration grid within the disk surface if the integration is to be carried out numerically.

Each grid point (image pixel) determines unambiguously a photon ray that crosses the plane of the observer perpendicularly (fig. 3). We calculate intersections of these rays with the disk surface $z \equiv z(R)$. Photon trajectories (null geodesics) will not be straight lines in space if effects of general theory of relativity are taken into account but this fact poses only a technical complication in calculating the intersections rather than a principal difference. Therefore, thirdly, we transform radiation intensity from the local disk frame, $I^{\rm R}(R, z(R); \nu^{\rm R}, \mu^{\rm R})$, to the observer's laboratory frame, $I^{\rm L}(R, z(R); \nu^{\rm L}, \mu^{\rm L})$, and propagate the intensity to the observer's plane. As mentioned above, a typical double-horn profile arises in the observed spectral line (although only one peak may be seen for some parameter values, namely, the inclination angle and the emission radius). Finally, we calculate the total observed flux of radiation by collecting photons,

$$F^{\rm L}(\nu^{\rm L})_{|\theta=\theta_{\rm obs}} = \int_{\text{(Over observer's plane)}} I^{\rm L}(\nu^{\rm L})_{|R\rightarrow\infty,\theta=\theta_{\rm obs}}\,dS. \tag{7}$$

The disk emits at temperature decreasing as a power-law function of radius. The resulting image is created and plotted, as shown in figure 4. Red colour (prevailing in the left part of the image) corresponds to a decreased energy of incoming photons with respect to energy in the local rest-frame attached to the disk, blue colour (prevailing in the right part of the image) corresponds to an increased energy. Light bending distorts the shape of the disk image, in particular when the observer's inclination is large (here it is almost edge-on, $\theta_{\rm obs} = 85\,{\rm deg}$). Notice that the image of the inner edge of the disk is not axially symmetric due to rotation of the black hole (dimensionless angular momentum parameter $a = 0.99$, i.e., almost maximal rotation). This figure is a typical result from computer modelling (Fukue & Yokoyama, 1988; Luminet, 1979; Karas et al., 1992; Viergutz, 1993). The main parameters influencing the final image are the functional dependency of the intrinsic emissivity over the disk surface, $I(r)$, the specific angular momentum a/M of the black hole, and the inclination $\theta_{\rm obs}$ of the accretion disk with respect to observer's line of sight.

3. Conclusions

We discussed effects of strong gravity on radiation that propagates from an accretion disk towards a distant observer. Imprints of these effects provide us with a possibility to study black holes residing the center of the disk. Having in mind the applications to present-day X-ray observations, the energy shifts, gravitational lensing and time delays are the principal effects which originate from General Relativity and can be tested. GR effects become dominant in the close vicinity of the hole, where they smear the resulting signal and are responsible for the source spectrum and its variability.

Let us note that the black-hole accretion disk model is defined by a number of parameters. There is a certain degree of degeneracy among the parameter values, so that some parameters cannot be constrained with sufficient confidence. This results in ambiguities that make the fitting procedure difficult. A partial way out is often adopted by freezing some of the parameters at their likely values, however, a more secure solution will require to gather addition observational data about the system.

Polarimetry can be employed to gain additional information. Unlike the case of equatorial (geometrically thin) disk, the possibility of non-negligible vertical thickness introduces an additional degree of freedom. Polarimetric properties are known to be very sensitive to the geometry of the source and we will need this extra piece of information to disentangle GR effects from cumbersome local physics. More complex non-axial geometry of the emitting region needs to be explored, such as spiral waves propagating across the accretion disk and twisted (precessing) disks. Strong gravity near the central black hole is very likely the main agent shaping the overall form of the X-ray spectral features from the inner disk.

Acknowledgements. VK acknowledges the Czech Science Foundation grant No. 17-16287S titled “Oscillations and Coherent Features in Accretion Disks around Compact Objects and Their Observational Signatures”.

References

Chen, K. & Halpern, J. P., Structure of line-emitting accretion disks in active galactic nuclei – ARP 102B. 1989, *Astrophys. J.*, **344**, 115, DOI: 10.1086/167782

Dovčiak, M., Karas, V., & Yaqoob, T., An Extended Scheme for Fitting X-Ray Data with Accretion Disk Spectra in the Strong Gravity Regime. 2004, *Astrophys. J., Suppl.*, **153**, 205, DOI: 10.1086/421115

Eckart, A., Hüttemann, A., Kiefer, C., et al., The Milky Way’s Supermassive Black Hole: How Good a Case Is It? 2017, *Foundations of Physics*, **47**, 553, DOI: 10.1007/s10701-017-0079-2

Eracleous, M. & Halpern, J. P., Doubled-peaked emission lines in active galactic nuclei. 1994, *Astrophys. J., Suppl.*, **90**, 1, DOI: 10.1086/191856

Fabian, A. C., Iwasawa, K., Reynolds, C. S., & Young, A. J., Broad Iron Lines in Active Galactic Nuclei. 2000, *Publ. Astron. Soc. Pac.*, **112**, 1145, DOI: 10.1086/316610

Fabian, A. C., Rees, M. J., Stella, L., & White, N. E., X-ray fluorescence from the inner disc in Cygnus X-1. 1989, *Mon. Not. R. Astron. Soc.*, **238**, 729, DOI: 10.1093/mnras/238.3.729

Frank, J., King, A., & Raine, D. 1992, *Accretion power in astrophysics.* (Camb. Astrophys. Ser., Vol. 21)

Fukue, J. & Yokoyama, T., Color photographs of an accretion disk around a black hole. 1988, *Publ. Astron. Soc. Jap.*, **40**, 15

Gerbal, D. & Pelat, D., Profile of a line emitted by an accretion disk - Influence of the geometry upon its shape parameters. 1981, *Astron. Astrophys.*, **95**, 18

Hanni, R. S., Wave fronts near a black hole. 1977, *Phys. Rev. D*, **16**, 933, DOI: 10.1103/PhysRevD.16.933

Karas, V., Theoretical aspects of relativistic spectral features. 2006, *Astronomische Nachrichten*, **327**, 961, DOI: 10.1002/asna.200610672

Karas, V. & Kraus, P., Doppler Tomography of Relativistic Accretion Disks. 1996, *Publ. Astron. Soc. Jap.*, **48**, 771, DOI: 10.1093/pasj/48.5.771

Karas, V., Lanza, A., & Vokrouhlický, D., Emission-line profiles from self-gravitating thin disks. 1995, *Astrophys. J.*, **440**, 108, DOI: 10.1086/175252

Karas, V., Vokrouhlický, D., & Polnarev, A. G., In the vicinity of a rotating black hole - A fast numerical code for computing observational effects. 1992, *Mon. Not. R. Astron. Soc.*, **259**, 569, DOI: 10.1093/mnras/259.3.569

Kato, S., Fukue, J., & Mineshige, S. 2008, *Black-Hole Accretion Disks — Towards a New Paradigm* (Kyoto University Press, Kyoto, Japan)

Kojima, Y., The effects of black hole rotation on line profiles from accretion discs. 1991, *Mon. Not. R. Astron. Soc.*, **250**, 629, DOI: 10.1093/mnras/250.3.629

Kojima, Y. & Fukue, J., Line profiles emitted from an accretion torus. 1992, *Mon. Not. R. Astron. Soc.*, **256**, 679, DOI: 10.1093/mnras/256.4.679

Laor, A., Line profiles from a disk around a rotating black hole. 1991, *Astrophys. J.*, **376**, 90, DOI: 10.1086/170257

Luminet, J.-P., Image of a spherical black hole with thin accretion disk. 1979, *Astron. Astrophys.*, **75**, 228

Murphy, K. D., Yaqoob, T., Karas, V., & Dovčiak, M., On the Prospect of Constraining Black Hole Spin Through X-ray Spectroscopy of Hotspots. 2009, *Astrophys. J.*, **701**, 635, DOI: 10.1088/0004-637X/701/1/635

Viergutz, S. U., Image generation in Kerr geometry. I. Analytical investigations on the stationary emitter-observer problem. 1993, *Astron. Astrophys.*, **272**, 355

Contrib. Astron. Obs. Skalnaté Pleso **48**, 456 – 465, (2018)

Lobster Eye X–ray optics for astrophysics: Recent status

R. Hudec[1,2], **L. Pina**[3], **V. Marsikova**[1], **O. Nentvich**[1], **M. Urban**[1] and **A. Inneman**[1]

[1] *Czech Technical University in Prague, Faculty of Electrical Engineering*
Technicka 2, Prague 166 27, Czech Republic
(E-mail: hudecren@fel.cvut.cz)

[2] *Engelhardt Astronomical observatory, Kazan Federal University,*
Kremlyovskaya street 18, 420008 Kazan, Russian Federation

[3] *Czech Technical University in Prague, Faculty of Nuclear Sciences and*
Physical Engineering, Brehova 7, Prague 115 19, Czech Republic

Received: December 16, 2017; Accepted: March 8, 2018

Abstract. X-ray optics in Lobster Eye arrangement represent promising complementary device to narrow field X–ray optics in common use. We present briefly recent status of design, developments, and tests of X–ray optics including Lobster Eye modules developed and tested within recent space project.

Key words: X–ray optics – X–ray telescopes – X–ray astrophysics

1. Introduction

X–ray optics in Lobster Eye (LE) arrangement represent promising complementary device to narrow field X–ray optics in common use. The wide field of view lobster telescope can e.g. detect and provide positions for fast, short lived transients such as gamma–ray bursts and X–rays accompanying gravitational waves, while the narrow field of view Wolter telescope provides high resolution images but can only point to known sources that have been discovered and positioned by other instruments such as the lobster telescope.

We present review of the recent status of design, simulations, development, assembly and tests of Lobster Eye X–ray optics including the modules developed and tested within the recent space projects. Various LE test modules were simulated, designed, assembled and tested at several X–ray test facilities. Selected results are briefly presented and discussed below.

2. Wide–Field Lobster Eye X-Ray Optics

The Lobster Eye (LE) optics mimic the arrangements of eyes of lobsters and was suggested in the 1970s for a very wide field X-ray imaging but used in space only very recently mostly due to severe manufacturing problems. Recently, advanced modules are available for both the Schmidt (Schmidt, 1975) and the alternative Angel (Angel, 1979) configurations, suitable for space applications.

Images in the eye of a lobster are formed through reflections off the internal walls of a lattice of small square-sided tubes arranged over the surface of a sphere. This design can be used in the construction of a grazing incidence system to focus X-rays.

The X-ray objective based on the lobster eye was proposed by (Angel, 1979), and similar design of a wide-field lens by (Schmidt, 1975). Each small channel is aligned along the radius of a sphere. A ray reflected twice off adjacent walls inside the channel is focused onto a spherical focal plane. Rays reflected only once are focused to a line causing background images to appear as a tapered cross. Some rays go through the lens with no reflections, contributing to diffuse background. The finite size of the tubes produces specific defocusing in the image, while the angle subtended by each tube at the focus limits the resolution of the system.

Despite these drawbacks, the great advantage of this design is an almost unlimited field of (Gorenstein, 1979; Gorenstein et al., 1996). This makes it ideal for use as an all-sky X–ray monitor. Up to 2017, no X–ray telescopes were launched using lobster-eye optics, mainly due to difficulty in manufacturing of the reflective tubes. However, improvements in multichannel plate technology has led to a proposal for a lobster-eye X-ray telescope could be placed on the International Space Station, and to an application on BeppiColombo (Fraser et al., 2010), and the alternative glass foil technology developed in the Czech Republic has lead to the construction of several first LE telescopes (Inneman et al., 1999, 2000). These efforts in the Czech Republic have started soon after announcing the idea of lobster optics (Hudec et al., 1995). The first LE module in space is the 1D LE optics on the VZLUSAT–1 minisatellite (Urban et al., 2017), see the dedicated section below.

The wide-field mirror modules offer advantageous application in astrophysics. The major scientific achievements of the X–ray astronomy in the past are closely related to the use of large X-ray imaging telescopes based mostly on the Wolter I X–ray objectives. These systems usually achieve excellent angular resolution as

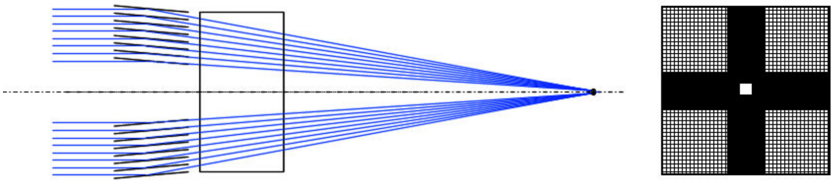

Figure 1.: LE 2D optics – composed of two 1D sub-modules, 2 reflections, energy range optical to 10 keV.

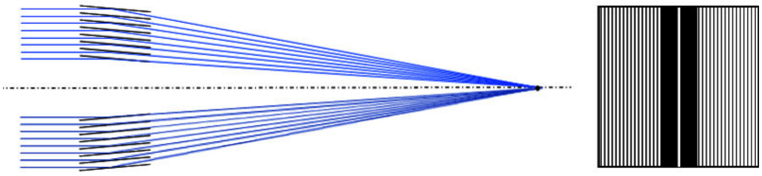

Figure 2.: LE 1D optics – 1 reflection, energy range optical to 30 keV.

well as very high sensitivity, but are quite limited in the field of view available, which is less than 1 degree in most cases. However, the future of X–ray astronomy and astrophysics requires not only detailed observations of particular triggers, but also precise and highly sensitive X–ray sky surveys, patrol and monitoring. The wide field lobster eye telescopes are hence expected to play an important role in future X–ray astrophysics missions and analyses.

The 2D LE optical system is illustrated on Fig. 1. For some applications where wider energy coverage (extension to harder X–rays) is necessary, the 1D LE system can be considered (Fig. 2). The imaging properties of these systems in optical light are documented in Fig. 3.

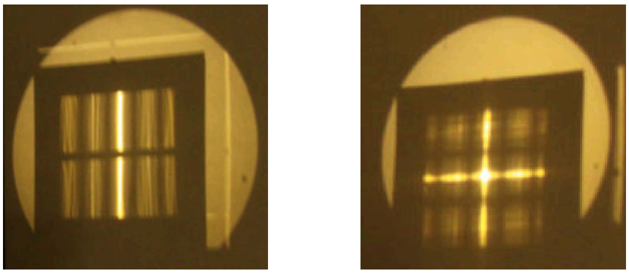

Figure 3.: LE system – test in visible light, left 1D, right 2D.

3. Simulations

For every Lobster Eye test module developed and assembled, ray–tracing simulations were performed in order to simulate the ideal imaging performance (Fig. 4). Few selected results are given below.

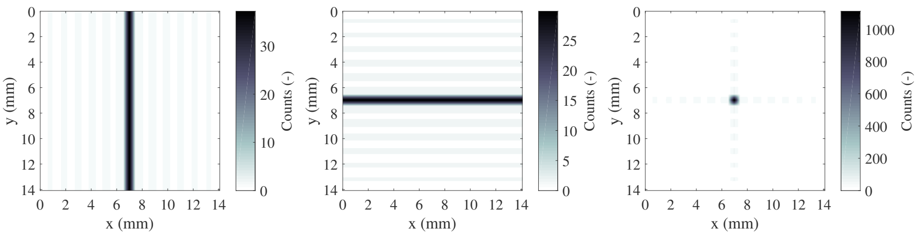

Figure 4.: REX LE optics simulation for source-detector distance 10 m at 8 keV, from left to right two 1D images and combined image.

4. Lobster Eye X–ray optics on VZLUSAT–1

The first LE X–ray optics in space is small Lobster Eye telescope onboard VZLUSAT–1. This cubesatellite represents example of 2U cubesatellite with advanced astrophysical payload onboard (Dániel et al., 2016). One from payloads is represented by one dimensional (Pína et al., 2016) miniature X–ray telescope (Pina et al., 2015) with Timepix detector in its focal plane (Baca et al., 2016). The main mission goal is technological verification of the system but scientific outcome is also expected for bright celestial X–ray sources (Urban et al., 2017; Dániel et al., 2016; Blazek et al., 2017). The satellite represents the 5th satellite with Czech X–ray optics onboard.

The 1D Lobster Eye module onboard VZLUSAT–1 has focal length of 250 mm and is composed of 116 wedges and 56 reflective double-sided gold-plated foils (thickness 145 microns) Input aperture is $29 \times 19\,\mathrm{mm}^2$, outer dimensions are $60 \times 28 \times 31\,\mathrm{mm}^3$. Active part of the foils is 19 mm in width and 60 mm in length and the energy range is 3 to 20 keV. The detailed parameters are documented in Tab. 1 and the pictures of the optics are in Fig. 5.

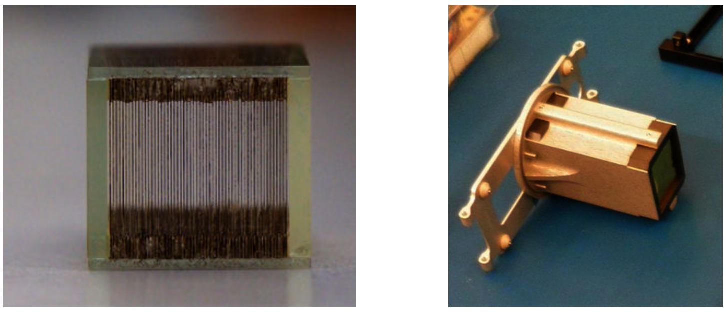

Figure 5.: The 1D LE module for the VZLUSAT–1 minisatellite (left), the 1D LE optics in frame (right).

At the time of writing, the VZLUSAT–1 X-ray payload was still in testing phase. The Timepix detector collects incident X–ray radiation on the satellite and all the electronics and communications of this experiment work well. In consequence of a temporary malfunction the attitude determination and control system (ADCS) and thus caused fast swinging of satellite, it is necessary to capture images with short exposure time. Obtaining images of the source in space is thus distinctively more difficult and statistically improbable. The first image was taken by Timepix on July 13, 2017 and were made more than 20 000 orbital measurements since launch. The results from the satellite operational phase will be presented in consecutive publications.

Table 1.: Parameters of the 1D LE optics for cubesat experiment VZLUSAT–1

Properties	Value
Aperture	$29 \times 19\,\mathrm{mm}^2$
FOV	3.3×2 degrees
Focal length	250 mm
Radius of convergence	500 mm
Dimensions of foils	$60 \times 25 \times 0.145\,\mathrm{mm}^3$
Number of foils	56
Spacing	0.3 mm
Reflective surface	Au
Effective area @ 8 keV and 80 % reflectivity	$\sim 0.5\,\mathrm{cm}^2$
Effective area @ 10 keV and 50 % reflectivity	$\sim 0.3\,\mathrm{cm}^2$
Angular resolution	2 arcmin
Detector	Timepix
Detection material	$300\,\mu$m Si detector
Detector resolution	256×256 pixels
Pixel size	$55\,\mu$m

5. Lobster Eye X–ray optics for rocket experiment

Another LE flight module was designed and manufactured for REX rocket experiment. The goal of this X-ray telescope is the Vela nebula observation during a sounding rocket flight. The Water Recovery X–ray Rocket (WRX–R) experiment is organized by the Pennsylvania State University (PSU), USA with a primary payload of a soft X-ray spectroscope. The Czech team developed a hard X-ray Lobster-eye telescope REX (see Fig. 6; left) as a secondary payload. The Czech experiments astrophysical object of study is the Vela pulsar in the centre of the Vela nebula.

The discussed optics for REX rocket experiment is two dimensional (2D) type. The LE module consists of two sub-modules addressed as Horizontal and

Table 2.: Parameters of the LE optics for rocket experiment REX

Properties	Value
Aperture	$54 \times 54\,\mathrm{mm}^2$
FOV	$1.3{\times}1.6$ degrees
Focal length	1 065 mm
Radius of convergence	2 130 mm
Dimensions of foils	$150 \times 75 \times 0.35\,\mathrm{mm}^3$
Number of foils in one sub–module	47
Spacing	0.75 mm
Reflective surface	Au
Effective area @ 8 keV and 80 % reflectivity	$\sim 1.4\,\mathrm{cm}^2$
Effective area @ 10 keV and 50 % reflectivity	$\sim 0.5\,\mathrm{cm}^2$
Angular resolution	1.1×1.4 arcmin
Detector	Timepix
Detection material	300 μm Si detector
Detector resolution	256×256 pixels
Pixel size	55 μm

Vertical in our case. The Horizontal sub-module is the one with longer focal length, closer to the observed object, which has mirrors oriented horizontally. The Vertical sub-module is placed closer to the camera, with mirrors placed vertically. The final optical system has focal length of 1065 mm and is composed of 114 wedges and 47 reflective single-sided gold-plated foils (thickness 350 microns) in each 1D module. Input aperture is $54 \times 54\,\mathrm{mm}^2$, outer dimensions of one 1D module are $80 \times 80 \times 170\,\mathrm{mm}^3$ and the active part of the foils is 54 mm in width and 150 mm in length. Total energy range is 1 to 15 keV over this energy range it work as soller slit. The main parameters of LE sub-modules are listed in Table 2 and a few selected measurement results are listed in next sections. For more information about the rocket experiment see (Dániel et al., 2017; Stehlikova et al., 2017).

6. X–ray tests at Boulder, Pennstate, Iowa and Prague

Several Lobster Eye modules were assembled and prepared for X–ray tests at the US and Czech test facilities. These LE modules were tested in vacuum chamber at CASA (University of Colorado at Boulder), taking into account the experimental arrangement of the test facility (focus to focus), hence these LE test modules were of focus to focus design, with source to optics distance: 10 m, optics to detector distance: 8 m, module position adjustment in visible light (Xe lamp), and a MCP detector as X–ray focal plane detector, with diameter of 1 inch.

Further X-ray tests were performed at X-ray test facilities in Iowa, Pennstate, and Prague, few selected results are illustrated below. For Pennstate tests, Timepix detector (Jakubek et al., 2014) was used to record the images.

The experimental setup at Pennstate test facility is in Fig. 6, examples of obtained results in Fig. 7. The comparison between simulation and experimental results for Prague measurement of VZLUSAT–1 1D module with used setup schema in Fig. 8 is in Fig. 9.

7. X–ray tests of LE module at PANTER

The full illumination X–ray tests of the LE module designed and assembled for the REX rocket experiment were performed at the Max Planck Institute for Extraterrestrial Physics PANTER facility, Germany in 2017. A few selected preliminary results are shown in Fig. 10. More details on these tests (including other types of X–ray optics) are given in another paper in this Volume (Pina et al., 2018).

8. Conclusions

Various LE X–ray optics modules were assembled and tested, based either on glass foils or high–quality silicon wafers, all of them in multi–foil arrangement, i.e. as stacked modules with flat X–ray reflecting substrates. These modules were tested at several X–ray test facilities, with very promising results, with around 1–2 arcmin FWHM in the best cases.

The LE X–ray optics represent promising alternative to widely used Wolter mirrors, mainly because of much larger FOV albeit at the cost of reduced angular resolution. The LE optics is suitable for use in wide–field X–ray monitors with very wide coverage of various astrophysical sources.

The availability of high-quality novel materials such as superior silicon wafers and/or glass foils enables the design and construction of LE X–ray optical systems with improved angular resolution for various applications both in space,

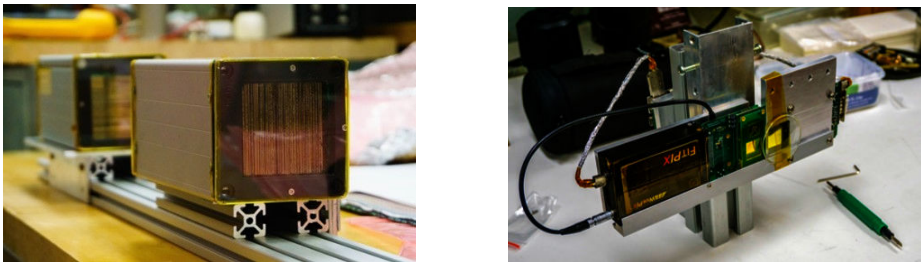

Figure 6.: X–ray tests at the Pennstate X-ray test facility. Left the REX LE module, right the Widepix detector used to record the focal images.

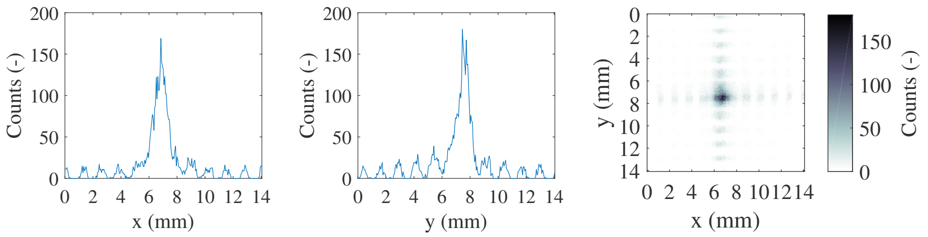

Figure 7.: X-ray tests of the REX LE module at the Pennstate X–ray test facility. The measured FWHM was 1.7 arcmin horizontal and 1.8 arcmin vertical.

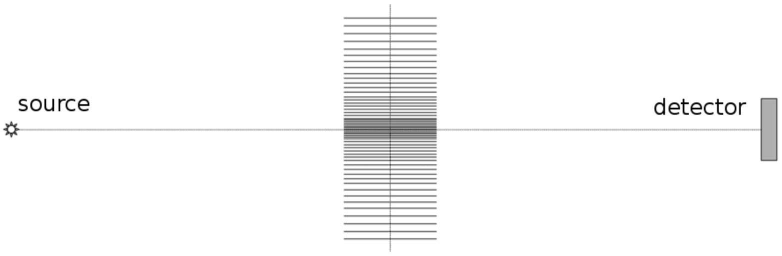

Figure 8.: Hard X–ray tests at RITE Prague, experimental setup. Cu K_α X-ray tube was used as source and Timepix as focal detector. LE optics was placed in the middle between source and detector.

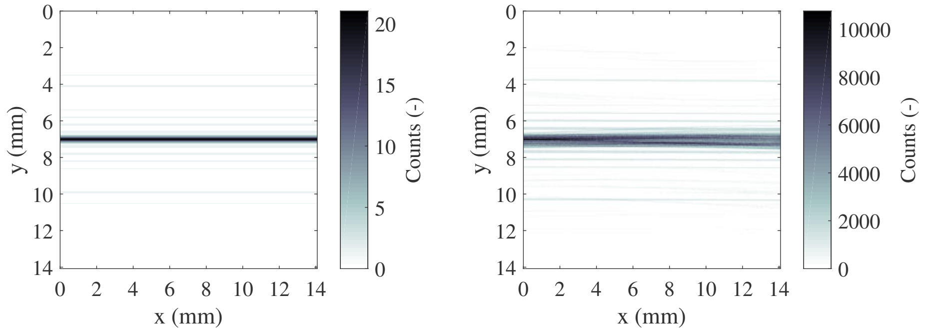

Figure 9.: Experimental tests of 1D LE optics, hard X-rays 8 keV at X–ray laboratory RITE Pregue, left simulated image, right measured image. Source – detector distance was 600 mm, exposure time 0.4 s and maximum signal = 104, after summation 18 × 105.

astronomy, as well as in the laboratory. In the near future, we plan to continue with assembling and testing LE modules with longer focal length and improved

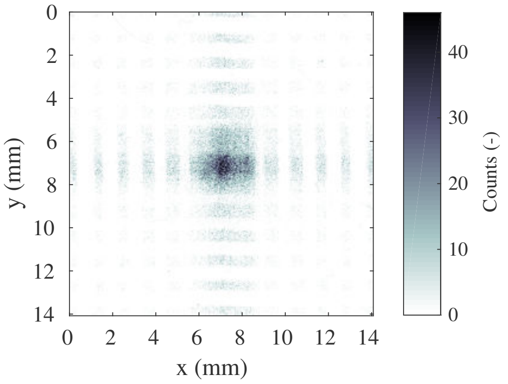

Figure 10.: LE REX PANTER X–ray test results. 2D LE X–ray optics (REX) – image of the 2D focus at 8.04 keV for different focal distance. Best focus in vertical direction 1.21 mm FWHM (1.5 arcmin) and in horizontal direction 0.94 mm (1.3 arcmin).

performance, based on superior quality substrates.

Acknowledgements. We thanks the teams at the X–ray test facilities at Boulder, Pennstate, Iowa and MPE PANTER for their assistance and help with measurements of LE modules there.

We acknowledge GA CR grants 13-33324S, 18-10088Y and AHEAD EU Horizon 2020 project (Integrated Activities in the High Energy Astrophysics Domain), grant agreement n. 654215. This work was partly supported by the Grant Agency of the Czech Technical University in Prague, grant No. SGS18/186/OHK3/3T/13 and MEYS RVO 68407700 as well.

References

Angel, J. R. P., Lobster eyes as X-ray telescopes. 1979, *Astrophys. J.*, **233**, 364, DOI: 10.1086/157397

Baca, T., Platkevic, M., Jakubek, J., et al., Miniaturized X-ray telescope for VZLUSAT-1 nanosatellite with Timepix detector. 2016, *Journal of Instrumentation*, **11**, C10007, DOI: 10.1088/1748-0221/11/10/C10007

Blazek, M., Pata, P., Inneman, A., & Skala, P., Astronomical Tasks for Tests of X-Ray Optics in VZLUSAT-1 Nanosatellite. 2017, *Advances in Astronomy*, **2017**, 316289, DOI: 10.1155/2017/3162892

Dániel, V., Inneman, A., Pína, L., et al., X-ray Lobster Eye all-sky monitor for rocket experiment. 2017, in Society of Photo-Optical Instrumentation Engineers (SPIE) Conference Series, Vol. **10235**, *Society of Photo-Optical Instrumentation Engineers (SPIE) Conference Series*, 1023503

Dániel, V., Pína, L., Inneman, A., et al., Terrestrial gamma-ray flashes monitor demonstrator on CubeSat. 2016, in Proceedings of the SPIE, Vol. **9978**, *CubeSats and NanoSats for Remote Sensing*, 99780D

Fraser, G. W., Carpenter, J. D., Rothery, D. A., et al., The mercury imaging X-ray spectrometer (MIXS) on bepicolombo. 2010, *Planet. Space Sci.*, **58**, 79, DOI: 10.1016/j.pss.2009.05.004

Gorenstein, P., X-ray optics for the LAMAR facility, an overview. 1979, in Proc. SPIE, Vol. **184**, *Space optics: Imaging X-ray optics workshop*, ed. M. Weisskopf, 63–72

Gorenstein, P., Whitbeck, E., Austin, G. K., et al., Lobster-eye x-ray telescope prototype. 1996, in Proc. SPIE, Vol. **2805**, *Multilayer and Grazing Incidence X-Ray/EUV Optics III*, ed. R. B. Hoover & A. B. Walker, 74–80

Hudec, R., Inneman, A., Pina, L., Řehák, P., & Gorenstein, P., Wide-field X-ray optics. 1995, in Lecture Notes in Physics, Berlin Springer Verlag, Vol. **454**, *IAU Colloq. 151: Flares and Flashes*, ed. J. Greiner, H. W. Duerbeck, & R. E. Gershberg, 435

Inneman, A., Hudec, R., Pina, L., & Gorenstein, P., Lobster eye x-ray optics. 1999, in Proc. SPIE, Vol. **3766**, *X-Ray Optics, Instruments, and Missions II*, ed. R. B. Hoover & A. B. Walker, 72–79

Inneman, A. V., Hudec, R., & Pina, L., Progress in lobster-eye x-ray optics development. 2000, in Proc. SPIE, Vol. **4138**, *X-Ray Optics, Instruments, and Missions IV*, ed. R. B. Hoover & A. B. Walker, 94–104

Jakubek, J., Jakubek, M., Platkevic, M., et al., Large area pixel detector WIDEPIX with full area sensitivity composed of 100 Timepix assemblies with edgeless sensors. 2014, *Journal of Instrumentation*, **9**, C04018, DOI: 10.1088/1748-0221/9/04/C04018

Pina, L., Hudec, R., Inneman, A., et al., X-ray monitoring for astrophysical applications on Cubesat. 2015, in Proceedings of the SPIE, Vol. **9510**, *EUV and X-ray Optics: Synergy between Laboratory and Space IV*, 951005

Pina, L., Hudec, R., Inneman, A., et al., Multi Foil X-ray Optics Tests at PANTER: Preliminary Results. 2018, *Contributions of the Astronomical Observatory Skalnaté Pleso*

Pína, L., Hudec, R., Inneman, A. J., et al., Development and tests of x-ray multifoil optical system for 1D imaging (Conference Presentation). 2016, in Proceedings of the SPIE, Vol. **9964**, *Advances in Laboratory-based X-Ray Sources, Optics, and Applications V*, 99640B

Schmidt, W. K. H., A proposed X-ray focusing device with wide field of view for use in X-ray astronomy. 1975, *Nuclear Instruments and Methods*, **127**, 285, DOI: 10.1016/0029-554X(75)90501-7

Stehlikova, V., Urban, M., Nentvich, O., et al., Hard X-ray Vela supernova observation on rocket experiment WRX-R. 2017, *Contributions of the Astronomical Observatory Skalnate Pleso*, **47**, 165

Urban, M., Nentvich, O., Stehlikova, V., et al., VZLUSAT-1: Nanosatellite with miniature lobster eye X-ray telescope and qualification of the radiation shielding composite for space application. 2017, *Acta Astronautica*, **140**, 96, DOI: 10.1016/j.actaastro.2017.08.004

Contrib. Astron. Obs. Skalnaté Pleso **48**, 466 – 475, (2018)

Multi-Foil X–ray optics tests at PANTER: Preliminary results

L. Pina[1], R. Hudec[2,3], A. Inneman[2], O. Nentvich[2], M. Urban[2], V. Marsikova[2], V. Stehlíková[2], D. Doubravova[4], V. Burwitz[5], C. Pelliciari[5], G. Hartner[5] and V. Daniel[6]

[1] *Czech Technical University in Prague, Faculty of Nuclear Sciences and Physical Engineering, Brehova 7, Prague 115 19, Czech Republic*

[2] *Czech Technical University in Prague, Faculty of Electrical Engineering, Technicka 2, Prague 166 27, Czech Republic*
(E-mail: hudecren@fel.cvut.cz)

[3] *Engelhardt Astronomical observatory, Kazan Federal University, Kremlyovskaya street 18, 420008 Kazan, Russian Federation*

[4] *Advacam, U Pergamenky 12, 170 00 Praha 7, Czech Republic*

[5] *Max Planck Institute for Extraterrestrial Physics, Giessenbachstrasse, 85748 Garching, Germany*

[6] *Czech Aerospace Research Centre, Beranovych 130, Prague 199 05, Czech Republic*

Received: December 20, 2017; Accepted: March 23, 2018

Abstract. We present and discuss preliminary test results performed with selected modules of Multi–Foil X–ray Optics in the MPE PANTER X–ray test facility. Three X–ray optics Multi–Foil modules were tested, namely 1D Kirkpatrick-Baez module, 2D Kirkpatrick-Baez module, both developed within the EU Horizon 2020 AHEAD Project, as well as the Lobster–Eye module REX for the rocket flight experiment.

Key words: X–ray optics – X–ray telescopes – X–ray test facilities – X–ray astrophysics

1. Introduction

In this short contribution, we present very preliminary results of tests of selected X–ray optics in Multi–Foil Optics (MFO) arrangements, namely Kirkpatrick-Baez (KB) and Lobster-Eye (LE) (Hudec, 2010; Inneman et al., 1999) test modules in the MPE PANTER X–ray test facility in Neuried, Germany (Burwitz et al., 2013, 2017; Freyberg et al., 2008). In these full aperture X–ray optical tests, two KB modules and one LE module were tested. The very preliminary results are briefly summarised below.

2. AHEAD WP on X–ray Optics

The work within the optics works package of EU AHEAD project (Piro et al., 2015) comprises studying, simulating and ray tracing the current optical design possibilities for three X-ray optics geometries, namely Wolter–I, Kirkpatrick-Baez, and Lobster-Eye. An assessment and modeling of inherent aberrations of the investigated technologies will be performed to determine a detailed error budget break-down of all the contributions which limit the angular resolution, size of the field of view and collecting area. A detailed simulation of instrument response for all cases will allow a prediction of the scientific performance. Also studies of different substrates Si vs. Glass for the KB modules will be carried out. For all the tests the setup geometry in PANTER will be optimised for each optic and the analysis software modified so that the consistency between measurement and simulations can be adequately checked.

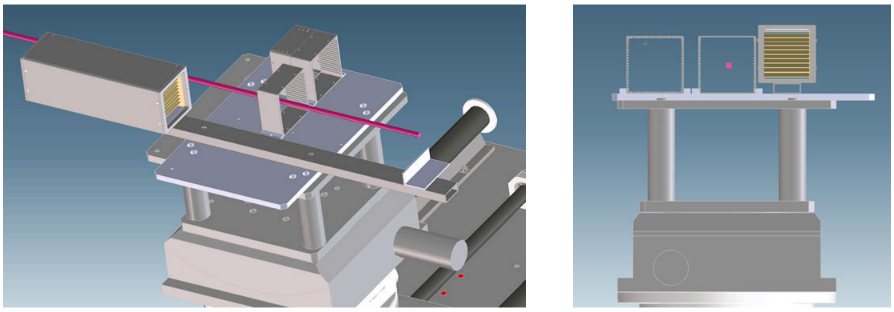

Figure 1.: A sketch of the setup of the MFO modules in the vacuum chamber of PANTER (in the left panel, from left to right REX optics, 1D KB optics, 2D KB optics). In the right panel the sequence is REX, 1D-KB, 2D-KB from right to left.

The AHEAD optics programme aims at simulating, producing and testing prototype X–ray optics using four key technologies as follows.

- Silicon Pore Optics (SPO) developed by ESA/Cosine for the Wolter-I geometry ATHENA telescope. SPO will also be studied for use in KB geometry.
- Square pore micro-channel plates for Lobster Eye module development.
- Slumped glass optics applicable to the Wolter I geometry or KB.
- Silicon wafer optics for the construction of KB optics.

All the X–ray tests here presented were performed at the PANTER X-ray test facility (Burwitz et al., 2017), characterization tests of the industrial production will be performed with BEaTriX (Spiga et al., 2017). The PANTER

X–ray test facility has for over a period of 35 years been involved in the developing, testing and calibrating X–ray optics for most X-ray satellite observatories that have flown to date (especially for ROSAT and XMM–Newton). This wealth of experience will be used in the design, preparation, and implementation of the X–ray tests within the AHEAD project. In the last years, PANTER has been upgraded and optimized to measure X–ray optics with a large focal length (up to f = 20 m, e.g. ATHENA has f = 12 m) (Burwitz et al., 2013, 2017; Freyberg et al., 2008).

In the AHEAD project, the PANTER X-ray test facility is expected to perform the following tasks

- Optimisation (materials and geometry) of a collimated beam using a zone plate sector approach.
- Design and implementation of X–ray test setups.
- Perform the measurements of the different X-ray optics.
- Developing software for analysing the test specific data.
- Optical analysis of the results and comparison with simulation.
- Characterization of high resolution X–ray optics units (HEW ≤ 5 arcsec)

3. AHEAD KB test modules for PANTER tests

The first KB modules (see Fig. 2 and Tab. 1) designed and assembled within the AHEAD project (Piro et al., 2015) were tested (see test setup in Fig. 1 and Fig. 2) at the Max Planck Institute for extraterrestrial Physics at the PANTER facility in Neuried, Germany in 2017, with preliminary results discussed below.

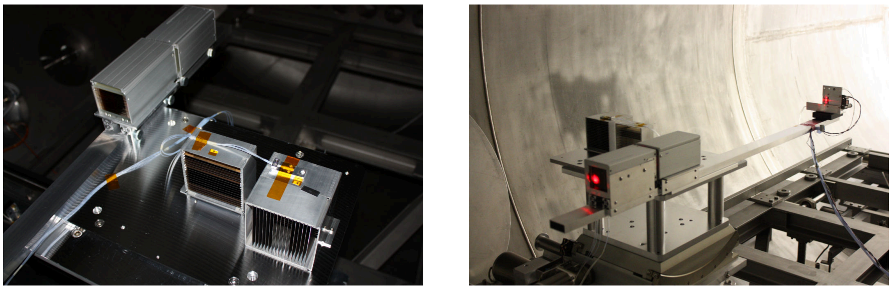

Figure 2.: The tested MFO modules inside PANTER facility (in the left picture from left to right REX optics, 1D KB optics, 2D KB optics). In the right panel REX optics with Timepix detector illuminated by laser beam.

Table 1.: Parameters of KB X-ray optics module for PANTER X ray tests. These parameters are for one 1D KB sub-module. Full 2D KB system is represented by 2 analogous modules (Hudec et al., 2018a).

Properties	Value
Aperture	$80 \times 80\,\mathrm{mm}^2$
FOV	$0.5{\times}0.5$ degrees
Focal length	6 500 mm
Dimensions of foils	$50 \times 100 \times 0.625\,\mathrm{mm}^3$
Number of foils in one sub–module	17
Spacing	4.5 mm
Reflective surface	Au
Detector	TRoPIC
Detector resolution	256×256 pixels
Pixel size	$75\,\mu$m

Each module consists of 17 pieces of thin parabolic silicon foils (thickness 0.625 mm) which are arranged such that the focal length corresponds to around 6.5 meters (theoretical). The field of view (FOV) of this X–ray optics is 30 arcmin. The module housing was manufactured from aluminium alloy. External dimensions of 1D module are approximately $105 \times 105 \times 50\,\mathrm{mm}^3$. The sub-module A in 2D X-ray optics was more distant from the detector and foils were in the vertical arrangement. The sub-module B was closer to detector and foils were in the horizontal arrangement, as illustrated in Fig. 3. The Si substrates represent promising alternative to glass foils used in MFO nowadays (Hudec et al., 2006, 2008a,b, 2009).

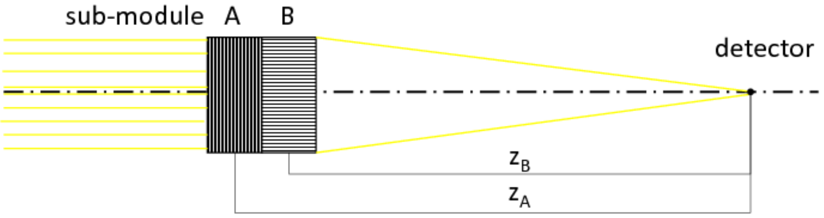

Figure 3.: Mounting configuration of the 2D-KB and LE optics during Panter tests.

4. Lobster Eye X–ray optics REX for PANTER tests

In addition to the AHEAD KB modules described above, LE flight module designed and manufactured for the REX rocket experiment was also tested in the same experiment (Hudec et al., 2018b). The Water Recovery X–ray Rocket (WRX–R) experiment is organized by the Pennsylvania State University (PSU), USA with a primary payload of a soft X-ray spectroscope. The Czech team developed the hard X-ray Lobster-eye telescope REX as a secondary payload. The basic optics parameters are listed in the Tab. 2, and preliminary measurement results are listed in the next sections. For more details on the rocket experiment see Dániel et al. (2017); Stehlikova et al. (2017).

Table 2.: Parameters of the LE optics for rocket experiment REX (Hudec et al., 2018b)

Properties	Value
Aperture	$54 \times 54\,\mathrm{mm}^2$
FOV	$1.3{\times}1.6$ degrees
Focal length	1 065 mm
Radius of convergence	2 130 mm
Dimensions of foils	$150 \times 75 \times 0.35\,\mathrm{mm}^3$
Number of foils in one sub–module	47
Spacing	0.75 mm
Reflective surface	Au
Effective area @ 8 keV and 80 % reflectivity	$\sim 1.4\,\mathrm{cm}^2$
Effective area @ 10 keV and 50 % reflectivity	$\sim 0.5\,\mathrm{cm}^2$
Angular resolution	1.1×1.4 arcmin
Detector	Timepix
Detection material	$300\,\mu$m Si detector
Detector resolution	256×256 pixels
Pixel size	$55\,\mu$m

The 2D LE X-ray optic REX is composed of two 1D sub-modules. The modules were assembled using MFO technology. Each module consists of 47 pieces of thin flat glass foils (thickness 0.35 mm) which are arranged such that the focal length is around 1.0 meter. The gold coating allows the material to reflect X–ray photons incoming under small incident angle of up to 0.5 deg. The field of view of X-ray optics is around 1.5 deg. The housing of the module is made of an aluminium alloy. The external dimensions of the 1D module are approximately $80 \times 80 \times 170\,\mathrm{mm}^3$. The sub-module A of 2D LE X–ray optics was more distant from detector and foils were in the vertical arrangement. The sub-module B was closer to detector and foils were in the horizontal arrangement.

5. X–ray tests of MFO at PANTER

The full illumination X–ray tests of the KB and LE modules designed and assembled for the AHEAD project and for the REX rocket experiment were performed at the vacuum beamline of the MPE PANTER facility in Neuried (Germany) in 2017, with preliminary results briefly presented below.

5.1. KB AHEAD Optics tests

The AHEAD KB X-ray optics was tested at 3 different energies, namely Al–Kα (1.49 keV), Ti–Kα (4.51 keV)/ Ti–Kβ (4.93 keV) and Cu–Kα (8.04 keV). The TRoPIC CCD detector (PANTER) with 256×256 px (75 μm pixel size, area of $19.2\,\mathrm{mm} \times 19.2\,\mathrm{mm}$) was used. The exposure time was 15 min.

The optimal focus was investigated at energy of 1.49 keV with aluminium (Al–Kα) anode and 10 μm thick Al filter, the high voltage (HV) power supply was set to 2.9 kV anode voltage. The optimal focus in the X-axis direction was measured as 1.1 mm (vertical 1D module A), then in the y-axis direction was measured as 2.1 mm (horizontal 1D module B) which can be seen the Fig. 4. The best focus for the whole KB 2D X–ray optics was looked for which is presented in (Hudec et al., 2018a). Because of different focal lengths of each sub-module the best focal length for 2D optics was found as their compromise. The 2D focus is in the Fig. 5, its FWHM was measured as 3.2 mm in vertical and 2.8 mm in horizontal direction. see Fig. 6.

5.2. LE REX Optics tests

The X–ray optics was tested at 3 different energies: Ag – Lα (2.89 keV), Ti–Kα (4.51 keV)/ Ti–Kβ (4.93 keV) and Cu–Kα (8.04 keV). The Timepix detector with 256×256 px (55 μm pixel size, $14.1\,\mathrm{mm} \times 14.1\,\mathrm{mm}$ area) was used during tests (Jakubek et al., 2014). The exposure time was 15 min.

PANTER measurements with REX optics and Timepix detector allowed the spectrum of reflected radiation to be analysed in the detection plane. Spectral plots show the spectrum of individual sources used for the experiment and con-

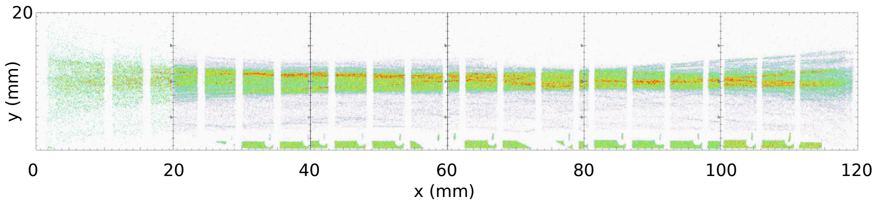

Figure 4.: The KB 2D X–ray optics – image of whole 1D focus in y direction (horizontal) at 1.49 keV.

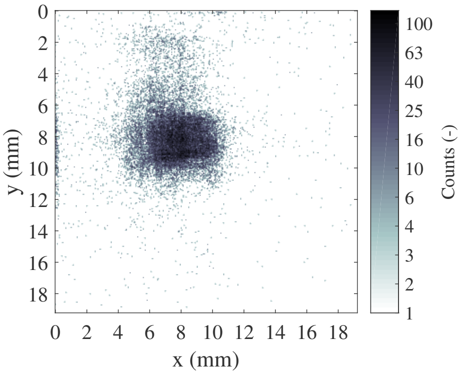

Figure 5.: AHEAD KB 2D X–ray optics – the best 2D focus at 1.49 keV, 33 arcsec FWHM (Hudec et al., 2018a).

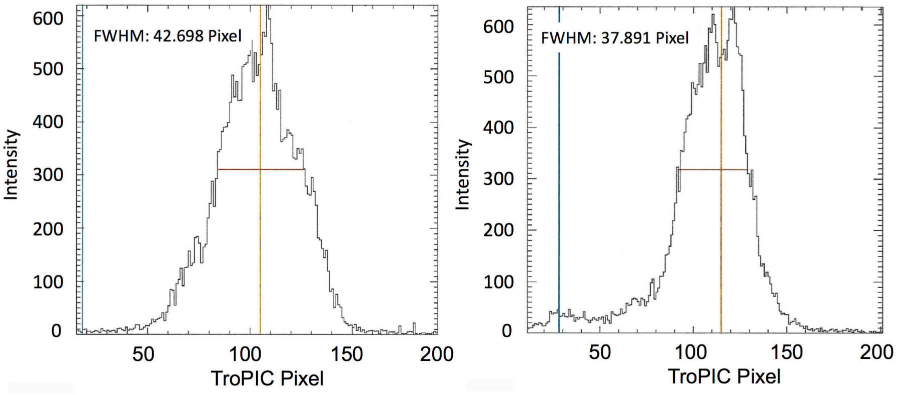

Figure 6.: The KB 2D X–ray optics – left FWHM of focus in vertical direction (3.2 mm), right FWHM of focus in horizontal direction (2.8 mm) at 1.49 keV.

firm that the REX optics operates in the energy range of 3 keV to 8 keV (higher energy could not be measured at this time due to experimental constraints).

The optimal focus was searched for an energy of 8.04 keV with copper anode (Cu-Kα) and 10 μm thick Al filter, the HV power supply was set to 15 kV anode voltage. The 1D modules and detector were tightly connected, so that 1D focus could not be investigated and only 2D focus was measured, see Fig. 7 and Fig. 8.

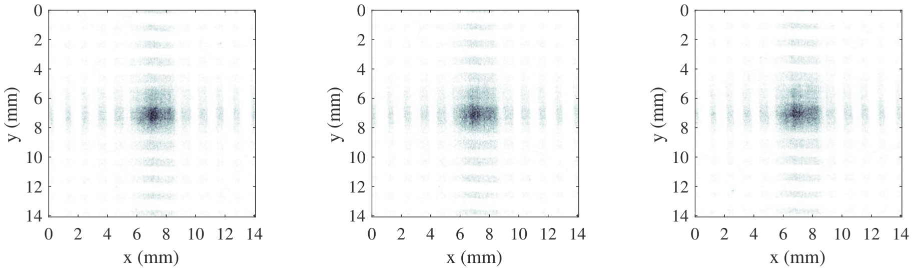

(a) 0 mm (b) + 50 mm (c) + 100 mm

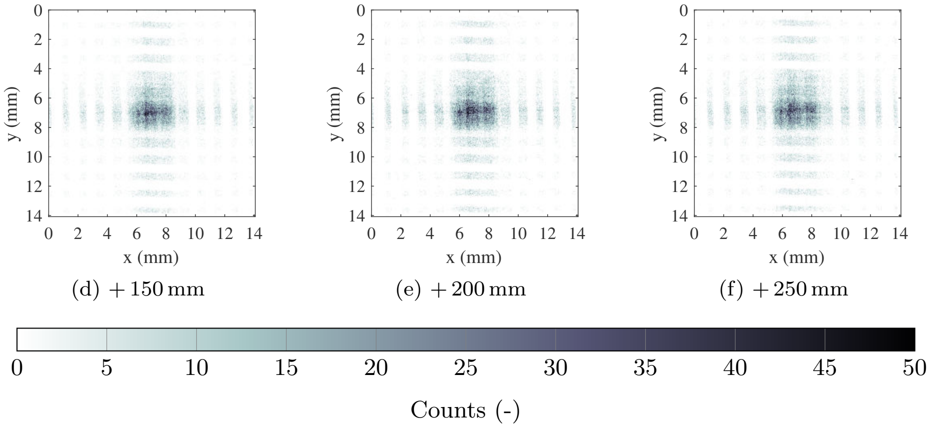

(d) + 150 mm (e) + 200 mm (f) + 250 mm

Figure 7.: The LE X–ray optics (REX) – image of the 2D focus at 8.04 keV for different focal distances - relative shift is shown in sub-figures (a) to (f).

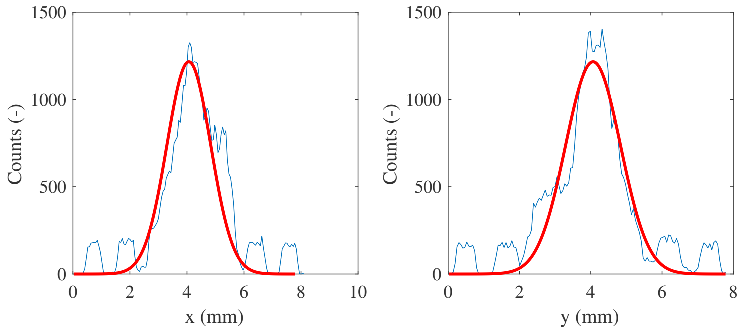

Figure 8.: The REX LE X–ray optics, the best focus – left FWHM of focus in horizontal direction (1.82 mm), right FWHM of focus in vertical direction (2.05 mm) at 8.04 keV at relative position + 0 mm.

6. Conclusions

The two types of X-ray optics were tested at the PANTER X–ray test facility – Kirkpatrick-Baez 1D and 2D modules with silicon foils and theoretical focal length of 6.5 m and Lobster Eye 2D module with glass foils and theoretical focal length of 1 m.

For the 2D X–ray KB optics, the best focus for the vertical sub-module was found to be 1.1 mm (18 arcsec) and for horizontal sub-module was 2.1 mm FWHM (33 arcsec). The combination of both sub-modules was not optimal thus the best 2D focus was $3.2 \times 2.8\,\mathrm{mm}^2$.

The X–ray measurements indicate that for the KB modules, the focal length is shorter than the theoretical assumption perhaps due to the x-ray test beam divergence.Unfortunately, the experimental setup did not allow to move the detector closer to the optics that is why the best focus was not achieved. Consequently, the real FWHM of the modules is very probably better than the measured value.

For the 2D X-ray LE optics (REX), the best focus in the vertical direction was found 2.05 mm FWHM and in horizontal direction FWHM 1.82 mm. Nowadays is this optical system (2D optic + Timepix detector) installed in Water Recovery X-ray Rocket and prepared for launch (Spring 2018).

The preliminary results of the full aperture X–ray optical tests of the MFO modules at the MPE PANTER facility confirm the expectations. It should be taken into account that the tested modules were based on standard commercially available substrates, namely silicon wafers for KB modules, and glass foils for LE module. Application of superior quality substrates, especially Si, considered for future modules, is expected to result in even better imaging performance.

Acknowledgements. We acknowledge GA CR grants 13-33324S, 18-10088Y and AHEAD EU Horizon 2020 project (Integrated Activities in the High Energy Astrophysics Domain), grant agreement n. 654215. We thank the teams at the X–ray test facility MPE PANTER for their assistance and help with measurements of MFO modules there. This work was partly supported by the Grant Agency of the Czech Technical University in Prague, grant No. SGS18/186/OHK3/3T/13 and MEYS RVO 68407700 as well.

References

Burwitz, V., Bavdaz, M., Pareschi, G., et al., In focus measurements of IXO type optics using the new PANTER x-ray test facility extension. 2013, in Proc. SPIE, Vol. **8861**, *Optics for EUV, X-Ray, and Gamma-Ray Astronomy VI*, 88611J

Burwitz, V., Willingale, R., Pellilciari, C., Hartner, G., & La Caria, M.-M., Testing and calibrating the ATHENA optics at PANTER (Conference Presentation). 2017, in Society of Photo-Optical Instrumentation Engineers (SPIE) Conference Series, Vol. **10399**, *Society of Photo-Optical Instrumentation Engineers (SPIE) Conference Series*, 103990O

Dániel, V., Inneman, A., Pína, L., et al., X-ray Lobster Eye all-sky monitor for rocket experiment. 2017, in Society of Photo-Optical Instrumentation Engineers (SPIE) Conference Series, Vol. **10235**, *Society of Photo-Optical Instrumentation Engineers (SPIE) Conference Series*, 1023503

Freyberg, M. J., Budau, B., Burkert, W., et al., New technology and techniques for x-ray mirror calibration at PANTER. 2008, in Proc. SPIE, Vol. **7011**, *Space Telescopes and Instrumentation 2008: Ultraviolet to Gamma Ray*, 701117

Hudec, R., Kirkpatrick-Baez (KB) and Lobster Eye (LE) Optics for Astronomical and Laboratory Applications. 2010, *X-Ray Optics and Instrumentation, 2010. Special Issue on X-Ray Focusing: Techniques and Applications, id.139148*, **2010**, 139148, DOI: 10.1155/2010/139148

Hudec, R., Marsikova, V., Mika, M., et al., Advanced x-ray optics with Si wafers and slumped glass. 2009, in Proc. SPIE, Vol. **7437**, *Optics for EUV, X-Ray, and Gamma-Ray Astronomy IV*, 74370S

Hudec, R., Pina, L., Marsikova, V., et al., Kirkpatrick Baez X–ray optics for astrophysics: Recent status. 2018a, *Contributions of the Astronomical Observatory Skalnate Pleso*, **48**, 437

Hudec, R., Pina, L., Marsikova, V., et al., Lobster Eye X-ray optics for astrophysics: Recent status. 2018b, *Contributions of the Astronomical Observatory Skalnaté Pleso*, **48**, 456

Hudec, R., Pina, L., Sveda, L., et al., Novel Approaches in Technologies for Large Light-Weight X-ray Space Telescopes. 2006, in ESA Special Publication, Vol. **604**, *The X-ray Universe 2005*, ed. A. Wilson, 969

Hudec, R., Semencová, V., Inneman, A., et al., Novel Technologies for Astronomical X-ray Telescopes. 2008a, in *The X-ray Universe 2008*, 254

Hudec, R., Sik, J., Lorenc, M., et al., Recent progress with x-ray optics based on Si wafers and glass foils. 2008b, in Proc. SPIE, Vol. **7011**, *Space Telescopes and Instrumentation 2008: Ultraviolet to Gamma Ray*, 701116

Inneman, A., Hudec, R., Pina, L., & Gorenstein, P., Lobster eye x-ray optics. 1999, in Proc. SPIE, Vol. **3766**, *X-Ray Optics, Instruments, and Missions II*, ed. R. B. Hoover & A. B. Walker, 72–79

Jakubek, J., Jakubek, M., Platkevic, M., et al., Large area pixel detector WIDEPIX with full area sensitivity composed of 100 Timepix assemblies with edgeless sensors. 2014, *Journal of Instrumentation*, **9**, C04018, DOI: 10.1088/1748-0221/9/04/C04018

Piro, L., Natalucci, L., & Ahead Consortium, AHEAD: Integrated Activities in the High Energy Astrophysics Domain. 2015, in *Exploring the Hot and Energetic Universe: The first scientific conference dedicated to the Athena X-ray observatory*, ed. M. Ehle, 74

Spiga, D., Pareschi, G., Salmaso, B., & Tagliaferri, G. 2017, BEaTriX X-ray facility for testing ATHENA mirror modules: a white paper for the implementation

Stehlikova, V., Urban, M., Nentvich, O., et al., Hard X-ray Vela supernova observation on rocket experiment WRX-R. 2017, *Contributions of the Astronomical Observatory Skalnate Pleso*, **47**, 165

Contrib. Astron. Obs. Skalnaté Pleso **48**, 476 – 487, (2018)

Rapid X-ray variability and properties of compact stars

G. Török, K. Goluchová and E. Šrámková

Institute of Physics and Research Centre for Computational Physics and Data Processing, Silesian University in Opava, Bezručovo nám. 13, CZ-746 01 Opava, Czech Republic, (E-mail: gabriel.torok@gmail.com)

Received: December 4, 2017; Accepted: March 28, 2018

Abstract. The Rossi X-ray timing explorer, which operated from 1995 to 2012, has provided a large amount of NS data. Timing analysis of the X-ray flux in more than a dozen NS systems reveals remarkable correlations between frequencies of two characteristic peaks present in the high-frequency part of the power-density spectra. We discuss a simple analytic relation that well reproduces these correlations. We outline a possible physical interpretation of the relation's parameters and explore the impact of the obtained results in a broader context.

Key words: X-Rays: Binaries – Accretion, Accretion Discs – Stars: Neutron

1. Introduction

Low-mass X-ray binaries (LMXBs) provide a unique opportunity to probe the effects associated with strong gravity in both black hole (BH) and neutron star (NS) systems (van der Klis, 2006). In the case of NS systems they may serve as a good tool for exploration of the supra-dense matter (Lewin et al., 1997).

The Proportional Counter Array aboard the Rossi X-ray timing explorer (PCA, RXTE Bradt et al., 1993; Jahoda et al., 1996), which operated from 1995 to 2012, has provided observations of NS sources that reveal the existence of two characteristic peaks present in the high-frequency part of the power-density spectra (twin-peak QPOs). In Figure 1a we illustrate correlations between twin-peak QPO frequencies in terms of the upper and lower QPO frequency, ν_U and ν_L, for a group of 14 sources including 8 atoll sources, 5 Z sources, and one milisecond X-ray pulsar. These 14 sources are listed in Table 1. At present there is no commonly accepted model that could explain the observed correlations. Nevertheless, based on various strong arguments, it is usually expected that the twin-peak QPOs are related to orbital motion in the vicinity of NSs. Miscellaneous concepts have been proposed to explain the observed phenomenon (Alpar & Shaham, 1985; Lamb et al., 1985; Miller et al., 1998; Psaltis et al., 1999; Stella & Vietri, 2001; Wagoner et al., 2001; Kluźniak & Abramowicz, 2001; Abramowicz & Kluźniak, 2001; Kato, 2001; Titarchuk & Wood, 2002; Abramowicz et al., 2003; Rezzolla et al., 2003; Kluźniak et al., 2004; Zhang, 2004; Pétri, 2005;

Bursa, 2005; Čadež et al., 2008; Wang et al., 2008; Mukhopadhyay, 2009; Bachetti et al., 2010; Dönmez et al., 2011; Stuchlík et al., 2013; Stuchlík & Kološ, 2014; Huang et al., 2016; Le et al., 2016; Germanà, 2017, and several others).

2. Orbital models

Various attempts to model the individual observed correlations with simple orbital models assuming test particle motion or oscillating pressure-supported fluid structures in the slender torus limit approximation have been rather unsuccessful (see, e.g., Lin et al., 2011; Török et al., 2010, 2012, 2016b, and references therein). In Figure 1a we include an example of correlation predicted by a particular geodesic model, the so-called relativistic precession model (Morsink & Stella, 1999; Stella & Vietri, 1998, 1999, in the following RP model). This correlation is compared to the prediction of a non-geodesic model recently proposed by Török et al. (2016a) to which we in the following refer as the CT (Cusp Torus) model. Both curves in the Figure are drawn for a non-rotating NS with gravitational mass $M = 1.7 M_{\odot}$.

2.1. The RP model

The RP model in its usual form incorporates the assumption that the observed rapid X-ray variability originates in the orbital motion of hot inhomogeneities orbiting in the innermost parts of the accretion disc. Within this framework the frequencies of the two observed QPOs are related to the Keplerian frequency ν_{K} and the relativistic precession frequency ν_{P} of slightly perturbed circular geodesic motion that occurs at an arbitrary orbital radius r,

$$\nu_{\mathrm{U}}(r) = \nu_{\mathrm{K}}(r), \quad \nu_{\mathrm{L}}(r) = \nu_{\mathrm{P}}(r)\,. \tag{1}$$

The precession frequency equals to a difference between the Keplerian and the radial epicyclic frequency, $\nu_{\mathrm{P}}(r) = \nu_{\mathrm{K}}(r) - \nu_{\mathrm{r}}(r)$.

It has been shown that relation (1) roughly matches the data of NS sources (e.g., Stella & Vietri, 1998, 1999; Belloni et al., 2007; Lin et al., 2011; Török et al., 2012, 2016b). It is however questionable whether the local motion of an individual spot can be responsible for the high amplitudes and coherence times of the observed QPOs (e.g., Barret et al., 2005a; Méndez, 2006; Barret & Vaughan, 2012).

2.2. The CT model

The CT model explored recently by Török et al. (2016a) deals with global modes of accreted fluid motion in an oscillating torus (Rezzolla et al., 2003; Abramowicz et al., 2006; Blaes et al., 2006; Šrámková et al., 2007; Ingram & Done, 2010; Fragile et al., 2016; Mishra et al., 2017; Parthasarathy et al., 2017; de Avellar et al., 2017). The torus is assumed to form a cusp by filling up the so-called critical equipotential volume. The upper kilohertz QPO frequency is assigned to the Keplerian frequency of the fluid at the centre of the torus where both the fluid pressure and the density peak, and from which most of the torus radiation emerges. The lower kilohertz QPO frequency is assigned to the frequency of a non-axisymmetric $m = -1$ radial epicyclic mode, $\nu_{\mathrm{r},-1}$. It is expected that the torus at all times keeps its maximal possible size filling the 'Roche-like' lobe, and that its radial oscillations modulate the boundary layer accretion flow (Paczynski, 1987; Horák, 2005; Abramowicz et al., 2007; Parthasarathy et al., 2017).

The QPO frequencies predicted by the CT model are functions of the torus centre location r_0,

$$\nu_U \equiv \nu_K(r_0), \quad \nu_L \equiv \nu_{\mathrm{r},-1}(r_0)\,. \tag{2}$$

Rather long analytic formulae that define $\nu_{\mathrm{r},-1}$ can be found in Straub & Šrámková (2009). Török et al. (2016a) numerically calculated the $\nu_L(\nu_U)$ correlation following from relation (2). Assuming this correlation, they obtained a good match of the data in the case of the atoll source 4U 1636-53 for NS mass of $M = 1.69M_\odot$ (see Figure 1b for illustration).

3. Simple analytical formula

In Török et al. (2017a) we suggested that the $\nu_L(\nu_U)$ frequency relations can be well described by the following formula

$$\nu_L = \nu_U \left(1 - \mathcal{B}\sqrt{1 - (\nu_U/\nu_0)^{2/3}}\right), \tag{3}$$

where ν_0 equals the Keplerian orbital frequency at the innermost stable circular orbit around a non-rotating NS with gravitational mass M_0. This frequency can be expressed in the units of Hz as (e.g., Kluzniak & Wagoner, 1985; Kluzniak et al., 1990),

$$\nu_0 = \nu_{ISCO} = \frac{1}{6^{3/2}}\frac{c^3}{2\pi G}\,\frac{1}{M} = 2198\,\frac{M_\odot}{M} = 2198\,\frac{1}{\mathcal{M}}. \tag{4}$$

For $\mathcal{B} = 1$, relation (3) merges with the frequency relation implied by the RP model while the CT model prediction is well approximated by relation (3) for $\mathcal{B} = 0.8$. We illustrate this property of relation (3) in Figure 1b.

4. Data matching - main results

For 9 sources, namely 4U 1608-52, 4U 1636-53, 4U 1735-44, 4U 1915-05, IGR J17191-2821, GX 17+2, Sco X-1, Cir X-1 and XTE J1807.4-294 we find good agreement between the CT model and data. In all these sources the CT model

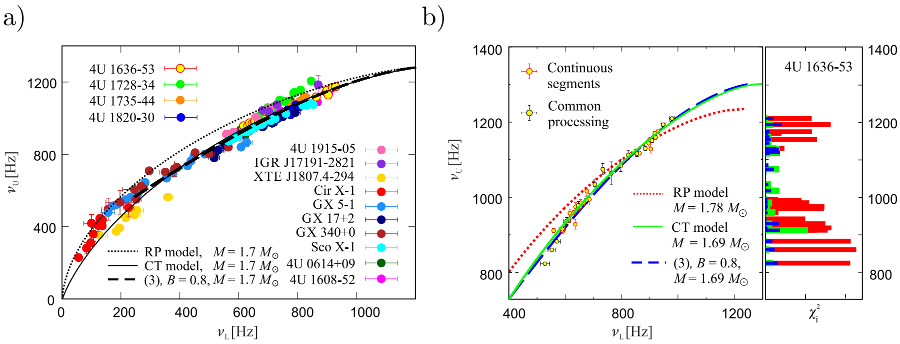

Figure 1. Correlations between the frequencies of twin-peak QPOs. a) The data of 14 sources and examples of the expected frequency relations. Detailed information on the individual sources along with the appropriate references is given in Table 1. b) The data of the atoll source 4U 1636-53 and their best fits. For the sake of clarity, the data-set which corresponds to the individual continuous observations is compared to the data-set associated with the common processing of all observations (see Török et al., 2016a). In both panels the expected frequency relations are drawn for a non-rotating NS.

matches the observed trend better than is done by the RP model (see Figure 2). For the other 5 sources, namely 4U 1728-34, 4U 0614+09, 4U 1820-30, GX 340+0 and GX 5-1, it is not possible to match the data due to the CT model limitations discussed by Török et al. (2016a).

Relation (3) well describes the data in each of the 14 sources (see Table 1). In some cases one does not achieve $\chi^2 \approx 1$d.o.f, but no clear deviation of data from the expected trend is found. This can be seen from a direct comparison between the expected curves and data, which is for each source included in Török et al. (2017a,b) where we present detailed results.

5. Consideration of models of rotating NSs

In the series of works (Török et al., 2010, 2012, 2016b) the authors explored the implications of several orbital QPO models. They found that the estimation of NS parameters based on these models leads to the effective degeneracy of these parameters. For a given model, each combination of NS mass M, angular momentum j and quadrupole moment q corresponds to a certain value of a single generalized parameter, e.g., non-rotating NS mass. Indeed, Török et al. (2016a) noticed that the NS mass implied by the CT model for the atoll source 4U 1636-53 can be expressed as

$$M = M_0[1 + 0.7(j + j^2)], \quad M_0 = 1.69^{\pm 0.01} M_\odot \,. \tag{5}$$

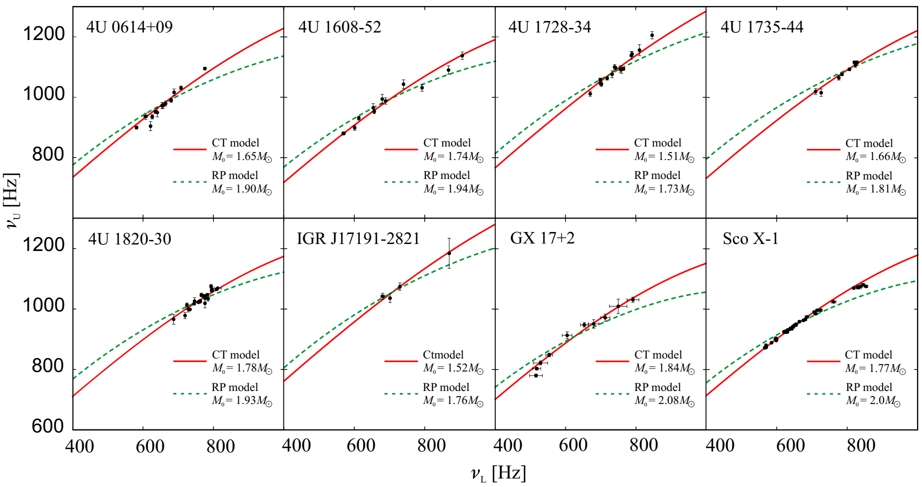

Figure 2. A comparison between the best fits obtained assuming the CT and RP models for data of the individual sources. The best fits for the atoll source 4U 1636-53 are shown in Figure 1b.

5.1. Neutron star spin, radius and equation of state

There is good evidence on the NS spin frequency of 4U 1636–53 based on the X-ray burst measurements (see the reference in Wang et al., 2017). The consideration of the X-ray burst models implies the NS spin to take the value of $\nu_S \doteq 580\,\mathrm{Hz}$. The CT model predictions can therefore be compared to the expectations given by models of rotating NSs.

Figure 3a (after Török et al., 2016a) displays several mass-angular momentum relations expected from the models of rotating NSs for the spin of 580 Hz. Inspecting this Figure one can see that there is an overlap between the relations given by the models of rotating NSs and the relation inferred from the CT model. The required NS mass is $M(580\mathrm{Hz}) \approx 2M_\odot$.

Considering the above result, one can expect that similar consideration should also be valid for the other sources listed in Table 1. This is justified in Figure 3b, where we explore the CT model predictions for another atoll source, 4U 1608-52. Table 1 indicates that $\mathcal{M}(\mathcal{B} = 0.8) = 1.74$. The NS spin inferred from the X-ray burst measurements takes the value of $\nu_S \doteq 610\,\mathrm{Hz}$ (see references in Wang et al., 2017). Analyzing Figure 3b one can see that the relation

$$M = M_0[1 + 0.6(j + j^2)], \quad M_0 = 1.74^{\pm 0.01} M_\odot \tag{6}$$

describes the CT model model prediction and overlaps with the relations given by the models of rotating NSs around $M(610\mathrm{Hz}) \approx 2.1M_\odot$.

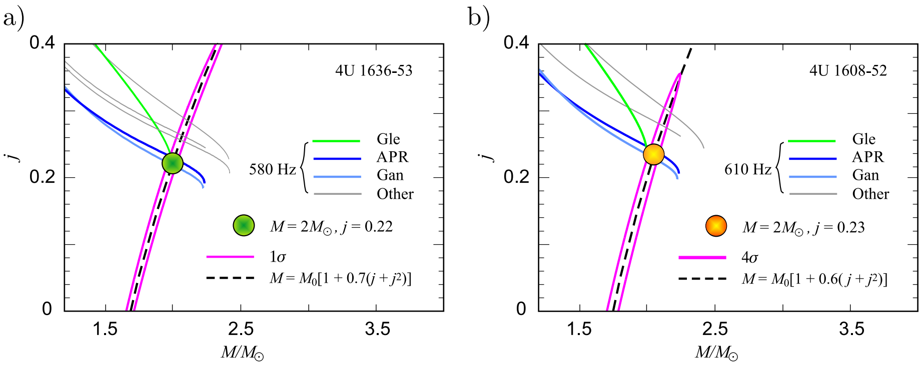

Figure 3. The mass-angular momentum contours obtained from the fitting of datapoints using the CT model vs. the mass-angular momentum relations predicted by models of rotating NSs. These are drawn for several NS EoS and the values of spin inferred from the X-ray burst measurements. For the models of rotating NSs we adopt the approach of Urbanec et al. (2013). The assumed EoS are as follows. Gle - Glendenning (1985); APR - Akmal et al. (1998); Gan - Gandolfi et al. (2010); other - Rikovska Stone et al. (2003); Urbanec et al. (2010). For the QPO model, the σ-confidence levels are calculated in accordance with the method used in Török et al. (2016a,b). a) The atoll source 4U 1636-53. b) The atoll source 4U 1608-52. In both panels the emphasized spot indicates where the QPO model and the EoS relations overlap.

6. Conclusions

The CT model as well as relation (3) for $\mathcal{B} = 0.8$ well reproduce the data of 9 sources. Assuming $\mathcal{B}$ as a free parameter, we obtain good fits for each of the 14 considered sources. We suggest that larger deviations from the case of $\mathcal{B} = 0.8$ are caused by further non-geodesic effects acting on the torus formation. These can be induced by the influence of magnetic field.

The particular consideration of the CT model agrees with the general interpretation, in which the $\mathcal{M}$ parameter represents the main parameter reflecting the spacetime geometry given by the NS mass and spin, while the $\mathcal{B}$ parameter reflects the additional stable factors. Further determination of NS mass and spin is possible when implications of relation (3) are confronted with the results of NS modeling based on NS spin measurements. In the case of the CT model we have already obtained promising results in this research direction.

Acknowledgements.

We would like to acknowledge the Czech Science Foundation grant No. 17-16287S, the internal SU grant No. SGS/15/2016, and the INTER-TRANSFER project No. LTT17003. We are grateful to Marek Abramowicz and Omer Blaes for useful discussions. Last but not least, we would like to acknowledge the hospitality of University of

Table 1. The results of data matching for relation (3) assuming $\mathcal{B} = 0.8$ and $\mathcal{B}$ as a free parameter. The goodness of fits is formally characterized by the χ^2 values. The uncertainties displayed here correspond to standard errors.

Source No./Type	Name	$\mathcal{M}(0.8)$	$\frac{\chi^2}{d.o.f.}$	$\mathcal{M}(\mathcal{B})$	$\mathcal{B}$	$\frac{\chi^2_{\mathcal{M}(\mathcal{B})}}{d.o.f.}$	Data-points
1/A	4U 1608-52	$1.80^{\pm0.01}$	1.6	$1.79^{\pm0.04}$	$0.79^{\pm0.03}$	1.7	12
2/A	4U 1636-53	$1.70^{\pm0.01}$	2.0	$1.70^{\pm0.01}$	$0.8^{\pm0.01}$	2.1	22
3/A	4U 1735-44	$1.69^{\pm0.01}$	2.1	$1.48^{\pm0.10}$	$0.61^{\pm0.06}$	1.0	8
4/A	4U 1915-05	$1.58^{\pm0.03}$	0.8	$1.65^{\pm0.03}$	$0.82^{\pm0.01}$	0.2	5
5/A	IGR J17191	$1.58^{\pm0.02}$	0.6	$1.63^{\pm0.20}$	$0.85^{\pm0.2}$	0.8	4
6/Z	GX 17+2	$1.89^{\pm0.02}$	1.2	$1.77^{\pm0.07}$	$0.72^{\pm0.04}$	0.8	10
7/Z	Sco X-1	$1.82^{\pm0.01}$	1.0	$1.81^{\pm0.01}$	$0.8^{\pm0.01}$	1.0	39
8/Z	Cir X-1	$0.74^{\pm0.10}$	1.2	$1.42^{\pm0.5}$	$0.89^{\pm0.06}$	1.1	11
9/P	XTE J1807.4	$2.61^{\pm0.11}$	0.8	$2.85^{\pm0.25}$	$0.86^{\pm0.07}$	0.8	7
10/A	4U 1728-34	$1.57^{\pm0.01}$	3.2	$1.35^{\pm0.12}$	$0.65^{\pm0.06}$	2.5	15
11/A	4U 0614+09	$1.71^{\pm0.02}$	5.1	$1.39^{\pm0.06}$	$0.62^{\pm0.02}$	1.1	13
12/A	4U 1820-30	$1.81^{\pm0.01}$	9.3	$1.53^{\pm0.07}$	$0.58^{\pm0.03}$	3.2	23
13/Z	GX 340+0	$1.62^{\pm0.08}$	4.2	$2.23^{\pm0.10}$	$1.10^{\pm0.08}$	1.6	12
14/Z	GX 5-1	$1.65^{\pm0.10}$	16.7	$2.31^{\pm0.04}$	$1.11^{\pm0.02}$	1.5	21

Source type: A - Atoll, Z - Z, P - Pulsar

References: (1)–(3), (10) – (12) - Barret et al. (2005b,c, 2006), (4) - Boirin et al. (2000), (5) - Altamirano et al. (2010), (6) - Homan et al. (2002), (7) - van der Klis et al. (1997), (8) - Boutloukos et al. (2006), (9) - Linares et al. (2005), (13) - Jonker et al. (2000), (14) - Jonker et al. (2002).

California in Santa Barbara, and to express our thanks to concierges of Mlýnská hotel in Uherské Hradiště, Czech Republic for their participation in organizing frequent workshops of Silesian University and Astronomical Institute of the Czech Academy of Sciences.

References

Abramowicz, M. A., Blaes, O. M., Horák, J., Kluźniak, W., & Rebusco, P., Epicyclic oscillations of fluid bodies: II. Strong gravity. 2006, *Classical and Quantum Gravity*, **23**, 1689, DOI: 10.1088/0264-9381/23/5/014

Abramowicz, M. A., Horák, J., & Kluzniak, W., Modulation of the Neutron Star Boundary Layer Luminosity by Disk Oscillations. 2007, *Acta Astron.*, **57**, 1

Abramowicz, M. A., Karas, V., Kluźniak, W., Lee, W. H., & Rebusco, P., Non-Linear Resonance in Nearly Geodesic Motion in Low-Mass X-Ray Binaries. 2003, *PASJ*, **55**, 467, DOI: 10.1093/pasj/55.2.467

Abramowicz, M. A. & Kluźniak, W., A precise determination of black hole spin in GRO J1655-40. 2001, *A&A*, **374**, L19, DOI: 10.1051/0004-6361:20010791

Akmal, A., Pandharipande, V. R., & Ravenhall, D. G., Equation of state of nucleon matter and neutron star structure. 1998, *Phys. Rev. C*, **58**, 1804, DOI: 10.1103/PhysRevC.58.1804

Alpar, M. A. & Shaham, J., Is GX5 - 1 a millisecond pulsar? 1985, *Nature*, **316**, 239, DOI: 10.1038/316239a0

Altamirano, D., Linares, M., Patruno, A., et al., Type I X-ray bursts, burst oscillations and kHz quasi-periodic oscillations in the neutron star system IGRJ17191-2821. 2010, *MNRAS*, **401**, 223, DOI: 10.1111/j.1365-2966.2009.15627.x

Bachetti, M., Romanova, M. M., Kulkarni, A., Burderi, L., & di Salvo, T., QPO emission from moving hot spots on the surface of neutron stars: a model. 2010, *MNRAS*, **403**, 1193, DOI: 10.1111/j.1365-2966.2010.16203.x

Barret, D., Kluźniak, W., Olive, J. F., Paltani, S., & Skinner, G. K., On the high coherence of kHz quasi-periodic oscillations. 2005a, *Mon. Not. R. Astron. Soc.*, **357**, 1288, DOI: 10.1111/j.1365-2966.2005.08734.x

Barret, D., Olive, J.-F., & Miller, M. C., An abrupt drop in the coherence of the lower kHz quasi-periodic oscillations in 4U 1636-536. 2005b, *MNRAS*, **361**, 855, DOI: 10.1111/j.1365-2966.2005.09214.x

Barret, D., Olive, J.-F., & Miller, M. C., Drop of coherence of the lower kilo-Hz QPO in neutron stars: Is there a link with the innermost stable circular orbit? 2005c, *Astronomische Nachrichten*, **326**, 808, DOI: 10.1002/asna.200510417

Barret, D., Olive, J.-F., & Miller, M. C., The coherence of kilohertz quasi-periodic oscillations in the X-rays from accreting neutron stars. 2006, *MNRAS*, **370**, 1140, DOI: 10.1111/j.1365-2966.2006.10571.x

Barret, D. & Vaughan, S., Maximum Likelihood Fitting of X-Ray Power Density Spectra: Application to High-frequency Quasi-periodic Oscillations from the Neutron Star X-Ray Binary 4U1608-522. 2012, *AJ*, **746**, 131, DOI: 10.1088/0004-637X/746/2/131

Belloni, T., Méndez, M., & Homan, J., On the kHz QPO frequency correlations in bright neutron star X-ray binaries. 2007, *Mon. Not. R. Astron. Soc.*, **376**, 1133, DOI: 10.1111/j.1365-2966.2007.11486.x

Blaes, O. M., Arras, P., & Fragile, P. C., Oscillation modes of relativistic slender tori. 2006, *MNRAS*, **369**, 1235, DOI: 10.1111/j.1365-2966.2006.10370.x

Boirin, L., Barret, D., Olive, J. F., Bloser, P. F., & Grindlay, J. E., Low and high frequency quasi-periodic oscillations in 4U1915-05. 2000, *Astronomy and Astrophysics*, **361**, 121

Boutloukos, S., van der Klis, M., Altamirano, D., et al., Discovery of Twin kHz QPOs in the Peculiar X-Ray Binary Circinus X-1. 2006, *APJ*, **653**, 1435, DOI: 10.1086/508934

Bradt, H. V., Rothschild, R. E., & Swank, J. H., X-ray timing explorer mission. 1993, *ApJ Supp.*, **97**, 355

Bursa, M., High-frequency QPOs in GRO J1655-40: Constraints on resonance models by spectral fits. 2005, in *RAGtime 6/7: Workshops on black holes and neutron stars*, ed. S. Hledík & Z. Stuchlík, 39–45

de Avellar, M. G., Porth, O., Younsi, Z., & Rezzolla, L., The kilo Hertz quasi-periodic oscillations in neutron star low-mass X-ray binaries as tori oscillation modes. I. 2017, *ArXiv e-prints* [arXiv: 1709.07706]

Dönmez, O., Zanotti, O., & Rezzolla, L., On the development of quasi-periodic oscillations in Bondi-Hoyle accretion flows. 2011, *Mon. Not. R. Astron. Soc.*, **412**, 1659, DOI: 10.1111/j.1365-2966.2010.18003.x

Fragile, P. C., Straub, O., & Blaes, O., High-frequency and type-C QPOs from oscillating, precessing hot, thick flow. 2016, *MNRAS*, **461**, 1356, DOI: 10.1093/mnras/stw1428

Gandolfi, S., Illarionov, A. Y., Fantoni, S., et al., Microscopic calculation of the equation of state of nuclear matter and neutron star structure. 2010, *MNRAS*, **404**, L35, DOI: 10.1111/j.1745-3933.2010.00829.x

Germanà, C., Upper-twin-peak quasiperiodic oscillation in x-ray binaries and the energy from tidal circularization of relativistic orbits. 2017, *ArXiv e-prints* [arXiv: 1711.01626]

Glendenning, N. K., Neutron stars are giant hypernuclei? 1985, *ApJ*, **293**, 470, DOI: 10.1086/163253

Homan, J., van der Klis, M., Jonker, P. G., et al., RXTE Observations of the Neutron Star Low-Mass X-Ray Binary GX 17+2: Correlated X-Ray Spectral and Timing Behavior. 2002, *The Astrophysical Journal*, **568**, 878, DOI: 10.1086/339057

Horák, J., A possible mechanism for QPOs modulation in neutron star sources. 2005, *Astronomische Nachrichten*, **326**, 845, DOI: 10.1002/asna.200510425

Huang, C.-Y., Ye, Y.-C., Wang, D.-X., & Li, Y., A model for 3:2 HFQPO pairs in black hole binaries based on cosmic battery. 2016, *Mon. Not. R. Astron. Soc.*, **457**, 3859, DOI: 10.1093/mnras/stw226

Ingram, A. & Done, C., A physical interpretation of the variability power spectral components in accreting neutron stars. 2010, *MNRAS*, **405**, 2447, DOI: 10.1111/j.1365-2966.2010.16614.x

Jahoda, K., Swank, J. H., Giles, A. B., et al., In-orbit performance and calibration of the Rossi X-ray Timing Explorer (RXTE) Proportional Counter Array (PCA). 1996, in Proc. SPIE, Vol. **2808**, *EUV, X-Ray, and Gamma-Ray Instrumentation for Astronomy VII*, ed. O. H. Siegmund & M. A. Gummin, 59–70

Jonker, P. G., van der Klis, M., Homan, J., et al., Low- and high-frequency variability as a function of spectral properties in the bright X-ray binary GX 5-1. 2002, *MNRAS*, **333**, 665, DOI: 10.1046/j.1365-8711.2002.05442.x

Jonker, P. G., van der Klis, M., Wijnands, R., et al., The Power Spectral Properties of the Z Source GX 340+0. 2000, *The Astrophysical Journal*, **537**, 374, DOI: 10.1086/309029

Kato, S., Basic Properties of Thin-Disk Oscillations. 2001, *PASJ*, **53**, 1, DOI: 10.1093/pasj/53.1.1

Kluźniak, W. & Abramowicz, M. A., The physics of kHz QPOs—strong gravity's coupled anharmonic oscillators. 2001, *ArXiv Astrophysics e-prints* [arXiv: astro-ph/0105057]

Kluźniak, W., Abramowicz, M. A., Kato, S., Lee, W. H., & Stergioulas, N., Nonlinear Resonance in the Accretion Disk of a Millisecond Pulsar. 2004, *AJ*, **603**, L89, DOI: 10.1086/383143

Kluzniak, W., Michelson, P., & Wagoner, R. V., Determining the properties of accretion-gap neutron stars. 1990, *ApJ*, **358**, 538, DOI: 10.1086/169006

Kluzniak, W. & Wagoner, R. V., Evolution of the innermost stable orbits around accreting neutron stars. 1985, *ApJ*, **297**, 548, DOI: 10.1086/163550

Lamb, F. K., Shibazaki, N., Alpar, M. A., & Shaham, J., Quasi-periodic oscillations in bright galactic-bulge X-ray sources. 1985, *Nature*, **317**, 681, DOI: 10.1038/317681a0

Le, T., Wood, K. S., Wolff, M. T., Becker, P. A., & Putney, J., Standing Shock Instability in Advection-dominated Accretion Flows. 2016, *Astrophys. J.*, **819**, 112, DOI: 10.3847/0004-637X/819/2/112

Lewin, W. H. G., van Paradijs, J., & van den Heuvel, E. P. J. 1997, *X-ray Binaries* (Cambridge University Press), 674

Lin, Y.-F., Boutelier, M., Barret, D., & Zhang, S.-N., Studying Frequency Relationships of Kilohertz Quasi-periodic Oscillations for 4U 1636-53 and Sco X-1: Observations Confront Theories. 2011, *The Astrophysical Journal*, **726**, 74, DOI: 10.1088/0004-637X/726/2/74

Linares, M., van der Klis, M., Altamirano, D., & Markwardt, C. B., Discovery of Kilohertz Quasi-periodic Oscillations and Shifted Frequency Correlations in the Accreting Millisecond Pulsar XTE J1807-294. 2005, *The Astrophysical Journal*, **634**, 1250, DOI: 10.1086/497025

Méndez, M., On the maximum amplitude and coherence of the kilohertz quasi-periodic oscillations in low-mass X-ray binaries. 2006, *MNRAS*, **371**, 1925, DOI: 10.1111/j.1365-2966.2006.10830.x

Miller, M. C., Lamb, F. K., & Psaltis, D., Sonic-Point Model of Kilohertz Quasi-periodic Brightness Oscillations in Low-Mass X-Ray Binaries. 1998, *AJ*, **508**, 791, DOI: 10.1086/306408

Mishra, B., Vincent, F. H., Manousakis, A., et al., Quasi-periodic oscillations from relativistic ray-traced hydrodynamical tori. 2017, *MNRAS*, **467**, 4036, DOI: 10.1093/mnras/stx299

Morsink, S. M. & Stella, L., Relativistic Precession around Rotating Neutron Stars: Effects Due to Frame Dragging and Stellar Oblateness. 1999, *ApJ*, **513**, 827, DOI: 10.1086/306876

Mukhopadhyay, B., Higher-Order Nonlinearity in Accretion Disks: Quasi-Periodic Oscillations of Black Hole and Neutron Star Sources and Their Spin. 2009, *AJ*, **694**, 387, DOI: 10.1088/0004-637X/694/1/387

Paczynski, B., Possible relation between the X-ray QPO phenomenon and general relativity. 1987, *Nature*, **327**, 303, DOI: 10.1038/327303a0

Parthasarathy, V., Kluzniak, W., & Cemeljic, M., MHD simulations of oscillating cusp-filling tori around neutron stars – missing upper kHz QPO. 2017, *ArXiv e-prints* [arXiv: 1703.05036]

Pétri, J., An explanation for the kHz-QPO twin peaks separation in slow and fast rotators. 2005, *A&A*, **439**, L27, DOI: 10.1051/0004-6361:200500151

Psaltis, D., Wijnands, R., Homan, J., et al., On the Magnetospheric Beat-Frequency and Lense-Thirring Interpretations of the Horizontal-Branch Oscillation in the Z Sources. 1999, *AJ*, **520**, 763, DOI: 10.1086/307460

Rezzolla, L., Yoshida, S., & Zanotti, O., Oscillations of vertically integrated relativistic tori - I. Axisymmetric modes in a Schwarzschild space-time. 2003, *MNRAS*, **344**, 978, DOI: 10.1046/j.1365-8711.2003.07023.x

Rikovska Stone, J., Miller, J. C., Koncewicz, R., Stevenson, P. D., & Strayer, M. R., Nuclear matter and neutron-star properties calculated with the Skyrme interaction. 2003, *Phys. Rev. C*, **68**, 034324, DOI: 10.1103/PhysRevC.68.034324

Šrámková, E., Torkelsson, U., & Abramowicz, M. A., Oscillations of tori in the pseudo-Newtonian potential. 2007, *A&A*, **467**, 641, DOI: 10.1051/0004-6361:20065979

Stella, L. & Vietri, M., Lense-Thirring Precession and Quasi-periodic Oscillations in Low-Mass X-Ray Binaries. 1998, *ApJ lett.*, **492**, L59, DOI: 10.1086/311075

Stella, L. & Vietri, M., kHz Quasiperiodic Oscillations in Low-Mass X-Ray Binaries as Probes of General Relativity in the Strong-Field Regime. 1999, *Phys. Rev. Lett.*, **82**, 17, DOI: 10.1103/PhysRevLett.82.17

Stella, L. & Vietri, M., Quasi-Periodic Oscillations from Low-Mass X-ray Binaries and Strong Field Gravity. 2001, in Astronomical Society of the Pacific Conference Series, Vol. **234**, *X-ray Astronomy 2000*, ed. R. Giacconi, S. Serio, & L. Stella, 213

Straub, O. & Šrámková, E., Epicyclic oscillations of non-slender fluid tori around Kerr black holes. 2009, *Classical and Quantum Gravity*, **26**, 055011, DOI: 10.1088/0264-9381/26/5/055011

Stuchlík, Z. & Kološ, M., String loops oscillating in the field of Kerr black holes as a possible explanation of twin high-frequency quasiperiodic oscillations observed in microquasars. 2014, *Phys. Rev. D*, **89**, 065007, DOI: 10.1103/PhysRevD.89.065007

Stuchlík, Z., Kotrlová, A., & Török, G., Multi-resonance orbital model of high-frequency quasi-periodic oscillations: possible high-precision determination of black hole and neutron star spin. 2013, *A&A*, **552**, A10, DOI: 10.1051/0004-6361/201219724

Titarchuk, L. & Wood, K., On the Low and High Frequency Correlation in Quasi-periodic Oscillations among White Dwarf, Neutron Star, and Black Hole Binaries. 2002, *AJ*, **577**, L23, DOI: 10.1086/344147

Török, G., Bakala, P., Šrámková, E., Stuchlík, Z., & Urbanec, M., On Mass Constraints Implied by the Relativistic Precession Model of Twin-peak Quasi-periodic Oscillations in Circinus X-1. 2010, *AJ*, **714**, 748, DOI: 10.1088/0004-637X/714/1/748

Török, G., Bakala, P., Šrámková, E., et al., Mass-Angular-momentum Relations Implied by Models of Twin Peak Quasi-periodic Oscillations. 2012, *ApJ*, **760**, 138, DOI: 10.1088/0004-637X/760/2/138

Török, G., Goluchová, K., Horák, J., et al., Twin peak quasi-periodic oscillations as signature of oscillating cusp torus. 2016a, *MNRAS*, **457**, L19, DOI: 10.1093/mnrasl/slv196

Török, G., Goluchová, K., Urbanec, M., et al., Constraining Models of Twin-Peak Quasi-periodic Oscillations with Realistic Neutron Star Equations of State. 2016b, *The Astrophysical Journal*, **833**, 273, DOI: 10.3847/1538-4357/833/2/273

Török, G., Goluchová, K., Šrámková, E., et al., On one-parametric formula relating the frequencies of twin-peak quasi-periodic oscillations. 2017a, *ArXiv e-prints* [arXiv: 1710.10901], accepted for publication in MNRAS

Török, G., Goluchová, K., Šrámková, E., et al., A one-parametric formula relating the frequencies of twin-peak quasi-periodic oscillations. 2017b, in *RAGtime 17, 18, 19: Workshops on black holes and neutron stars*

Urbanec, M., Běták, E., & Stuchlík, Z., Observational Tests of Neutron Star Relativistic Mean Field Equations of State. 2010, *Acta Astron.*, **60**, 149

Urbanec, M., Miller, J. C., & Stuchlík, Z., Quadrupole moments of rotating neutron stars and strange stars. 2013, *MNRAS*, **433**, 1903, DOI: 10.1093/mnras/stt858

Čadež, A., Calvani, M., & Kostić, U., On the tidal evolution of the orbits of low-mass satellites around black holes. 2008, *A&A*, **487**, 527, DOI: 10.1051/0004-6361:200809483

van der Klis, M. 2006, *Rapid X-ray Variability* (Cambridge University Press), 39–112

van der Klis, M., Wijnands, R. A. D., Horne, K., & Chen, W., Kilohertz Quasi-Periodic Oscillation Peak Separation Is Not Constant in Scorpius X-1. 1997, *APJL*, **481**, L97, DOI: 10.1086/310656

Wagoner, R. V., Silbergleit, A. S., & Ortega-Rodríguez, M., "Stable" Quasi-periodic Oscillations and Black Hole Properties from Diskoseismology. 2001, *AJ*, **559**, L25, DOI: 10.1086/323655

Wang, D.-H., Zhang, C.-M., Qu, J.-L., & Yang, Y.-Y., Correlations between the frequencies of twin kHz QPOs and spins of neutron stars in LMXBs. 2017, *ArXiv e-prints* [arXiv: 1710.09128]

Wang, D.-X., Gan, Z.-M., Huang, C.-Y., & Li, Y., Association of the 3:2 HFQPO pairs with the broad Fe K line in XTE J1550-564 and GRO J1655-40. 2008, *Mon. Not. R. Astron. Soc.*, **391**, 1332, DOI: 10.1111/j.1365-2966.2008.13965.x

Zhang, C., The MHD Alfven wave oscillation model of kHz Quasi Periodic Oscillations of Accreting X-ray binaries. 2004, *A&A*, **423**, 401, DOI: 10.1051/0004-6361:20035808

Contrib. Astron. Obs. Skalnaté Pleso **48**, 488 – 497, (2018)

Study of multiple layers coatings for X–ray mirrors

V. Stehlikova[1,2], **A.-C. Probst**[3], **O. Nentvich**[1], **M. Urban**[1], **L. Sieger**[1], **T. Döhring**[3] and **R. Hudec**[1]

[1] *Czech Technical University in Prague,*
Technicka 2, Prague 166 27, Czech Republic
(E-mail: veronika.stehlikova@fel.cvut.cz)
[2] *Max-Planck-Institut für extraterrestrische Physik, Garching, Germany*
[3] *Aschaffenburg University of Applied Sciences,*
Würzburger Straße 45, 63743 Aschaffenburg, Germany

Received: December 22, 2017; Accepted: February 28, 2018

Abstract. This paper focuses on a theoretical background that motivated the experimental campaign of multiple layer coatings of X-ray mirrors, and the first results of the testing of the prepared samples. Simulations of the use of different overcoats were performed in order to improve the reflectivity of thin iridium coatings designed for X-ray optics effective in the energy up to 10 keV. Samples based on these simulations were prepared and are being tested for the properties that influence the X-ray optical performance, such as layer homogeneity, density and surface micro-roughness. Further the topic of the coating stress was addressed, as it is an issue in case of thin, lightweight X-ray mirrors and affects the time stability of layers. The discussion and preliminary results conclude our contribution.

Key words: X-ray optics – multiple coating layers – X-ray reflectivity

1. Introduction

Coating layers used for producing X-ray reflective surfaces are usually made of heavy metals like gold and iridium and the thickness of these layers varies from tens to hundreds of nanometres (Kolodziejczak et al., 2000). These layers grant the reflectivity of X-ray mirrors in desired energy range which the mirror is designed for and their quality directly affects the effectivity of the optics (Stehlikova et al., 2017).

The quality of the coating can be evaluated from two different points of view. The first is the qualitative rating of the coating material. Here can be assessed the reflectivity of the selected material, the effectivity of reflection in dependence on the incident angle or the reactivity with the environment during the process of layer deposition. The second examines the properties of the prepared layer. Here are evaluated features like adhesivity between the reflective layer and carrying substrate, microroughness achievable using actual deposition methods and stress in the layers, which can affect the time stability of coatings and others (Döhring et al., 2017).

Next chapters describe theoretical study of coatings dedicated for a Lobster-eye type of X-ray optics (Schmidt, 1975; Hudec et al., 2015), with modified design which was already presented (Stehlikova et al., 2016). The main idea was to prepare a reflective layer suitable for relatively soft X-rays, up to 8 keV, 10 keV maximum. There were two real possibilities of layers production, to prepare a golden layer or to prepare an iridium layer. The iridium layers advantage is about 5 % better reflectivity in the energy range from 2.2 keV to 9 keV, the positive difference is ever rising at the higher energies. A disadvantage which is seen in this design was an energetic gap around 2 040 keV, corresponding to the electron binding energy of Fermi level M5. Here, the reflectivity of the material at the considered incident angle drops from about 90 % to about 10 % and then returns to 80 %, with not so prominent decreases at other Fermi levels (M4, M3, M2, M1; 2040.4 eV, 2116.1 eV, 2550.7 eV, 2908.7 eV, 3173.7 eV respectively).

2. Simulations

Following figures are the result of simulations, prepared as a template for an integrated testing set of multiple layers coatings on silicon. Materials of the layers were chosen according to the previous tests and are reflecting the already acquired experiences. The thicknesses of each layer are chosen according to two main parameters. The first is minimal thickness, which is needed to get a full-reflective layer avoiding energetic transmission into substrate. The second is the influence of thickness on microroughness and energy losses in the layers. Another restriction lies in the used equipment.

The apparatus which has been used to produce samples for real tests is able to work with two targets at once (Probst et al., 2017b). Thus, during changing between two materials there is no need to open the chamber and flood it with air. Layers prepared by this procedure are not threatened by oxidation, which could cause material degradation and generation of indefinable interlayers. Disadvantage is that the chamber has only two targets, so the combinations of layers are strongly limited. The simulations work with the following parameters:

- materials of layers and substrates
- roughness of the surface
- density and thickness of the layer
- energy of incident rays and the angle of incident

2.1. Materials

The materials for planned experiments are chromium and iridium, the substrate for the mirrors is a silicon wafer. Other assessed materials were gold and aluminium. The reasons of the final choice are described below.

According to previous studies, an iridium layer sputtered on super-polished silicon does not have adequate adhesivity. Because of internal stress in the layer and insufficient adhesivity between the layer and the substrate causes cracks and peeling off of the layers (Probst et al., 2017a; Broadway et al., 2015; Stehlikova et al., 2017).

To improve the adhesivity, an interlayer prepared of suitable element can be introduced between the substrate and the reflective layer. Previously, we have tested the interlayers based on aluminium and chromium. These elements have similar crystalline structure and adhesivity tests performed according to ISO2409 standard showed that both aluminium and chromium eliminate the peeling-off issue. Chromium was chosen as the inserted element because of its environmental stability which is generally better than of aluminium. As was mentioned above, when wanting to avoid the oxidation influence in between the coatings, only two targets can be mounted, so the chromium has to be used as the overlayer as well. At this moment, the better stability of chromium is beneficial.

2.2. Surface roughness

The parameter of surface microroughness has strong impact on the final reflectivity, because the wavelength of incident rays is similar to the mean value of microroughness and therefore the scattering effect causes strong energy losses. To get relevant results, RMS values measured on the samples of proper materials and thicknesses were used as a simulation input. Mean values got from these measurements are listed in Tab. 1. All the measurements were performed using atomic force microscope.

The samples which were used are listed bellow:

- a pure silicon wafer with crystallographic structure (1,0,0)
- the same grade silicon wafers with a 100 nm thick layer of chromium
- a 30 nm thick layer of iridium
- a 30 nm thick layer of gold

Traced general trend is rising microroughness with thickness, therefore closest values of tested thicknesses were chosen for test.

2.3. Layer thickness

Thickness of the layers depends on the factor of ideally zero transmission into the substrate for the reflective iridium layer and of stress compensation in the chromium-iridium bilayer. The stresses in iridium and chromium layers are inverse and to achieve the lowest possible stress level, the thickness ratio Cr:Ir is 3:1. (Ames et al., 2015).

Table 1. Table of different sputtered layers microroughnesses.

Surface type	RMS (nm)
Silicon substrate	0.17
Chromium	0.35
Iridium	0.50
Gold	0.38

There is the question of the chromium overlayer thickness as well. The iridium layer is the main reflective surface, and should be opaque for the X-rays in the whole judged range. Contrary to that, the overlayer, which has a better reflectivity at lower energies, should be transparent for the higher, to not limit the reflection at the main layer. According to the sputtering abilities of the machine, the thinnest layer with sufficient homogeneity in all the points is 4 nm.

2.4. Optical parameters of optics

All the material and layer parameters are closely associated with the optical design. X-ray mirrors are usually working with very small, flat incident angle of incoming rays. Rising angle causes, for example, deeper transmission of radiation into the surface layers. Although it has justification in a number of applications, in case of designed lobster eye optics the grazing angle has to be small - less than 0.5 degrees. The energy range of optics is designed for ranges up to 10 keV. Construction parameters are briefly listed in Tab. 2. One segment of planned multi-module optics can be seen in Fig. 1.

As relevant reflectivity limit was chosen 50 %. Even with improved optical design, which allows to focus more rays into the focal point, the ray still undergoes two reflections and that doubles the energy loss. Due to the general weakness of potential observation targets, less reflectivity is not worth.

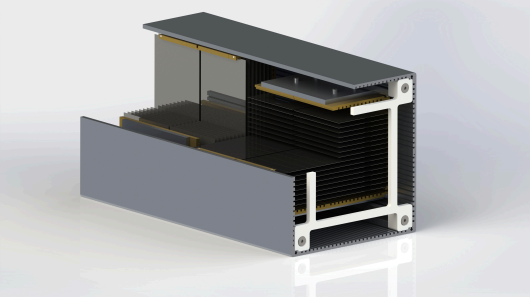

Figure 1. A visualization of lobster eye optical module.

Table 2. Table of basic optics parameters.

Number of mirrors	16
Number of sets	4
Mirror dimension	75 mm to 150 mm
Focal length	2.5 m
Gap between mirrors	6 mm
Thickness of mirror	0.75 mm

2.5. Simulations results and discussion

The simulations were performed for a series of combinations of thicknesses of adhesive layer, main reflective layer and the overlayer. The first problem was to compare the influence of different thicknesses on the absolute reflectivity of main reflecting layer. The comparison of 20 nm, 30 nm, 40 nm and 50 nm of iridium showed only marginal changes (<1%) in reflectivity at energy over 9 keV. The thickness of the adhesive layer was changed as well to ensure the reflectivity will not be changed by using chromium-iridium bilayer. As was expected if the simulation shows that the iridium layer behaves like the opaque one, the underlayer thickness does not have any effects. The risk of changing thickness of adhesive layer is based more on possible rising microroughness with thicker layers, which can then show up in the main layer.

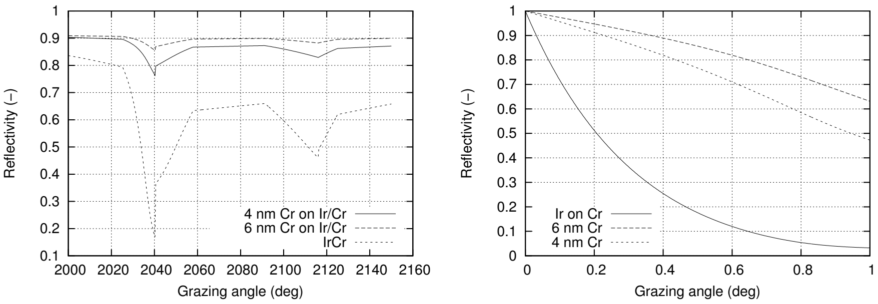

Figure 2. Detail of the energy gap at 2040 eV, where is clearly visible the improvement caused by usage of chromium overlayer (left figure); The dependence of reflectivity on the incident angle for the critical M5 energy. Angle value ranges from 0 to 1 deg, the layer is 4 or 6 nm thick chromium on 30 nm of iridium (right figure)

As was already mentioned, there was a possibility to choose between golden and iridium layer for the main reflective surface. The comparison of reflectivity is in Fig 3, where are shown iridium and golden layers of the same thickness (30 nm)

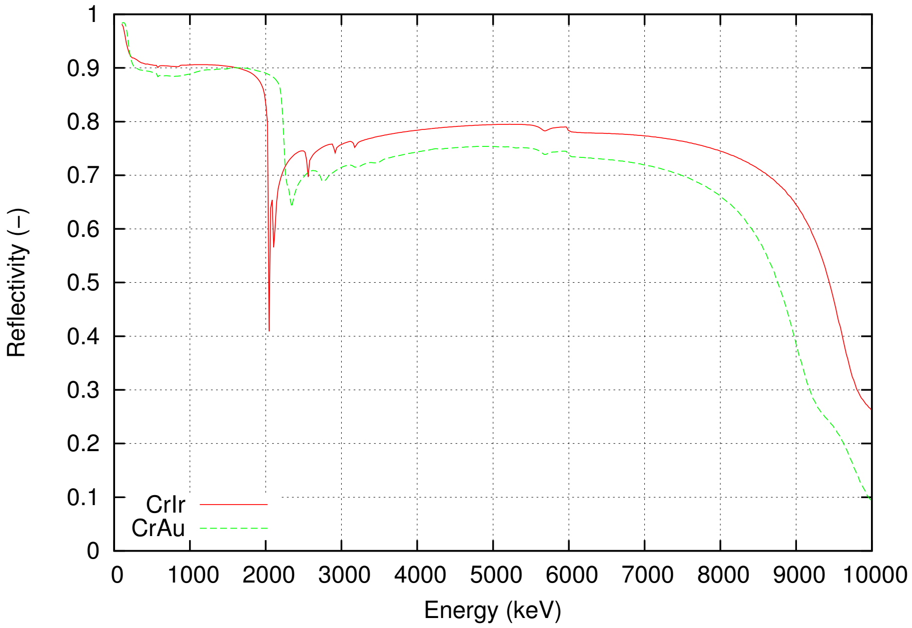

Figure 3. Difference between golden and iridium coating of the same thickness for incident angle 0.5 deg.

and on the same chromium underlayer (90 nm). The reflectivity of iridium is from 3 to 25 percent better in almost the whole scale with an exception of the energy gap at 2 040 eV. The region with reflectivity better than 50 % goes actually even 1 keV further into high energies.

The application of chromium overlayer is illustrated in Fig. 2. There is a detail of the energy gap around M5 for two thicknesses of overlayer and for two conditions; energy change in close surroundings (left figure) and influence of overlayer when changing incidence angle of incoming ray exactly at the binding energy (right figure). The effect of levelling the gaps is clearly visible, thicknesses 4 and 6 nm are accompanied by reference iridium-only surface.

The thickness of the overlayer was scaled from 2 nm to 8 nm. The effect on the reflectivity is antagonistic at low and at high energies. The border between these areas creates at 5 989 eV the K1 line, where the reflectivity of pure chrome layer drops under 10 %. Looking at the figure 4, the thickness of overlayer degrades the reflectivity of iridium equally, but the improvement in the softer rays is more exponential. Preparing of layer thicker than 6 nm seems meaningless, only degrading the high energy part; as ideal thickness for real experiments were chosen 5 nm and 6 nm.

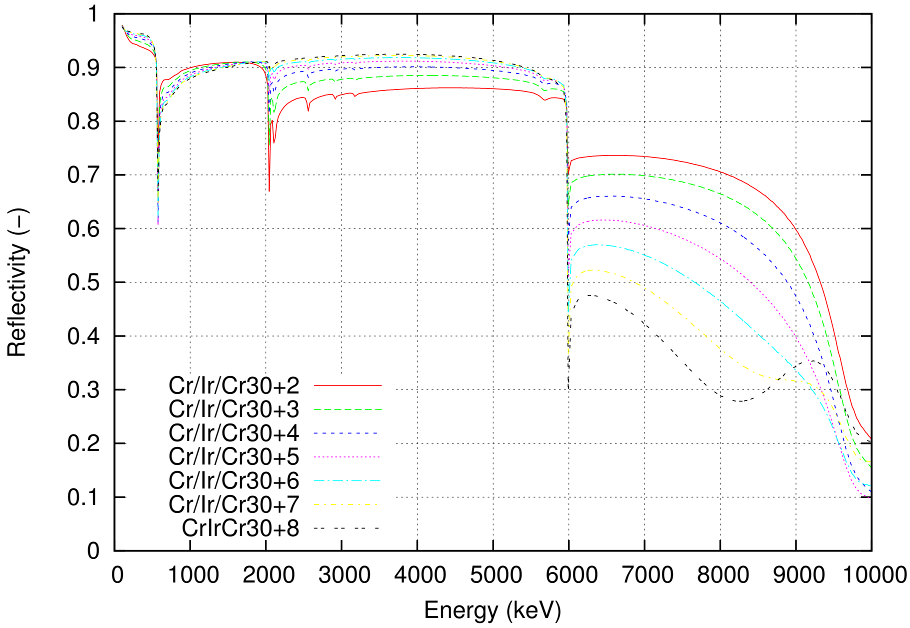

Figure 4. The 30 nm thick reflective iridium surface on 90 nm adhesive chromium interlayer, covered by different thickness (2 nm - 8 nm) chromium overcoating which improves the reflectivity of mirrors at lower energies

For better comparison between the chosen possibilities, there is Fig.2.5. The best compromise seems to be the combination of main iridium reflective layer and 5 nm thick chromium overlayer. It levels the gaps caused by iridium electron binding energies and concurrently does not cause too critical energy losses in the rest of studied energy range. It is necessary to count with not perfect homogeneity of the layers, which can cause fluctuations of layer thickness ±1 nm. Although this value is small, in the context of Fig. 4 is obvious that the effect is not negligible.

3. Real samples production

Based on the theoretical expectations, a series of samples with different layer ratios was produced for testing. To check the layer thickness of thicker layers (tests of 90 nm adhesive layers or main reflective layer) was used tactile stylus profiler Bruker DektakXT. For checking super-thin overlayers, an atomic force microscope (AFM) was used. The AFM was also used to check the microroughness of the surfaces.

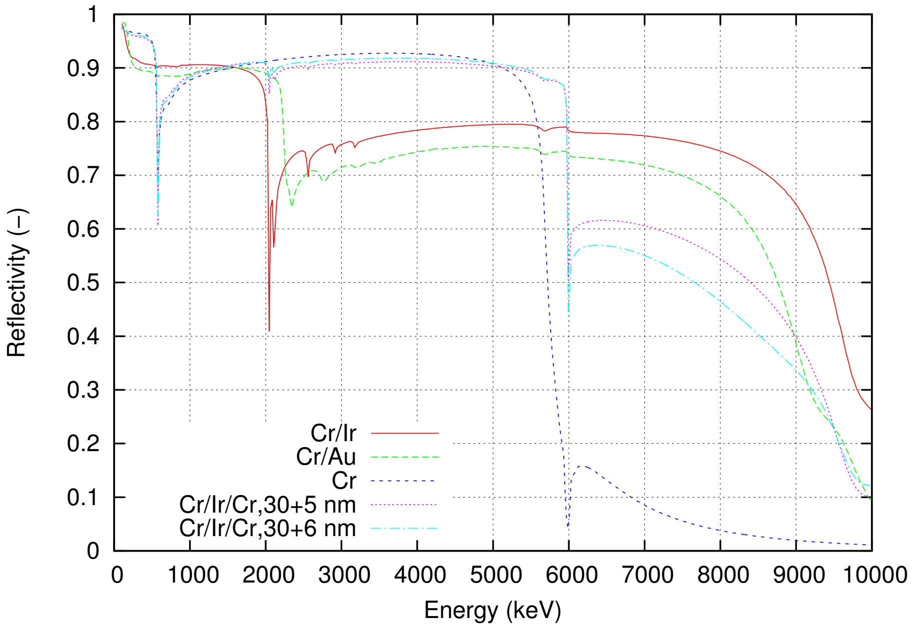

From the first tests ensues that with concurrent apparatus set-up it is possible to produce layers of expected homogeneity and thickness. Using variously shaped masks to prepare a measurable step, the fluctuation of the acquired thin chromium overlayers was ±0.11 nm. The AFM measurement of surface microroughness showed expected rising tendency in dependence on thickness. The difference between the worst and the best case for several tens of samples was 0.236 nm. Still, the most rough surface had RMS 0.408 nm, which value is under chosen 0.5 nm worst-case variant.

4. Conclusion

The paper presents a part of simulations performed to determine the best combination of two materials for future X-ray telescope dedicated for energy range between 1 and 8 keV. The simulation worked with the data and experiences acquired during last years activities. Based on them, input parameters of simulations were chosen to get relevant expectation of a multiple layer coatings behaviour.

According to the simulation results, the most promising coating variant for silicon X-ray mirrors is a configuration of layers silicone - adhesive chromium layer - main reflective iridium layer - levelling and protective chromium overlayer with thicknesses 1.75 mm - 90 nm - 30 nm - 5 nm.

So far were prepared several sets of samples with different combinations of the layers to prove the ability of preparing them with required accuracy. The preliminary results show good quality of surface microroughness which can significantly affect the resultant reflectivity of a mirror, as well as the capability of the sputtering apparatus to prepare very thin homogeneous layers.

Following tests in a vacuum tunnel should examine the X-ray reflectivity of prepared multiple layers to acquire results comparable with the theoretical simulation. If they will be corresponding, a full set of mirrors for the first lobster eye module is going to be produced.

Acknowledgements. All the technological steps result from a cooperation between Czech Technical University in Prague, University of Applied Sciences in Aschaffenburg and Rigaku Innovative Technologies, s.r.o. in Prague.

This work was supported by the Grant Agency of the Czech Technical University in Prague, grants No. SGS18/186/OHK3/3T/13 and SGS16/150/OHK3/2T/13, by Czech Republic Grant Agency No.13-33324S and also in the frame of the international JEUMICO project (Joint European Mirror Competence), which is funded by a Joint call of the Bavarian state ministry for education and culture, sciences and art in Germany and the Ministry of education, youth and sports of the Czech Republic.

References

Ames, A., Bruni, R., Cotroneo, V., et al., Using iridium films to compensate for piezoelectric materials processing stresses in adjustable x-ray optics. 2015, in Proc. SPIE, Vol. **9603**, *Society of Photo-Optical Instrumentation Engineers (SPIE) Conference Series*, 96031I

Broadway, D. M., Weimer, J., Gurgew, D., et al., Achieving zero stress in iridium, chromium, and nickel thin films. 2015, in Proc. SPIE, Vol. **9510**, *EUV and X-ray Optics: Synergy between Laboratory and Space IV*, 95100E

Döhring, T., Probst, A.-C., Emmerich, F., et al., Development of iridium coated x-ray mirrors for astronomical applications. 2017, in Society of Photo-Optical Instrumentation Engineers (SPIE) Conference Series, Vol. **10399**, *Society of Photo-Optical Instrumentation Engineers (SPIE) Conference Series*, 103991C

Hudec, R., Pina, L., Inneman, A., & Tichy, V., Applications of lobster eye optics. 2015, in Proc. SPIE, Vol. **9510**, *EUV and X-ray Optics: Synergy between Laboratory and Space IV*, 95100A

Kolodziejczak, J. J., Elsner, R. F., Austin, R. A., & O'Dell, S. L., Ion transmission to the focal plane of the Chandra X-Ray Observatory. 2000, in Proc. SPIE, Vol. **4140**, *X-Ray and Gamma-Ray Instrumentation for Astronomy XI*, ed. K. A. Flanagan & O. H. Siegmund, 135–143

Probst, A.-C., Stollenwerk, M., Emmerich, F., et al., Influence of sputtering pressure on the nanostructure and the X-ray reflectivity of iridium coatings. 2017a, *Surface and Coatings Technology*, DOI: 10.1016/j.surfcoat.2017.10.062

Probst, A.-C., Stollenwerk, M., Wen, M., Proserpio, L., & Döhring, T., Iridium coatings for space based x-ray optics. 2017b, in *International Conference on Space Optics 2016*, ed. N. Karafolas, B. Cugny, & Z. Sodnik (SPIE), 177

Schmidt, W. K. H., A proposed X-ray focusing device with wide field of view for use in X-ray astronomy. 1975, *Nuclear Instruments and Methods*, **127**, 285, DOI: 10.1016/0029-554X(75)90501-7

Stehlikova, V., Probst, A.-C., Nentvich, O., & Urban, M., Reflective coating layers for X-ray optics. 2016, in *AXRO conference 2016*

Stehlikova, V., Probst, A.-C., Nentvich, O., et al., Proceedings of 5th EOS Conference on Manufacturing of Optical Systems. 2017, in *Proceedings of 5th EOS Conference on Manufacturing of Optical Systems*

Contrib. Astron. Obs. Skalnaté Pleso **48**, 498 – 505, (2018)

The Wide Field Imager instrument for Athena

N. Meidinger
on behalf of the WFI proto-consortium

Max Planck Institute for Extraterrestrial Physics,
Giessenbachstrasse, 85748 Garching, Germany

Received: November 29, 2017; Accepted: January 20, 2018

Abstract. ESA's next large X-ray mission Athena will be equipped with two focal plane cameras, a Wide Field Imager (WFI) and an X-ray Integral Field Unit (X-IFU). The WFI instrument is designed for imaging and spectroscopy over a large field of view, and high count rate observations up to and beyond 1 Crab source intensity. Both cameras share alternately a mirror system based on silicon pore optics with a focal length of 12 m and an unprecedented large effective area. Main scientific requirements for WFI are described here and the corresponding conceptual design to meet them. The instrument employs active pixel sensors of DEPFET type, which are fully depleted, back-illuminated silicon devices of 450 µm thickness. In combination with front-end electronics ASICs tailored to the project, the resulting detectors provide high quantum efficiency over the 0.2 keV to 15 keV range with state-of-the art spectral resolution and extremely fast readout speeds compared to previous generations of Si detectors for X-ray astronomy. The focal plane comprises a Large Detector Array (LDA) with over 1 million pixel of 130 µm × 130 µm size, providing oversampling of the PSF by a factor > 2 over the 40 arcmin × 40 arcmin large field of view, complemented by a smaller Fast Detector (FD) optimized for high count rate applications.

Key words: Athena – Wide Field Imager – X-ray camera

1. WFI Overview and Requirements

The Athena mission had been proposed in 2013 by a large community of European X-ray astrophysicists (Nandra et al., 2013). Its scientific payload consists mainly of two focal plane cameras sharing alternately one mirror system based on silicon pore optics (Bavdaz et al., 2017). While the X-ray Integral Field Unit (X-IFU) permits high-resolution spectroscopy employing transition edge sensors operated at cryogenic temperatures, the Wide Field Imager (WFI) features a large field of view and high count rate capability by the use of novel active pixel sensors of DEPFET type (Meidinger et al., 2017a), (Treberspurg et al., 2017).

For these purposes, the WFI instrument comprises a large detector array (LDA) and a fast detector (FD) as shown in Fig. 1 (Meidinger et al., 2017b). Both shall perform spectroscopy of X-ray photons in the energy range from 0.2 keV to 15 keV. Energy resolutions of <80 eV and <170 eV FWHM are scientifically required for energies of 1 keV and 7 keV respectively, over the

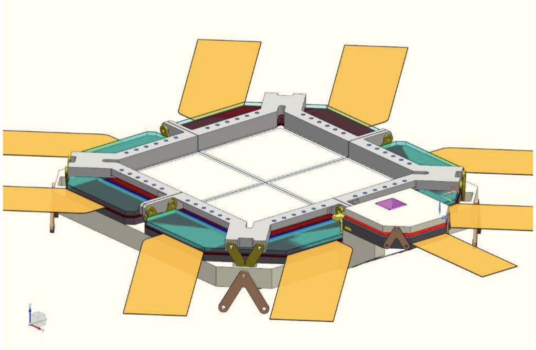

Figure 1. WFI detectors: the LDA with the four large-area quadrants, each with two flexible leads, and the small FD in the front right-hand corner of the image.

field of view and until end of life. The LDA spans the large field of view of 40 arcmin × 40 arcmin by 1024 × 1024 pixels, each with a size of 130 µm × 130 µm. They are grouped in four independent quadrants. This configuration allows a simultaneous readout of the four quadrants in rolling shutter mode which is necessary to achieve the required time resolution of 5 ms in full frame mode. The time resolution can optionally be improved by operating the LDA in window mode which means to read out a small region of the detector area where the X-ray source of interest is imaged. The FD with a field of view of $143'' \times 143''$ is designed for observations of bright point sources and is therefore composed of only 64 × 64 pixels which facilitates high time resolution. It is operated in split full frame mode, i.e. the detector architecture permits a simultaneous readout of two sensor halves which improves the time resolution by a factor of two, resulting in a time resolution of 80 µs. By defocussing the detector by 35 mm, a more uniform distribution of the photon hits over the sensor area is achieved and thus a pile-up $\leq 1\%$ for an observation of a 1 Crab source.

The DEPFET sensor is also sensitive to visual and UV light. Therefore an optical blocking filter is necessary yielding a reduction of visual light transmission by about six orders of magnitude. It will be split in two parts: an aluminum layer of 90 nm will be directly deposited on the photon entrance window of the sensor chip and the other part will be accommodated as foil in the filter wheel. The foil has a thickness of 150 nm of polyimide and 30 nm of aluminum. For the WFI instrument, no vacuum enclosure is foreseen and therefore the filter foil has to survive the acoustic noise loads arising during launch of the satellite. Analysis and tests are currently performed to verify that a mesh support prevents any performance degradation of the ultra-thin and fragile filter foil, e.g. by a rupture. Both optical blocking filters affect of course the quantum efficiency (QE) of the detector at low energies. At the carbon line (277 eV), the required quantum efficiency of >20% will be achieved. For higher energies the quantum efficiency

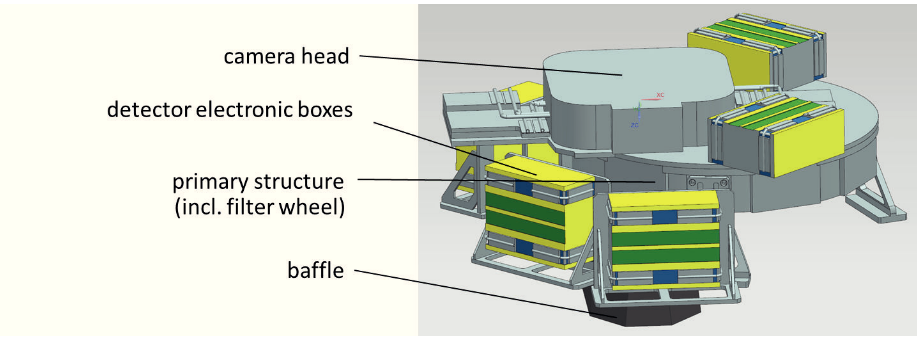

Figure 2. WFI instrument with its main subsystems: camera head comprising the detectors, five detector electronic boxes surrounding the camera head, the primary structure which is part of the filter wheel housing and the mounting interface to the science instrument module (SIM) of the satellite, the filter wheel and the optical stray–light baffle in front of it. Note that the two Instrument Control and Power Distribution Units, which are outside of the focal plane, are not shown here.

suffers little from the absorption by the optical blocking filters. At 1 keV energy, the QE is already >80% and at 10 keV even above 90% which meets the scientific requirements. The DEPFET sensor itself (i.e without coating) shows a high quantum efficiency due to the concept of backside illumination in combination with the implementation of an ultra-thin photon entrance window (accomplished by a shallow implant). Another stringent requirement to the WFI instrument is to achieve a non-X-ray background of $<5\,\mathrm{x}\,10^{-3}$ counts s^{-1} cm^{-2} keV^{-1} in the energy range from 2 keV to 7 keV in 60% of the observing time according to the science requirements. Coating of both sensor surfaces as well as anti-coincidence analysis by identification of particle hits with the detector itself will facilitate the attainment of this challenging goal. Furthermore, the contribution of low-energy electrons and protons, which are transmitted through and imaged by the mirror system, will be minimized. While typically on X-ray satellites only electrons are deflected, Athena employs for this purpose a magnetic diverter accommodated in front of the WFI, which deflects also low-energy protons from the LDA.

2. WFI Conceptual Design and Development

The conceptual design of the WFI instrument with its subsystems is shown in Fig. 2. X-ray photons are focussed by the Athena mirror system, which has a focal length of 12 m, onto either the WFI or the X-IFU instrument (Fig. 3). Regarding the WFI camera, there are actually two different focal points depending whether the LDA or the FD detector observes the X-ray sky. Pointing to any of the three focal points is accomplished by a tiltable mirror system mounted

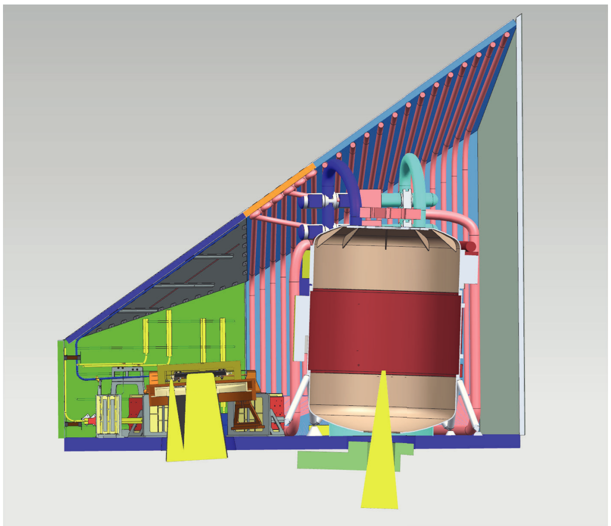

Figure 3. WFI instrument on the left and X-IFU instrument on the right accommodated on Athena's science instrument module (SIM). The related field of views for the FD and LDA of WFI and for the X-IFU detector are indicated at the bottom in the figure (image credits: ESA and MPE).

on a hexapod (Bavdaz et al., 2017). The source X-ray photons pass at first through the magnetic diverter and the optical stray-light baffle of WFI. Then they pass the filter wheel, which provides four positions for each of the two WFI detectors: I) the optical and UV blocking filter, II) the radioactive onboard calibration source to irradiate the sensor area with monochromatic X-ray photons for performance verification, III) the open position for optimum venting and outgassing as well as for special observations without filter (of the filter wheel) but higher quantum efficiency, and IV) the closed position whereby the detector is mechanically protected on ground and shielded against radiation in space. Finally, the X-ray photons hit the DEPFET sensor chip and generate signal electrons which are collected in the internal gate of the DEPFET (DEpleted P-channel Field Effect Transistor). This causes an increase of the transistor current which is proportional to the signal charge and thus to the photon energy. The Switcher-A ASICs select the lines for readout row by row, while the 64-channel Veritas-2.1 ASICs perform the readout of all pixels of a row in parallel. The signals are then multiplexed to one output per ASIC to minimize the number of ADCs. The detector is supplied and controlled by the Detector Electronics (DE) and the output signals are processed there in real-time in order to reduce the data to an acceptable rate. Electrical interface between the detector and the DE is a flexible lead integrated in the detector as shown in Fig. 1. The five DEs, four for the individual LDA quadrants and one for the FD, are controlled and supplied by the Instrument Control and Power distribution Unit (ICPU), which is implemented in cold redundancy. In contrast to the other subsystems of WFI, the two ICPU boxes can be accommodated outside the focal plane at a relatively large distance to the instrument. The ICPU is the electrical, command and data interface between the DEs and the spacecraft. It performs further data analysis and data compression before transmission to the mass memory onboard of the satellite.

The sensors, the front-end electronics ASICs, and the DEs require cooling but to different temperatures (Meidinger et al., 2017a). Therefore, different cooling chains are implemented which link the subsystem by heat pipes to dedicated radiator panels that are exposed to the cold space. The accurate control and stabilization of the detector temperature is performed by heater units.

The most complex development for the WFI instrument is that of the detectors, which are the key element of the camera. Prototype DEPFET sensors using different transistor design, fabrication process technology, and readout options have been developed with the goal to identify by measurements the optimum type. The Switcher-A ASIC as well as the Veritas-2.1 ASIC have been designed and tested for the Athena-WFI project, first just the ASIC characteristics and then integrated in the detector system. Such a small prototype detector, comprising a 64 × 64 pixel matrix, is shown in Fig. 4.

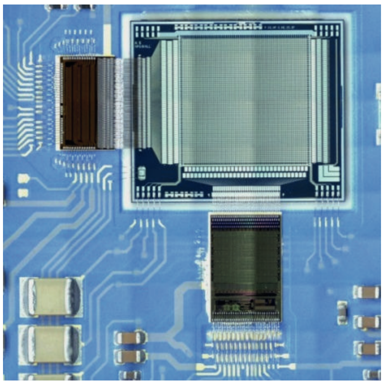

Figure 4. Prototype detector of WFI with 64 × 64 pixel sensor, the Switcher-A control ASIC to the left and the Veritas-2.1 readout ASIC at the bottom. The three silicon devices are connected by wire bonds.

With appropriate types of the sensor, spectra as shown in Fig. 5 have been measured. They yield full width at half maximum (FWHM) values of 130 eV at 5.9 keV photon energy and read noise values between 2.0 and 2.5 electrons rms under relevant operating conditions, in particular for the required fast readout of

2.5 µs per row for the FD (Meidinger et al., 2017a). For the LDA, a readout time requirement of 5 ms is defined corresponding to 9.8 µs per row. With a matrix of 256 × 256 pixels, which is a quarter of the flight-size matrix, a performance of 135 eV FWHM at 5.9 keV photon energy and a read noise of 3.2 electrons rms was measured for a readout time of 5 µs per row. This is a promising result, facing the fact that larger detectors require typically longer readout times per row because of larger RC time constants. The fast readout of large DEPFET arrays (matrices) is facilitated by a special readout mode enabled by Veritas-2.1, called drain readout. However this readout can only be used if the transistor currents of all pixels are quite uniform (Treberspurg et al., 2017). The alternative source follower readout mode is slower but less affected by inhomogeneities of the transistor currents over the sensor area. The final decision on the readout mode will be taken after further tests and analysis have been performed providing better statistics.

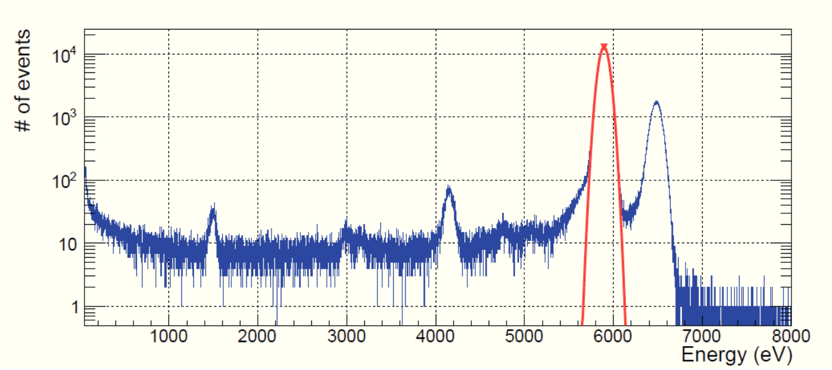

Figure 5. ^{55}Fe source spectrum measured with a small 64 × 64 pixel prototype DEPFET detector. At 5.9 keV photon energy of the Mn-K$_\alpha$ line, a FWHM of 130 eV is obtained.

3. WFI Status and Outlook

In the present phase A of the project, the conceptual design of WFI is defined and the necessary development of technologies is performed. Critical subsystems with respect to the development are the verification of detector function and performance, the real-time capability of the onboard signal processing chain and whether the ultra-thin large-area optical blocking filter withstands the acoustic noise loads which arise during launch in ambient conditions. The latter is critical as no vacuum enclosure is planned.

In the course of the technology development, various prototype detectors comprising the key components: DEPFET sensor, Switcher-A ASIC and Veritas-2.1 ASIC, have been developed and tested as described in section 2. The results determine in particular the design and technology of the pre-flight DEPFET sensors, which will be the first devices of flight-size, but drive also the redesign of Veritas-2.1 to achieve optimized performance.

For verification of the signal processing chain, a breadboard is developed using a Microsemi RTG4 FPGA as central element. All necessary steps for signal correction and filtering will be tested in particular to evaluate the time needed for this and to verify the real-time processing capability. A rigorous data reduction onboard of the satellite is mandatory because of the high frame rate combined with the large number of pixels. Otherwise, the WFI data rate would far exceed the allowed telemetry rate to ground.

Tests in acoustic noise facilities complemented by vibration tests shall demonstrate that the 17 cm x 17 cm large and 180 nm thin optical blocking filter survives the satellite launch. This should be possible by support of the filter foil with an appropriate mesh and by a design of the filter wheel which minimizes the loads. First tests have already been performed and the verification test will be conducted within the current technology development phase.

Furthermore, an optimized thermal system has been studied and designed. It is subdivided in three different thermal chains, all based on passive cooling.

Trade-offs have been performed for various concept options to obtain an architecture of the WFI instrument compliant with the requirements to the instrument, especially with respect to energy, time, and spatial resolution, quantum efficiency, instrumental background, as well as technical budgets like mass, volume, power consumption, and radiator area.

After the technology development and breadboarding phase, which shall be finished in 2018, an engineering model and a structural-thermal model of the WFI will be developed and tested, followed by the qualification model, and finally the flight model. The launch of Athena is scheduled for 2028/2029 with destination to Lagrange point L2.

Acknowledgements. The authors are grateful to all colleagues and institutions that support the Wide Field Imager instrument for Athena. The WFI Proto-Consortium is formed by MPE, ECAP, IAAT (all DE), CBK/CAMK (PL), University of Leicester and Open University (both GB), DTU (DK), IWF and University of Vienna (both AT), University of Palermo and INAF-OABO (both IT), CEA and Observatory Strasbourg (both FR), PennState, MIT, SAO and Standford/SLAC (all US), IA (PT), NOA (GR), and University of Geneva (CH). The work was funded by the Max-Planck-Society and the German space agency DLR (FKZ: 50 QR 1501). Development and production of the DEPFET sensors for the Athena WFI is performed in collaboration between MPE and the MPG Semiconductor Laboratory (HLL).

References

Bavdaz, M., Wille, E., Ayre, M., et al., The ATHENA telescope and optics status. 2017, *Proc. SPIE*, **10399**, 0B1, DOI: 10.1117/12.2274776

Meidinger, N., Barbera, M., Emberger, V., et al., The Wide Field Imager instrument for Athena. 2017a, *Proc. SPIE*, **10397**, 0V1, DOI: 10.1117/12.2271844

Meidinger, N., Eder, J., Eraerds, T., et al., The Wide Field Imager Instrument for Athena. 2017b, *ArXiv e-prints*

Nandra, K., Barret, D., Barcons, X., et al., The Hot and Energetic Universe: A White Paper presenting the science theme motivating the Athena+ mission. 2013, *ArXiv e-prints*

Treberspurg, W., Andritschke, R., Baehr, A., et al., Studies of prototype DEPFET sensors for the Wide Field Imager of Athena. 2017, *Proc. SPIE*, **10397**, 0U1, DOI: 10.1117/12.2274032